DOUGLAS HECTOR FONTES

NUMERICAL STUDY OF LIQUID JET IN CROSSFLOW USING A HYBRID APPROACH

FEDERAL UNIVERSITY OF UBERLÂNDIA

MECHANICAL ENGINEERING FACULTY

2018

DOUGLAS HECTOR FONTES

NUMERICAL STUDY OF LIQUID JET IN CROSSFLOW USING A HYBRID APPROACH

Dissertation presented to the Mechanical Engineering Postgraduate Program of the Federal University of Uberlândia, as part of the requirements for obtaining the qualification of **DOCTOR IN MECHANICAL ENGINEERING**.

Concentration area: Heat transfer and Fluid Mechanics.

Advisor: Prof. Dr. Francisco José de Souza

Uberlândia - MG
2018

Dados Internacionais de Catalogação na Publicação (CIP)
Sistema de Bibliotecas da UFU, MG, Brasil.

F683n
2018

Fontes, Douglas Hector, 1990-
Numerical study of liquid jet in crossflow using a hybrid approach [recurso eletrônico] / Douglas Hector Fontes. - 2018.

Orientador: Francisco José de Souza.
Tese (Doutorado) - Universidade Federal de Uberlândia, Programa de Pós-Graduação em Engenharia Mecânica.
Modo de acesso: Internet.
Disponível em: http://dx.doi.org/10.14393/ufu.te.2018.914
Inclui bibliografia.
Inclui ilustrações.

1. Engenharia Mecânica. 2. Aerossóis. 3. Equações. 4. Métodos de simulação. 5. Lagrange, Funções de. I. Souza, Francisco José de. II. Universidade Federal de Uberlândia. Programa de Pós-Graduação em Engenharia Mecânica. III. Título.

CDU: 621

Isabella de Brito Alves - CRB-6/3045

UNIVERSIDADE FEDERAL DE UBERLÂNDIA
Coordenação do Programa de Pós-Graduação em Engenharia Mecânica
Av. João Naves de Ávila, nº 2121, Bloco 1M, Sala 212 - Bairro Santa Mônica, Uberlândia-MG, CEP 38400-902
Telefone: (34) 3239-4282 - www.posgrad.mecanica.ufu.br - secposmec@mecanica.ufu.br

ATA

ATA DE DEFESA DE TESE

NÚMERO DE ORDEM: 259

DATA: 19/12/2018

Às nove horas do dia dezenove de dezembro de dois mil e dezoito, no Auditório do Laboratório de Mecânica dos Fluidos - Bloco 5P, Campus Santa Mônica, reuniu-se a Banca Examinadora composta pelos professores Dr. Francisco José de Souza (Orientador), Dr. Aristeu da Silveira Neto, Dr. Gilmar Guimarães e Dr. João Marcelo Vedovoto, da Universidade Federal de Uberlândia, Dr. Dirceu Noriler, da Universidade Estadual de Campinas, e Dr. Rudolf Huebner, da Universidade Federal de Minas Gerais, para, sob a presidência do primeiro, desenvolver o processo de avaliação da tese intitulada ***"Numerical Study of Liquid Jet in Crossflow Using a Hybrid Approach"***, apresentada pelo aluno **DOUGLAS HECTOR FONTES**, matrícula número **11513EMC010**, em complementação aos requisitos determinados pelo Regimento do Programa de Pós-Graduação em Engenharia Mecânica para obtenção do título de Doutor. Após discorrer sobre seu trabalho, o candidato foi arguido pelos membros da Banca, diante das comunidades universitária e externa. Em seguida, a tese foi avaliada em seção privada pelos membros da Banca que, ao encerrar o processo, consideraram-na:

(x) Aprovada
(   ) Aprovada com modificações a serem submetidas para a aprovação do orientador
(   ) Aprovada com modificações a serem submetidas para a aprovação da banca
(   ) Reprovada

conferindo ao aluno, em caso de aprovação, o título de Doutor em Engenharia Mecânica, Área de Concentração: **Transferência de Calor e Mecânica dos Fluidos**; Linha de Pesquisa: **Dinâmica dos Fluidos e Transferência de Calor**. As demandas complementares observadas pelos examinadores deverão ser satisfeitas no prazo máximo de 30 dias, para dar validade a esta aprovação. Para constar, lavrou-se a presente ata, que vai assinada pelo presidente e demais membros da Banca.

Membros:

Prof. Dr. Francisco José de Souza (orientador) - UFU

Prof. Dr. Aristeu da Silveira Neto - UFU

Prof. Dr. Gilmar Guimarães - UFU

Prof. Dr. João Marcelo Vedovoto - UFU

Prof. Dr. Dirceu Noriler - Unicamp

Prof. Dr. Rudolf Huebner - UFMG

Uberlândia, 19 de dezembro de 2018

Documento assinado eletronicamente por **Francisco José de Souza**, **Professor(a) do Magistério Superior**, em 19/12/2018, às 13:55, conforme horário oficial de Brasília, com fundamento no art. 6º, § 1º, do Decreto nº 8.539, de 8 de outubro de 2015.

Documento assinado eletronicamente por **João Marcelo Vedovoto**, **Professor(a) do Magistério Superior**, em 19/12/2018, às 14:14, conforme horário oficial de Brasília, com fundamento no art. 6º, § 1º, do Decreto nº 8.539, de 8 de outubro de 2015.

Documento assinado eletronicamente por **Dirceu Noriler**, **Usuário Externo**, em 19/12/2018, às 15:20, conforme horário oficial de Brasília, com fundamento no art. 6º, § 1º, do Decreto nº 8.539, de 8 de outubro de 2015.

Documento assinado eletronicamente por **Aristeu da Silveira Neto**, **Professor(a) do Magistério Superior**, em 19/12/2018, às 17:29, conforme horário oficial de Brasília, com fundamento no art. 6º, § 1º, do Decreto nº 8.539, de 8 de outubro de 2015.

Documento assinado eletronicamente por **Gilmar Guimarães**, **Professor(a) do Magistério Superior**, em 19/12/2018, às 17:30, conforme horário oficial de Brasília, com fundamento no art. 6º, § 1º, do Decreto nº 8.539, de 8 de outubro de 2015.

Documento assinado eletronicamente por **Rudolf Huebner**, **Usuário Externo**, em 04/01/2019, às 11:47, conforme horário oficial de Brasília, com fundamento no art. 6º, § 1º, do Decreto nº 8.539, de 8 de outubro de 2015.

A autenticidade deste documento pode ser conferida no site https://www.sei.ufu.br/sei/controlador_externo.php?acao=documento_conferir&id_orgao_acesso_externo=0, informando o código verificador **0925843** e o código CRC **2359E223**.

"To Jesus Christ, my God, Lord and friend."

ACKNOWLEDGEMENTS

First of all, I express my entire gratitude to the owner of all knowledge, God, for all that I am and I have comes from Him.

I would like to thank my wife, Bruna, for supporting me and staying by my side at all moments of life.

To my parents, Hamilton and Luciene (*in memoriam*) my eternal gratitude for everything. They are example and wisdom for me. I do not have words to explain...

A special thank goes to all my colleagues of the MFlab, especially to Vitor Vilela, Lucas Meira and Carlos Antônio for helping in parts of this work.

Finally, I would like to my advisor Francisco José de Souza for many opportunities he gave me. He is an excellent advisor, professor, code programmer and engineer.

FONTES, D. H., **Numerical study of liquid jet in crossflow using a hybrid approach** 2018. 122 p. Ph.D. dissertation, Federal University of Uberlândia, Uberlândia-MG, Brazil.

ABSTRACT

The main goal of this dissertation is to present a proper methodology for numerical solution of spray formation in liquid jet in crossflow configuration, by means of a hybrid approach. Hybrid approach is a mixture of Euler-Euler and Euler-Lagrange approaches to solve a specific problem. From the stand point of the objectives of the dissertation, the VOF method was implemented in the unstructured grid code UNSCYFL3D, in which Euler-Lagrange structure had been already implemented. Numerical verification and validation for VOF method showed results according to the data from literature. Two primary breakup coefficients, two secondary breakup models and the effects of two-way coupling with droplet-to-droplet collisions were systematically evaluated, in order to establish the most suitable methodology to solve liquid jet in crossflow in the regimes of the studied cases. Numerical results presented good agreement with the experimental ones, related to liquid jet topology, spray formation, mean diameter of droplets, mass fraction distribution and droplet velocity. Considering the most difficult feature to be obtained experimentally, the primary coefficient $C_b = 3.44$ and the AB-TAB secondary breakup model showed the best agreement with the experimental results. Numerical results using two-way coupling with droplet-to-droplet collision presented negligible differences related to simulations using one-way coupling.

Keywords: Liquid jet in crossflow, spray, primary breakup, secondary breakup

FONTES, D. H., **Avaliação numérica de jato líquido em escoamento cruzado utilizando uma abordagem híbrida** 2018. 122 f. Tese de Doutorado, Universidade Federal de Uberlândia, Uberlândia-MG, Brasil.

RESUMO

Esta tese tem por obejtivo apresentar uma metodologia adequada para solução numérica da formação de aerossol na configuração de jato líquido em escoamento cruzado de gás, por meio de uma abordagem híbrida. A abordagem híbrida pode ser descrita como uma mistura das abordagens Euler-Euler e Euler-Lagrange na solução de um problema específico. Tendo em vista o objetivo da tese, realizou-se a implementação do método VOF (abordagem Euler-Euler) no código de malha não estruturada UNSCYFL3D, no qual a estrutura numérica para a abordagem Euler-Lagrange já estava implementada. Verificações e validações numéricas para o método VOF foram realizados, gerando resultados satisfatórios, em concordância com dados da literatura. Dois coeficientes para correlação de quebra primária, dois modelos de quebra secundária e acoplamento de duas vias com colisão entre partículas foram avaliados sistematicamente, de modo a estabelecer para os casos simulados a metodologia mais adequada para a solução numérica de aerossol na configuração de jato líquido em escoamento cruzado. Os resultados numéricos apresentaram boa concordância com os dados experimentais no que tange à topologia do jato líquido, formação do aerossol, estimativas do diâmetro médio, distribuição de fração mássica e velocidade de gotas. Em termos das características de mais difícil reprodução com simulações numéricas, o coeficiente de quebra primária $C_b = 3.44$ e o modelo de quebra secundária AB-TAB apresetaram melhor concordância com os experimentos. As simulações usando acoplamento de duas vias com colisão entre partículas não apresentaram diferenças significativas em relação às simulações com acoplamento de uma via.

Palavras-chave: Jato líquido em escoamento cruzado, aerossol, quebra primária, quebra secundária, VOF

List of Figures

1.1 German aircraft Messerschmitt Bf 109. 1

2.1 Diagram of the analyzed LJIC domain. 6

2.2 Visualizations of breakup mechanisms identified by Oda et al. (1994). 9

2.3 Visualizations of breakup mechanisms identified by Wu, Kirkendall and Fuller (1997). 10

3.1 Representation of the two assumed droplet interaction. 27

3.2 Schematic representation of the Taylor Analogy Breakup. 38

3.3 Schematic diagram of two finite volumes of an unstructured grid. 42

3.4 Flow chart of the SIMPLE method. 46

3.5 Diagram of particle position and centroid of cells. 49

3.6 Flow chart of the general overview of the numerical modeling applied in the numerical simulation procedure. 51

4.1 Diagram of the initial position of the sphere submitted to deformation. 53

4.2 Temporal stages of the droplet deformation. 55

4.3 Diagram of the denser sphere surrounded by less dense phase in a cubic domain. 57

4.4 Magnitude of spurious velocities. 58

4.5 Map showing the bubble entrainment zone for different conditions based on the Weber and Froude numbers, adapted from (OGUZ; PROSPERETTI, 1990). 60

4.6 Schematic of the droplet in the imminence of impacting the water pool. 61

4.7 The effect of the air pushing the free surface of the water pool. 62

4.8 Qualitative comparisons of the numerical splash topologies with images from Morton, Rudman and Liow (2000) for the case I. 62

4.9 Qualitative comparisons of the numerical splash topologies with images from Morton, Rudman and Liow (2000) for the case II. 63

4.10 Quantitative comparison of the numerical results for the depth crater with the experimental data of Morton, Rudman and Liow (2000). 63

4.11 Dimensions of the experimental domain for the two cases of LJIC. 65

4.12 Physical domain for the two cases of LJIC. 65

4.13 Map of momentum flux ratio versus Weber number for the primary breakup of the LJIC. 66

4.14 Grid and refinement zone near jet. 68

4.15 Comparison of volume fraction field at $x-plane$ and mass fraction distribution and velocity at $z-plane$ for both analyzed domains. 69

4.16 Pressure on liquid column jet and spray formation. 71

4.17 Profiles of liquid column jet. 72

4.18 Streamwise velocity component. 72

4.19 Streamlines of air flow around the liquid jet. 73

4.20 General view of the first and secondary breakups. 74

4.21 Sampling plane at $3.81\ cm$, red line. 76

4.22 Average of droplet diameter in three planes for $C1$. 77

4.23 Schematic diagram of a drop with oblique velocity compared to the air streamline. 78

4.24 Average of droplet diameter in three planes for $C2$. 80

4.25 Mass fraction distribution for $C1$ using different primary and secondary breakup models. 82

4.26 Mass fraction distribution for case $C2$ using different primary and secondary breakup models. 84

4.27 Droplet velocity for $C1$ at the sampling plane $3.81\,cm$ downstream of the liquid jet nozzle. 85

4.28 Liquid jet curvature for $C1$. 87

4.29 Droplet velocity for $C2$ at the sampling plane $3.81\,cm$ downstream of the liquid jet exit. 88

4.30 Mass fraction distribution using $C_b = 3.44$ and AB-TAB model. 90

4.31 Droplet velocity using $C_b = 3.44$ and AB-TAB model. 91

List of Tables

2.1 Important dimensionless parameters for LJIC study 7

3.1 The analogy between the mass-spring-damper system and a oscillating and distorting droplet. 38

4.1 Error of numerical simulation compared to the analytical solution for different algebraic schemes and Courant numbers. 56

4.2 Comparison of the numerical solution and analytical solution for the problem of surface tension in a stationary inviscid droplet. 58

4.3 Scaled dimensions of the splash cases. 61

4.4 Physical properties of the fluids studied. 65

4.5 Flow conditions for the two studied cases. 66

4.6 Numerical settings for the two studied cases. 67

4.7 Mean diameter of droplet in the last plane (air tunnel exit) for $C1$. 79

4.8 Mean diameter of droplet in the last plane (air tunnel exit) for $C2$. 81

4.9 $l2-norm$ of the mass fraction distribution for $C1$. 83

4.10 $l2-norm$ of mass fraction distribution for $C2$. 83

4.11 $l2-norm$ of the mass fraction distribution for $C2$. 89

List of Symbols

Abbreviations

AMR	Adaptive Mesh Refinement
CAP	Contribution of the ap coefficients
CICSAM	compressive interface capturing scheme for arbitrary meshes
CIP	Cubic Interpolated Pseudo-particle
CLSMOF	Coupled Level Set Moment of Fluid
CLSVOF	Coupled Level Set Volume of Fluid
CSF	Continuum Surface Force
FVM	Finite Volume Method
HRIC	high resolution interface capturing
LES	Large Eddy Simulation
LJIC	Liquid jet in crossflow
LPP	lean, premixed and pre-vaporized combustion
PDA	phase Doppler anemometry
PDF	probability density function
PDPA	Phase Doppler Particle Analysis

PLIC	Piecewise Linear Construction
RT	Rayleigh-Taylor
SMD	Sauter Mean Diameter
TAB	Taylor Analogy Breakup
URANS	Unsteady Reynolds Averaged Navier-Stokes
VOF	Volume of Fluid

Greek letters

α	volume fraction
δ	to represent the Kronecker delta
ϵ	dissipation rate of the turbulent kinetic energy
κ	turbulent kinetic energy or interface curvature in the VOF model
Λ	integral length of the turbulent jet $[m]$
λ	wave length $[m]$ or a specific coefficient for different models
μ	dynamic viscosity $[kg \cdot m^{-1} \cdot s^{-1}]$
ρ	density $[kg \cdot m^{-3}]$
σ	surface tension coefficient $[N \cdot m^{-1}]$
τ	relaxation time
τ	stress tensor
ε	surface breakup efficiency factor

Latin letters

b	collision impact parameter

Ca	Capilarity number
Co	Courant number
d	diameter $[m]$
f	source term
Fa	Faeth number
g	gravity $[m \cdot s^{-2}]$
J	Liquid to air momentum ratio
L	to indicate left side or length scale
m	index for iteration or mass $[kg]$
Ma	Mach number
n	to indicate normal vector
nf	number of faces
Oh	Ohnesorge number
p	pressure $[Pa]$
R	right
r	radius or distance (vector) $[m]$
Re	Reynolds number
s	distance $[m]$
t	time $[s]$
u	velocity component $[m \cdot s^{-1}]$
V	volume $[m^3]$

v	velocity component $[m \cdot s^{-1}]$
w	velocity component $[m \cdot s^{-1}]$
We	Weber number
x	spatial coordinate component $[m]$
Y	random number between 0 and 1
y	spatial coordinate component $[m]$
z	spatial coordinate component $[m]$

Subscripts

∞	to indicate a bulk or mean value of the air crossflow
b	to indicate primary breakup
c	to indicate the jet column
$crit$	to indicate a critical value
d	to indicate drag
f	to indicate face value
g	to indicate the gas phase
i	index notation
j	index notation
jet	to indicate a variable of the jet flow
L	to indicate length scale
l	to indicate the liquid phase
p	to indicate particle or the centroid of a numerical finite volume

R	to indicate right side
rel	to indicate relative values
s	to indicate the surface of the jet column
sc	surface control
st	surface tension
st	to indicate surface tension
t	to indicate turbulent variable
vc	volume control
w, b	to indicate the combined buoyancy-weight force

Superscripts

$'$	to indicate fluctuating value
$''$	to indicate flux over a surface area
$\bar{\ }$	to indicate the mean value
n	current time for the variables
$*$	to indicate first approximation

CONTENTS

LIST OF FIGURES **viii**

LIST OF TABLES **x**

1 INTRODUCTION **1**

1.1 Objectives 3

1.2 Dissertation structure 3

2 LITERATURE REVIEW **5**

2.1 LJIC fundamentals 5

2.2 Experimental analysis of LJIC 7

2.3 Numerical analysis of LJIC 15

2.3.1 Euler-Lagrange approach 16

2.3.2 Euler-Euler approach 18

2.3.3 Hybrid approach 21

2.3.3.1 Low dependence on transition models 21

2.3.3.2 High dependence on transition models 22

3 MODELING AND METHODOLOGY **25**

3.1 Physical modeling 25

3.2 Mathematical modeling 27

3.2.1 Eulerian referential 28

3.2.1.1 Turbulence closure model 29

3.2.1.2 Two-phase model 32

3.2.2 Lagrangian referential 34

3.2.3 Primary breakup and secondary breakup models 36

3.3 Numerical modeling 41

3.3.1 Eulerian referential 41

3.3.1.1 Temporal term 41

3.3.1.2 Advection term 42

3.3.1.3 Diffusion term 43

3.3.1.4 Advection scheme for VOF method 43

3.3.1.5 Pressure-velocity coupling 45

3.3.1.6 Momentum interpolation method 46

3.3.2 Lagrangian referential 48

3.3.2.1 Integration scheme 48

3.3.2.2 Interpolation at the particle position 48

3.3.2.3 Algorithm of particle tracking 49

3.3.3 Numerical overview 50

3.3.4 Methodology 50

4 RESULTS AND DISCUSSIONS **52**

4.1 Verification and validation of VOF method 52

4.1.1 Sphere deformation 53

4.1.2 Surface tension in a stationary droplet 57

4.1.3 Water droplet splash 59

4.2 Numerical results for LJIC 64

4.2.1 LJIC cases and numerical settings 64

4.2.2 Strategy for domain reduction 67

4.2.3 LJIC characteristics using hybrid approach 70

4.2.4 Evaluation of primary breakup coefficients and secondary breakup models 75

4.2.4.1 General results for mean diameter distribution 76

4.2.4.2 Mass fraction distribution 81

4.2.4.3 Droplet velocity 85

4.2.5 Two-way coupling and droplet collision effects 89

5 CONCLUSIONS AND FUTURE WORK **92**

CHAPTER I

INTRODUCTION

Humanity has constantly sought improvements in living conditions, even in war. In the beginning of the World War II, the German aircraft Messerschmitt Bf 109, Fig. 1.1 had a big advantage over British fighters, concerning the type of fuel injection. The German aircraft had a different fuel injection, so that fuel injection into the engine did not fail, even in extreme manoeuvres, such as fly upside-down or to perform other negative-G manoeuvres.

Figura 1.1 – German aircraft Messerschmitt Bf 109.

The majority of processes and equipment in nature and industry is related with fluids and their interactions, which affect directly the efficiency of these processes and equipment. Regarding fluids in the possible existing systems, usually two-phase flow condition is encountered. Two-phase flow presents additional physical aspects to those in one-phase flow, such as interfacial interaction and high physical properties ratios. The interfacial interaction is extremely hard to study, since the interface is very thin, whose interactions occurs in microscopic level. However, the interface and their interactions are not treated in microscopic level, so that some physical concepts are inferred to keep analysis on continuum hypothesis, as an example by the use of the surface tension coefficient.

Spray is an important two-phase flow system that are present in many practical problems, such as: combustion, irrigation and airway medication. The efficiency of each process depend on several spray characteristics, for example: injection type, spray angle, droplet diameter, droplet velocity, and time/space to produce entirely the desired droplet distribution. Liquid jet in crossflow (LJIC) is used to obtain liquid spray in short length scale using simpler injection system, with lower pressure injection, than that used in diesel injection. Due to these features, LJIC has been used in gas turbine combustors, scramjet and ramjet combustors (HOJNACKI, 1972). The combustion efficiency of these combustors are highly dependent on the droplet formation. Therefore, the understanding of the breakup process is crucial to develop models able to predict the spray formation. Numerical simulations, with reliable models related to LJIC, can provide many useful information to enhance the combustors efficiency.

For better understanding of spray formation in LJIC, experimental analyses are extremely important. However, experimental analyses are often expensive and present geometric restrictions. When reliable models and correlations are well established, numerical simulations are an interesting approach for projects and provide relevant results that are difficult or impossible to obtain experimentally. Therefore, the development of numerical modeling able to predict suitably spray formation in LJIC is valuable for industrial and research purposes.

In this dissertation, the evaluation of some methodologies to solve numerically spray formation in LJIC is presented, aiming to advance the research about sprays.

1.1 Objectives

The purpose of this dissertation is to fill the gap related to numerical modeling in spray formation in LJIC. Currently, three numerical approaches have been used to solve LJIC: Euler-Euler, Euler-Lagrange and hybrid approach. The author of this dissertation aims to fill some gaps on the hybrid approach use, such as: evaluation of primary breakup coefficients, analysis of a new secondary breakup model proposed by Dahms and Oefelein (2016) and the evaluation of four way coupling on LJIC, using a hybrid approach.

Therefore, the main objective of this dissertation can be stated as: investigate numerically, by means of a hybrid approach, spray formation in LJIC configuration with respect to primary breakup modeling, secondary breakup model and the effect of two-way coupling along with droplet-to-droplet collision.

Furthermore, the following specific goals can be listed:

- implement subroutines for the VOF method Euler-Lagrange conversions and secondary breakup models on an unstructured grid code;
- verify and validate VOF implementation;
- make an appropriate computational grid to solve LJIC by means of hybrid approach;
- find detailed LJIC experimental cases for validation;
- and establish the spray features to compare the chosen models.

1.2 Dissertation structure

This dissertation was developed following a coherent structure composed by five chapters. In the present chapter, an introduction of the dissertation is made, covering the reasons to study spray and the objectives of the dissertation.

In chapter 2, a relevant bibliographic review about sprays in LJIC is presented. Firstly, physical fundamentals for LJIC are described, highlighting the main dimensionless variables related to LJIC problems. Secondly, the main results and correlations of experimental researches for spray in LJIC are shown from the former publications to the most recent ones, emphasizing how research has remained firmly. Finally, the numerical researches about the theme are discussed, where advantages and disadvantages of the three approaches, i.e., Euler-Euler, Euler-Lagrange and hybrid are shown.

In chapter 3 physical, mathematical and numerical modelings used in all simulations performed in this work are presented.

In the Chapter 4, all results are presented and discussed in detail. Verification of the VOF model implementation are presented, guaranteeing that VOF model implementation is correct and reliable. In the following, all numerical simulations for spray formation in LJIC are described, according to the evaluated correlations/models.

The main conclusions of the work along with some suggestions for future works related to sprays analysis are discussed in chapter 5.

CHAPTER II

LITERATURE REVIEW

This chapter is dedicated to contextualize the contribution of this dissertation in the most recent numerical research of liquid jet in crossflow (LJIC). Thus, the LJIC fundamentals, some experimental works and the numerical methods available to solve LJIC, with their respective numerical results of the state of the art, are presented in the following.

2.1 LJIC fundamentals

Liquid jet in crossflow (LJIC) consists of a liquid jet that interacts with a gas flow obliquely, as represented in Fig. 2.1. In this physical configuration, the interaction of phases and the properties differences between liquid and gas establish high gradients of physical properties in the interface that is infinitesimally thin, presenting a discontinuous properties jump. Instabilities may arise in LJIC, taking to the breakup of the intact liquid column and stripping droplets from the liquid surface concurrently, depending on the flow features. In LJIC, some physical phenomena can exist simultaneously: at the liquid-air interface, surface tension collaborates with the maintenance of the structure of the liquid jet column and liquid drops; turbulence eddies and aerodynamic instabilities favors the disruption of the liquid jet; and mass and momentum transfer contribute to the changes in mass and momentum of the

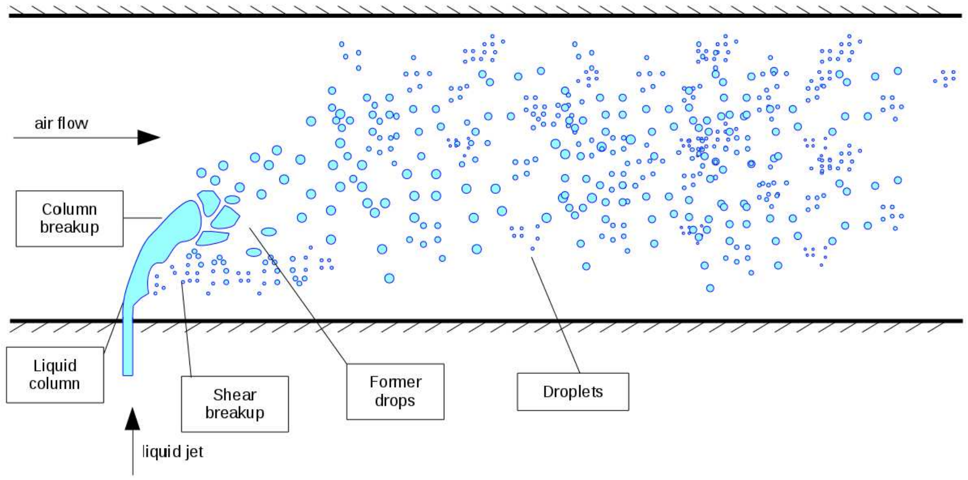

Figura 2.1 – Diagram of the analyzed LJIC domain.

each phase sharing interface.

In addition to the interface phenomena, primary breakup is inherently part of LJIC, consisting of the first ruptures of the intact liquid column, which creates the first droplets. This breakup process is very misunderstood due to the difficulties of visualizing droplets formation properly and obtaining not intrusive experimental flow data. However, it is known that primary breakup may occur due to the growth of Kelvin-Helmholtz, Rayleigh-Taylor, turbulent eddies instabilities and cavitation (BRAVO; KWEON, 2014).

Some of those droplets suffer secondary breakup, depending on the instabilities growth, related to the surface tension, aerodynamic and viscous forces balance. The droplets interact with the surrounding air flow and with one another, experiencing coalescence, elastic collision, or a composition of the last two modes.

Considering the complexity of the problem, some dimensionless numbers related to the physical phenomenon are very useful. Some important dimensionless numbers for LJIC are presented in Tab. 2.1, where, ρ_l, μ_l and d are respectively the density, dynamic viscosity and diameter of the liquid drop; ρ_g is the gas density and σ is the surface tension coefficient of the liquid-gas pair.

Tabela 2.1 – Important dimensionless parameters for LJIC study

Dimensionless number	Meaning	Formula
Droplet Reynolds	Inertia to viscosity forces ratio	$Re_l = \dfrac{\rho_l u_{p_{rel}} d_p}{\mu_l}$
Liquid Weber	Inertia to surface tension forces ratio	$We_l = \dfrac{\rho_l u_{jet}^2 d_p}{\sigma}$
Gas Weber	Inertia to surface tension forces ratio	$We_g = \dfrac{\rho_g u_\infty^2 d_p}{\sigma}$
Ohnesorge	Viscosity to inertial and surface tension forces ratio	$Oh = \dfrac{\mu_l}{\sqrt{\rho_l \sigma d_p}}$
Capilarity	Viscosity to surface tension forces ratio	$Ca = \dfrac{\mu_l u_p}{\sigma}$
J	Liquid to air momentum ratio	$J = \dfrac{\rho_l v_{jet}^2}{\rho_g u_\infty^2}$

Method and equipment improvements have gradually overcome the experimental and numerical challenge of LJIC spray formation analysis. In the next sections, some numerical and experimental outcomes in LJIC field are presented, over the years.

2.2 Experimental analysis of LJIC

First experimental works on LJIC were unable to analyze deeply spray formation, being limited to correlate the liquid jet penetration in the air crossflow.

Chelko (1950) obtained a jet penetration correlation, using photographs taken from LJIC through transparent tunnel walls. Jet penetration was correlated using the velocities and densities of the air (u_∞, ρ_g) and of the liquid jet (v_{jet}, ρ_l), the downstream distance from the jet nozzle center line, x, and the jet diameter, d_{jet}, according to Eq. 2.1,

$$\frac{y}{d_{jet}} = 0.450 \left(\frac{v_{jet}}{v_{\infty}}\right)^{0.95} \left(\frac{\rho_l}{\rho_g}\right)^{0.74} \left(\frac{x}{d_{jet}}\right)^{0.22}, \tag{2.1}$$

where: y is the distance of the liquid jet from the exit; d_{jet} is the jet diameter; v_{jet} is the jet velocity; v_{∞} is the velocity of the gas crossflow; ρ_l is the liquid density; ρ_g is the gas density and x is the longitudinal distance of the liquid jet. This correlation presented a deviation of approximately 7% from the experimental measurements.

The lateral penetration of a water jet in a supersonic air crossflow (i.e. the spray width from a top view of the jet diameter) for different Mach numbers was correlated by Rebello (1972). The author proposed equations for the jet penetration as function of the Mach number, injection pressure, jet diameter and angle of injection, identifying that the injector diameter and the angle of injection are the dominant parameters on the lateral jet penetration. The general empirical correlation for lateral penetration presented a degree of agreement of 0.86 compared with experimental data.

The experimental limitations of obtaining a better understanding of the spray formation in LJIC were reduced with the improvement of equipment and methodologies. Oda et al. (1994) studied the breakup of a liquid jet normal to a high-speed airstream using a laser-sheet tomography and Fraunhofer techniques (i.e. related to diffraction measurements). The authors used Eosine-Y($C_{20}H_6Br_4Na_2O$), a fluorescent dye, dispersed in water for better visualization of the breakup process. Two breakup mechanisms were identified for different flow conditions, according Fig. 2.2. In the first identified mechanism, surface and column breakup, the liquid jet was ejected into a high speed airstream, distorting of the liquid column towards a bow shape. Small droplets also detached from the tips of the bow, large drops were produced from the end of the liquid column and bellow the end of the liquid column a cavity in the liquid column was identified. In the second mechanism, column breakup, lower velocities of the liquid jet and the airstream were imposed, resulting in an unstable liquid column (snakelike shape). Beside this, the droplets were produced near of the end of the liquid column. The authors

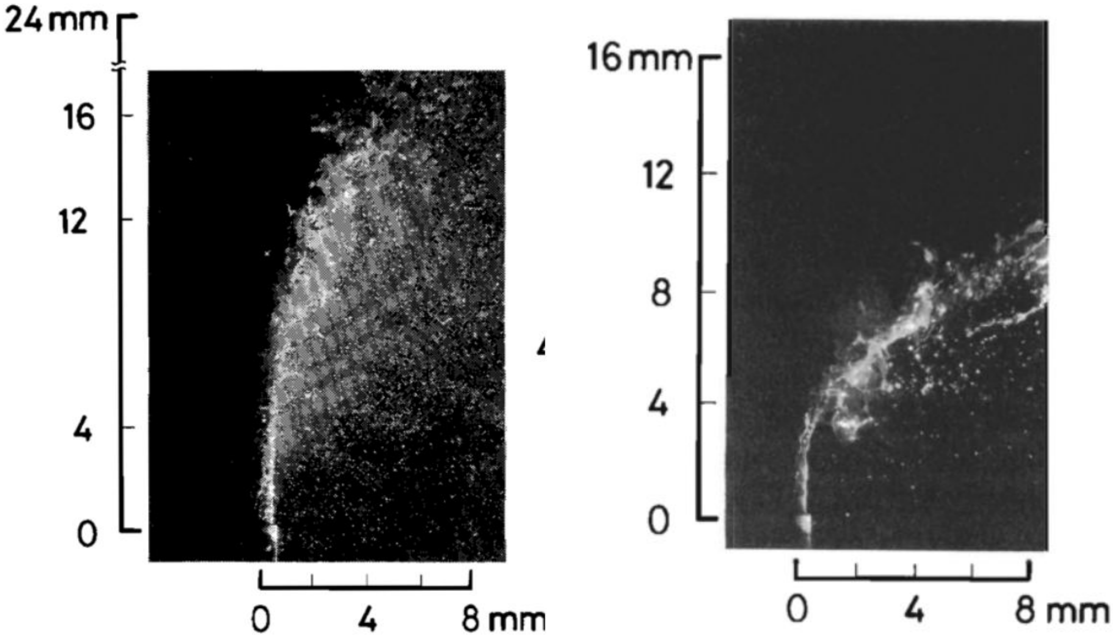

(a) Surface and column breakup.

(b) Column breakup.

Figura 2.2 – Visualizations of breakup mechanisms identified by Oda et al. (1994).

verified the intact liquid column height (before full breakup) is inversely proportional to the airstream velocity and directly proportional to the injection velocity.

In the work of Wu, Kirkendall and Fuller (1997), breakup process of LJIC in a subsonic air crossflow were experimentally studied, varying test liquids, injector diameter and Mach air number to obtain a wide range of operation conditions. Pulsed shadowgraphic technique was used to visualize and analyze the breakup properties and formation. In Fig. 2.3, different conditions of Weber and momentum ratios numbers are shown from the results of Wu, Kirkendall and Fuller (1997). The authors identified two primary breakup mechanisms, different from those of the work of Oda et al. (1994), termed shear breakup and column breakup, classifying them using Weber and liquid to air momentum ratio numbers. Just the column breakup was correlated using an analogy with the individual droplet breakup, when subjected to aerodynamic forces. Column breakup equations are expressed in function of the vertical (along to the jet), y, and horizontal (perpendicular to the jet), x, breakup position of the intact liquid column, respectively, Eq. 2.2 and Eq. 2.3. Additionally, liquid column trajectory,

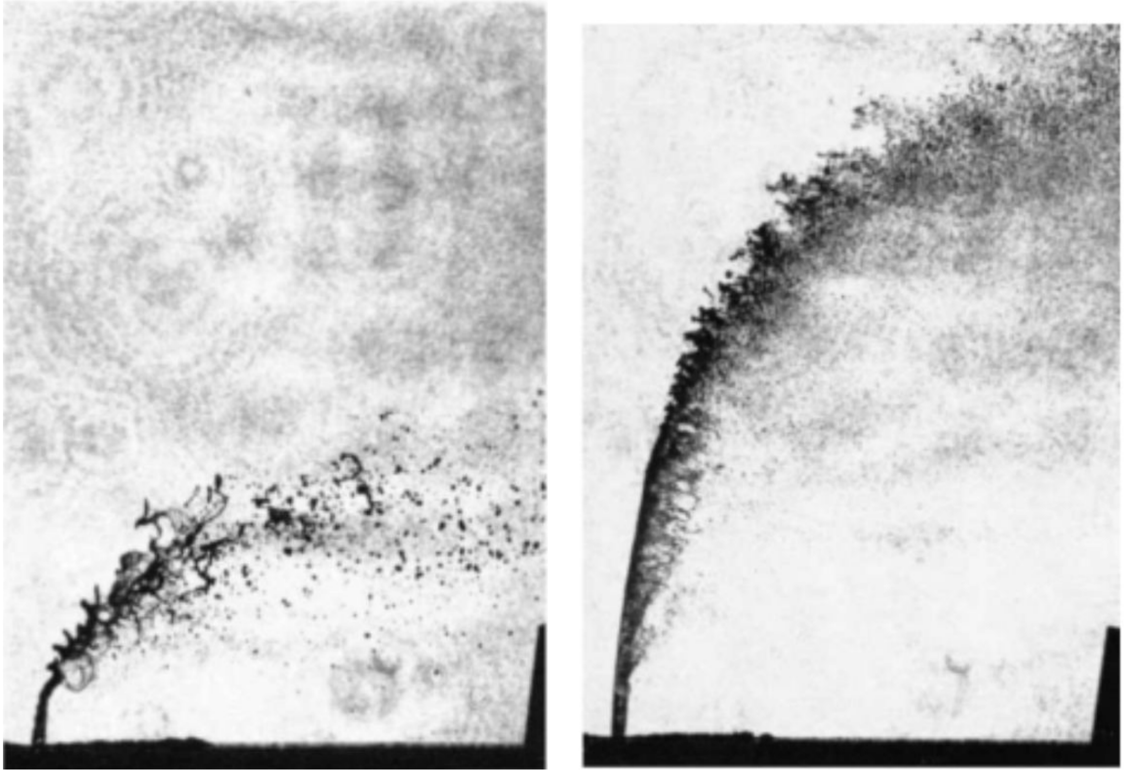

(a) $J = 9.9$ and $We = 71$. (b) $J = 70.8$ and $We = 160$.

Figura 2.3 – Visualizations of breakup mechanisms identified by Wu, Kirkendall and Fuller (1997).

Eq. 2.4, was correlated,

$$\frac{y_b}{d_{jet}} = 3.44\sqrt{J}, \tag{2.2}$$

$$\frac{x_b}{d_{jet}} = 8.06, \tag{2.3}$$

$$\frac{y}{d_{jet}} = 1.37\sqrt{J\left(\frac{x}{d_{jet}}\right)}, \tag{2.4}$$

where, the origin of the axes is the center of the exit jet diameter.

An experimental investigation of non-turbulent LJIC at normal temperature and pressure was carried out by Mazallon et al. (1998), using pulsed shadowgraphs to observe jet deformation and breakup. In their work, an wide range of dimensionless variables was evaluated, changing several parameters (different liquids, jet diameters, inlet jet velocities, air velocities): Weber number, $We = 2 - 200$; Ohnesorge number, $Oh = 0.00006 - 0.3$; liquid to gas momentum ratio, $J = 100 - 8000$; and liquid to gas density ratios, $\rho_l/\rho_g = 580 - 1020$. The authors inferred primary breakup process in LJIC was similar to the droplet breakup process (secondary breakup). Four breakup regimes were identified and characterized only through the Weber number (Ohnesorge, density ratio and liquid to gas momentum ratio presented little influence in the breakup regime): column breakup, $We > 5$; bag breakup, $5 < We < 60$; bag/shear breakup, $60 < We < 110$; and shear breakup, $We > 100$. Furthermore, the authors correlated two kinds of waves in the LJIC, observed in the experiments: column wave length, λ_c, and surface wave length, λ_s, Eq. 2.5 and Eq. 2.6, respectively,

$$\lambda_c/d_{jet} = 16.3We^{-0.79}, \tag{2.5}$$

$$\lambda_s/d_{jet} = 2.82We^{-0.45}. \tag{2.6}$$

These waves are related to the onset of the primary breakup in the LJIC, though none correlation of the drop diameter from the primary breakup was made in the work of Mazallon et al. (1998).

Becker and Hassa (2002) investigated experimentally breakup, penetration and atomization of a plain jet of kerosene jet A-1 fuel in an air crossflow at test conditions relevant to lean, premixed, pre-vaporized (LPP) combustion of gas turbines, using time-resolved shadowgraphs, Mie-scattering laser lightsheets and phase Doppler anemometry (PDA). Test were conducted in a quartz duct with rectangular cross section of 25 by 40 mm, where 27 were performed. Velocity, pressure and temperature of the air were respectively $u_\infty = 50, 75, 100$ m/s, $p_g = 1.5$ to 15 bar and $T_g = 290$ K. The authors confirmed, similarly to Wu, Kirkendall and Fuller (1997) and Mazallon et al. (1998), two breakup mechanisms, column breakup and surface breakup, obtaining through Eq. 2.7,

$$We_{crit} = 10^{\left(\dfrac{3.1 - log(J)}{0.81}\right)}, \tag{2.7}$$

a good agreement of their data with the mechanisms classification made by Wu, Kirkendall and Fuller (1997). Becker and Hassa (2002) also correlated jet penetration, y, in function of longitudinal distance from the diameter jet, $x/d_{jet} = 2 - 22$, liquid to air momentum ratio, $J = 1 - 40$ and We number, $We = 90 - 2120$, as expressed by Eq. 2.8,

$$\frac{y}{d_{jet}} = 1.48 J^{0.42} ln \left(1 + 3.56 \frac{x}{d_{jet}}\right), \tag{2.8}$$

presenting a standard deviation of 1.21 from the experimental data points.

An experimental investigation of the primary breakup of non-turbulent round liquids jets in gas crossflow was conducted by Sallam, Aalburg and Faeth (2003) considering different liquids, jet diameters, liquid jet velocities and air crossflow velocities, that yields the following range of dimensionless parameters: liquid to gas density ratio, $\rho_l/\rho_g = 683 - 1021$; Weber number, $We = 30 - 260$; liquid to air momentum ratio, $J = 3 - 200$; and Ohnesorge number, $Oh = 0.003 - 0.12$. Pulsed holography and shadowgraphy techniques were used to observe primary breakup of the LJIC, obtaining experimental uncertainties less than 10% for diameter larger than $0.01\ mm$ and for drop velocity, with 95% confidence. Similarities between primary breakup of the LJIC and breakup of individual drops subjected to shock wave disturbances were found, as Mazallon et al. (1998). Visualizations showed there is no influence of liquid jet turbulence or vorticity in the primary breakup of the liquid jet, even for jet Reynolds number of 30000. The authors identified three breakup regimes: bag, multimode and shear breakup, strongly related to the Weber number and not (or weakly) related to the liquid to air momentum ratio and Ohnesorge number, for conditions tested. Despite three breakup regimes were identified, the authors correlated two primary breakup mechanisms: breakup of the entire liquid column and shear breakup in the liquid jet surface. The distance from the exit jet diameter to the column breakup was correlated, similarly to Wu, Kirkendall and Fuller (1997), using the liquid to air momentum ratio, according Eq. 2.9,

$$\frac{y_b}{d_{jet}} = 2.6\sqrt{J}. \tag{2.9}$$

For the shear breakup correlation, the diameter of the ligaments formed along the column liquid surface by the aerodynamic interactions were measured. Measurements of the ligaments diameters were comparable to the drop sizes caused by the primary breakup along the liquid surface, assuming Rayleigh breakup caused drops to be formed from the end of the ligaments. Thus, the drop sizes from the primary breakup along the liquid jet are expressed by Eq. 2.10 and Eq. 2.11,

$$\frac{d_p}{d_{jet}} = 3.36\left(\frac{\nu_l y}{v_{jet} d_{jet}^2}\right)^{1/2}, y/y_c \leq 1, \tag{2.10}$$

$$\frac{d_p}{d_{jet}} = 0.132, y/y_c > 1, \tag{2.11}$$

where, ν_l is the kinematic viscosity of the liquid, v_{jet} is the jet velocity at the diameter jet exit and $y_c/d_{jet} = (0.001 v_{jet} d_{jet})/(\nu_l)$. Beside this, drop velocities after breakup were measured. The resulting correlations for drop velocities in jet direction and in air crossflow direction are expressed, respectively by Eq. 2.12 and Eq. 2.13

$$\frac{v_p}{v_{jet}} = 0.7, \tag{2.12}$$

$$\frac{u_p}{u_L} = \frac{u_p}{u_\infty (\rho_g/\rho_l)^{1/2}} = 6.4. \tag{2.13}$$

Deformation and breakup properties of turbulent LJIC were studied experimentally by Aalburg, Faeth and Sallam (2005), using pulsed shadowgraph and holograph observations, for the following conditions: gas Weber number, $We = 0 - 282$; liquid to gas density ratios of 683 and 845; jet exit Reynolds number, $Re = 3800 - 59000$; and small effects of the liquid viscosity, $Oh < 0.12$. Aalburg, Faeth and Sallam (2005) found a negligible effect of the gas crossflow on changing the liquid jet velocity in the jet flow direction, which means the liquid jet velocity, v_{jet}, is approximately constant. They proposed a correlation for drop SMD (Sauter Mean Diameter) in function of the distance along the liquid jet, Eq. 2.14,

$$\frac{SMD}{\Lambda} = 0.52\left(\frac{y}{\Lambda} We_\Lambda^{1/2}\right)^{0.52}, \tag{2.14}$$

where, $We_\Lambda = \rho_l \Lambda v_j / \sigma$ is the Weber number based on the integral length of the turbulent liquid jet, Λ. Droplet diameter was not affected by the crossflow, suggesting that turbulent primary breakup dominates aerodynamic effects in the conditions evaluated. Beside this, the authors showed that drop velocities after turbulent primary breakup were independent of the droplet size, with drop velocity in the liquid jet direction comparable to the liquid jet velocity at the exit, Eq. 2.15, while the droplet velocity in the air flow direction were correlated through Eq. 2.16,

$$\frac{v_p}{v_{jet}} = 0.6, \tag{2.15}$$

$$\frac{u_p}{u_L} = \frac{u_p}{u_\infty (\rho_g/\rho_l)^{1/2}} = 4.27. \tag{2.16}$$

An experimental investigation of the primary breakup of turbulent and non-turbulent LJIC, at normal pressure and temperature, is described by Sallam et al. (2006), for Weber numbers of $0-2000$, liquid to gas momentum ratios of $100-8000$, liquid to gas density ratios of $683-1021$, Ohnesorge numbers of $0.003-0.12$, jet Reynolds numbers of $300-300000$. Jet primary breakup regimes, conditions for the onset of breakup and properties of waves were obtained using pulsed shadowgraph and holograph observations. The authors recognized three breakup regimes, namely bag breakup, multimode breakup and shear breakup, both functions of the Weber number, with little influence of the viscosity (at small Ohnesorge numbers, $Oh << 1$) on the transition of the breakup regime. For large Ohnesorge numbers, $Oh >> 1$, the breakup regime of non-turbulent LJIC is function of $We^{1/2}/Oh$. For non-turbulent LJIC, the authors noted drop velocity distributions after breakup were relatively independent of drop size, according Eq. 2.17 and Eq. 2.18, respectively for crossflow velocity and jet flow velocity directions,

$$\frac{u_p}{u_L} = \frac{u_p}{u_\infty (\rho_g/\rho_l)^{1/2}} = 6.4, \tag{2.17}$$

$$\frac{v_p}{v_{jet}} = 0.6. \tag{2.18}$$

Beside this, the ligaments diameters (comparable to the droplet sizes from the surface breakup), along the liquid column, increases with increasing distance from the jet diameter exit in transient state. Two breakup regimes of turbulent LJIC were found, aerodynamic breakup regime and turbulent breakup regime. A new dimensionless parameter, Faeth number, $Fa = We_\Lambda J^{1/3}$, was proposed to divide these two regimes: for $Fa > 17000$, turbulent breakup regime occurs and for $Fa < 17000$ aerodynamic breakup regime occurs. Breakup conditions for turbulent LJIC were correlated similarly to Sallam, Aalburg and Faeth (2003), Aalburg, Faeth and Sallam (2005), only different coefficients were obtained for the correlations of the droplet SMD, Eq. 2.19, and of the drop velocities, Eq. 2.20 and Eq. 2.21,

$$\frac{SMD}{\Lambda} = 0.56\left(\frac{y}{\Lambda}We_\Lambda^{1/2}\right)^{0.5}, \tag{2.19}$$

$$\frac{u_p}{u_L} = \frac{u_p}{u_\infty(\rho_g/\rho_l)^{1/2}} = 4.82, \tag{2.20}$$

$$\frac{v_p}{v_{jet}} = 0.75. \tag{2.21}$$

Experimental researches about LJIC have been made progressively (RAGUCCI; BELLOFIORE; CAVALIERE, 2007; NG; SANKARAKRISHNAN; SALLAM, 2008; PRAKASH et al., 2015; SINHA et al., 2015; BEHZAD; ASHGRIZ; MASHAYEK, 2015; ENAYATOLLAHI; NATES; ANDERSON, 2017), however the main experimental works of LJIC related to this dissertation were presented above, since breakup position of LJIC and diameter size in the primary breakup are the most important LJIC characteristics for this dissertation.

2.3 Numerical analysis of LJIC

Due to the complexity of LJIC, there are three approaches to solve numerically this spray configuration, depending on the desired results: Euler-Lagrange approach, Euler-Euler approach and hybrid approach (mixture of the last two approaches).

2.3.1 Euler-Lagrange approach

In Euler-Lagrange approach, one phase is treated as continuous that is evaluated in a fixed referential system (Eulerian referential), and the other phase is treated as discrete using a mobile referential system (Lagrangian referential) where discrete particles are tracked within the computational domain. Momentum, mass and energy exchanges between phases may be modeled whenever they are relevant for the specific problem. This approach is more suitable for immiscible phases flows with low concentrations of a phase over the other. Usually, particle (gaseous, liquid or solid) flows are treated in this approach. The computational cost is low for relative low numbers of immersed particles in the continuous phase; however it can be prohibitive for high amounts of discrete particles.

In LJIC, Euler-Lagrange approach treats the gas phase as continuous and liquid phase as discrete. In the jet exit, liquid column jet and its interaction with the air crossflow is not well represented by discrete liquid particles, since the flux of discrete particles do not represent a cohesive body as liquid column jet. However, far from the jet exit, liquid spray is better represented by discrete liquid particles, because in fact, in this region there is a predominance of liquid particles (drops). In the past, this approach was widely used to represent spray, mainly due to the computational cost limitations. Currently, the Euler-Lagrange approach is commonly used to obtain practical or preliminary results.

A numerical analysis of the LJIC was made using Euler-Lagrange approach by Reitz (1987). They injected liquid phase into the air crossflow using the blob method, which consists injecting discrete liquid drops with a diameter of the injector exit diameter order, with a frequency injection that conserves mass upstream of the injector exit. Drop collision and coalescence were accounted in the numerical computations. Breakup of the original droplets followed linear stability analysis, which was able to describe different breakup regimes. Different diameter for the generated droplets after breakup were calculated, relating the wavelength of unstable waves on the blob surface with the generated droplet diameters. Jet penetration was well correlated with the experimental work of Hiroyasu and Kadota (1974). The authors concluded drop size, also well correlated with experimental data, is found to be determined by a competition between drop breakup, drop coalescence and vaporization effects.

Euler-Lagrange approach was used with the Large Eddy Simulation (APTE; GOROKHOVSKI; MOIN, 2003), that is a turbulence closure model in which large scales are calculated and only small scales are modeled. Secondary breakup of the injected drop in crossflow was evaluated through a stochastic model in the form of the differential Fokker-Planck equation for the probability density function (PDF) of droplet radii. Parameters of the model were obtained according to the local Weber number, using two-way coupling between gas and liquid phases. The authors used LES simulation to provide accurate predictions of turbulent transport used in the estimation of the maximum stable diameter of droplets before breakup. Numerical results of jet penetration and spray angle agreed well with experimental work of Hiroyasu and Kadota (1974).

Balasubramanyam and Chen (2008) analyzed numerically a LJIC using Euler-Lagrange approach and $\kappa - \epsilon$ turbulence closure model. The entrance of the liquid particles from the injector exit inside the air crossflow followed the blob method. The grid size used to solve this problem was of 208000 elements, that is a relatively coarse grid for computational fluid dynamics. The authors obtained good comparisons with experimental results referent to droplet velocity along the air duct height. However, the jet penetration was not very well represented by the numerical results.

Jaegle et al. (2010) analyzed numerically LJIC using Euler-Lagrange approach with LES turbulence closure model. The authors modeled the jet column effect over the air crossflow through an imposition of a liquid jet curved column (virtually). Droplets were released from a breakup point at the top and along of the jet column, since the Euler-Lagrange is not able to predict dense region properly. A fully developed particle size distribution was assumed, where size droplets were selected in the injection instant. Liquid volume flux and the SMD were compared to experimental data (BECKER; HASSA, 2002) presenting reasonably agreement.

In a recent work (LI et al., 2017), LJIC in supersonic air flow ($Ma = 1.94$) using Euler-Lagrange approach was analyzed. Kelvin-Helmholtz breakup model was used to calculate drop stripping process and secondary breakup was simulated using Taylor Analogy Breakup (TAB) and Rayleigh-Taylor (RT) models concomitantly. Compressible flow and LES turbulence closure model were implemented in the code used, which included modified drag coefficient and breakup models depending on compressible effects and droplet deformation. The authors obtained good comparisons with experimental data referent to the jet penetration height and SMD along to the air flow direction.

2.3.2 Euler-Euler approach

Euler-Euler approach consists evaluating both phases, considered as continuous phases, under a fixed referential system. This approach is more suitable for immiscible flows and in the regions where phases have similar concentrations. The concept of volume fraction of the phases is assumed, so that different phases can not occupy the same place at the same time, unless in the interface. Advective transport equations for the phases (phase, if two-phase flow) are solved, ensuring the laws of classical mechanics be respected. This approach presents positive aspects in representing LJIC, such as: liquid breakup is calculated (without empirical modeling); interface is better represented along all domain; and droplet interaction with walls and other droplets (coalescence, bouncing) do not need additional modelings. However, these positive aspects are achieved only at high computational costs. Several methods have been developed in the sense of Euler-Euler approach, where each of them presents an extensive description, therefore just a summary of the results of some methods are discussed in the following.

Pure application of the Euler-Euler approach to LJIC (and other liquid jets configurations) has been possible recently due to the computer improvements and parallel computation strategies (many processors to solve a problem). The numerical solution of two-phase flows properly using Euler-Euler approach requires high number of elements. Shinjo and Umemura (2011) evaluated numerically diesel jet tip atomization, using VOF method, with a grid resolution sufficient to capture final droplet generated by surface tension, not considering turbulence and cavitation instabilities. Advection terms were solved using Cubic Interpolated Pseudo-particle (CIP) method. Two-phase flow was solved through Multi-interface Advection and Reconstruction Solver combined with a Level-Set method, while the surface tension was evaluated in all domain with the Continuum Surface Force (CSF) method. The minimum grid resolution required in the simulations performed by the authors was 400 million of elements in the JAXA supercomputer system. The temporal evolution of the jet breakup, the umbrella formation at the jet tip and the droplet formation along the jet due to the air interaction (airflow recirculation) were well capture in the simulations.

The Volume of Fluid method was used by Hirt and Nichols (1981) to study the formation and fragmentation of the spray from two impinging jets (CHEN et al., 2013). Adaptive Mesh Refinement (AMR) technique were used with VOF method for capture all physical characteristics of the impinging jets with high fidelity. The advection equation for the volume fraction, from the VOF method, was discretized using a robust Piecewise Linear Construction (PLIC) scheme, resulting in a good representation of the interface (POPINET, 2009). The surface tension term in momentum equation was discretized with a combination of a balanced force surface tension discretization and a height function curvature estimation, which presented a second order convergence rate, reducing considerably parasitic currents, that appears in the simulation of a stationary droplet in theoretical equilibrium (POPINET, 2009). These highly accurate schemes (with other high order spatial and temporal schemes) in combination with AMR, based on Octree meshes (one of the type meshes for AMR with the lowest computational cost), were able to capture all the flow patterns formed by impingement of two liquid jets, presenting good correlation with experimental data, such as: fine structures on their characteristics length scales; and various atomization modes, including sheet formation and rupture, atomization into ligaments and droplets. Although in his work AMR was used, it was necessary more than 1 million of cells to accurately solve spray formation of impinging jets (more than 134 million would be required in a uniform grid). LJIC presents smaller length scales than impinging jets, thus a higher number of cells would be necessary, even with the methodology used by Chen et al. (2013).

High fidelity simulations of Diesel jet were made by Arienti and Sussman (2015) using two interface tracking: ELVIRA method (EDWARD; JR; PUCKETT, 2004), for liquid-gas interface; and Coupled Level Set Moment of Fluid-CLSMOF (JEMISON et al., 2013), for interfaces with solid phases. Besides this, embedded boundary method was used to simulate walls, since boundary movement was involved. Diesel jet required a domain with a mesh size of $576 \times 64 \times 64$ (more than 2.3 million elements), which were solved using 128 SUN X6275 blades (total of 256 cores) in parallel. Droplet formation along to the jet were well described, though the calculated rate of injection and momentum were smaller than predict values from models based on the injection pressure and an assigned discharge rate. The differences in the rate of injection and momentum with the models may be related to the low mesh size used for the authors, in comparison to the mesh size used in the work of Shinjo and Umemura (2011).

Similar simulations of a fuel jet using an unstructured un-split VOF method was made (BRAVO et al., 2015) for realistic complex injector. The conditions analyzed consisted of a jet diameter of $90\mu m$, that released fuel in a quiescent chamber filled of Nitrogen at ambient conditions ($20\ bar$, $300\ K$) with $6.9\times10^4 < Re < 2.5\times10^5$ and $5.4\times10^4 < We < 1.25\times10^5$. For the turbulence closure model, the Smagorinsky LES model was used, which together with a good interface representation in VOF method required a 77 million grid points. Qualitative comparisons showed numerical breakup length was twice as long as that of the experimental images for lower injection pressure analyzed. These differences may arise due to the lack of some physical modeling, such as turbulence flow upstream exit injector, cavitation and fluid-structure interaction.

Due to the high number of elements required to solve LJIC (more than that used in liquid jet in a quiescent air chamber), Euler-Euler approach has been hardly employed. Li and Soteriou (2016) simulated LJIC using Euler-Euler approach and hybrid approach to be described in the following section. Euler-Euler approach employed consisted in Coupled Level Set Volume of Fluid (CLSVOF) method to capture spatial and temporal evolution of the liquid-air interface and sharp interface ghost fluid method to stably handle with the high liquid-air density ratios. The authors used an uniform grid with characteristic length size of the finite volume of $39 \mu m$, which corresponds to 503.3 million of elements, and an adaptive mesh refinement strategy (AMR), using three levels of refinement, resulting in 7.1 million of elements. For the uniform grid simulations 5000 cores were used and for AMR simulations, 24 cores, both on a supercomputer. Numerical results were well compared with experimental data qualitatively and quantitatively. The authors recognized that for uniform grid simulations, 503.3 million grid not only present high computational cost, but pose significant challenges in storing and processing the large set of simulation data. Therefore, for these simulations only two dimensional data (surfaces) were extracted from the results and analyzed.

2.3.3 Hybrid approach

Hybrid approach has been used recently to solve jet breakup as a better way to capture liquid-air interaction properly at more acceptable computational costs. Hybrid approach can be divided in two class: low dependence on transition models (higher computational cost); and high dependence on transition models (lower computational cost).

2.3.3.1 Low dependence on transition models

In this class of hybrid approach, the transition of a liquid portion from an Eulerian analysis to a Lagrangian analysis follows the concept of Herrmann (2010), that developed a parallel Eulerian-Lagrangian multi-scale coupling procedure for two-phase flows. The authors used Eulerian approach to solve liquid-air interactions until some criteria (size of liquid drops) and restrictions (grid capacity to solve interface interaction) be achieved, when Eulerian liquid portions are converted into Lagrangian liquid droplets. The transition method described by Herrmann (2010) consists in identifying an isolated liquid portion, which is converted into Lagrangian particle according to two criteria: size criterion, that select a liquid portion if its volume is lower than a threshold volume; and shape criterion, that select a liquid portion if its eccentricity is lower than a threshold eccentricity. Both criteria indicate that the liquid portion may not break after Lagrangian conversion. The simulations were performed using

Refined Level Set Grid (RLSG) method for transporting liquid-air interface in a parallel code (HERRMANN, 2008). Beside this, back transition (Lagrangian particle to Eulerian droplet) were considered in the simulations, based on the size of a coalesced drop. The applicability of the method was demonstrated with a detailed simulation of the atomization of a turbulent liquid jet, similar those obtained in pure Euler-Euler approach.

Following the concept of Herrmann (2010), small liquids structures formed by atomization were removed from Eulerian description and transformed into Lagrangian particles using CLSVOF method with block structured AMR (LI; ARIENTI; SOTERIOU, 2010). Three criteria were used to determine the eligibility of a liquid portion to be converted from Eulerian approach to Lagrangian approach: volume size, sphericity and maximum local concentration of droplet which the transformation to the Lagrangian phase can occur. Impinging jets and LJIC were analyzed using hybrid approach. For Impinging jets, the computational time was approximately 150 seconds per time step, considering time step was $0.66 \mu s$ and two levels of refinement were used, leading to a minimum grid size of $31.25\,\mu m$ (in a uniform grid, it leads more than 150 million of grid points). For LJIC, computational time was $300-400$ seconds per time step, considering time step was $0.17\,\mu s$ and a base grid more than 4 million of elements were used with three levels of refinement. Both simulations were performed on two 8-core, 32 Gb, 3000 MHz nodes with InfiniBand switch. Qualitatively, both simulations presented good comparisons with experimental data. Sauter Mean Diameter measurements in a plane and droplet distribution presented good correlation with experimental data, respectively for LJIC and Impinging jets. Compared to Euler-Euler approach, hybrid approach effectively reduces computational costs, even they are still high when low dependence on transition models are used.

2.3.3.2 High dependence on transition models

Euler-Lagrange approach with high dependence on transition models does not represent all the physics involved. However, this approach is able to determine many features of the LJIC nicely, such as: droplet distribution; droplet velocity; and jet height. The computational costs related to the high dependence on transition models in Euler-Lagrange approach is low, comparable with the numerical simulations from Lagrange approach. The advantages of the two separated approaches (Euler and Lagrange) is maintained, but some empirical models are needed. The precursor work related to this methodology applied to LJIC is attributed to Arienti et al. (2006). They implemented in the hybrid approach empirical correlations from Sallam, Aalburg and Faeth (2003) and Sallam et al. (2006), described in section 2.2. The methodology consisted in evaluated the empirical correlations for primary breakup at the top of the liquid jet and along the column of the liquid jet. The stripped mass from the liquid column was calculated using the surface breakup efficiency factor, Eq. 2.22,

$$\varepsilon = \frac{\dot{m}_l''}{\rho_l \bar{u}_p}, \tag{2.22}$$

where, $\bar{u}_p$ is the mean stream-wise droplet velocity, Eq. 2.23,

$$\bar{u}_p = C_u u_\infty \left(\rho_g/\rho_l\right)^{1/2}, \tag{2.23}$$

and C_u is an empirical constant, reported by Sallam, Aalburg and Faeth (2003) as $C_u = 6.4$ for $\rho_l/\rho_g > 500$. The primary breakup at the top of the liquid jet was calculated according described in the section 2.2, using the Eq. 2.9 (the authors assumed the empirical constant as 2.44 instead 2.6) and Eq. 2.24, respectively for the breakup height and the drop diameter,

$$\frac{d_p}{d_{jet}} = \left(1.5\lambda_b\right)^{1/3}, \tag{2.24}$$

where, $\lambda_b = \lambda_c/d_{jet}$ is the dimensionless wave length and λ_c is calculated from Eq. 2.5. Arienti and Soteriou (2007) presented numerical simulation using the same empirical correlations, except in the calculation of the drop diameter generated by the shear stripping along the column jet. They used a turbulent correlation instead the wave model by Reitz (1987) used by Arienti et al. (2006).

Following the application of high dependence on transition models in LJIC, numerical simulations of the LJIC considering film formation were performed using Hybrid approach, composed by VOF/HRIC method and Lagrangian approach (ARIENTI et al., 2011). In their work, a less arbitrary condition to shear breakup than that of the efficiency shear breakup concept was developed. The more realistic condition compares the aerodynamic forces over the surface, which tends to strip drops from the surface of the liquid column, and the surface tension forces, which tends to maintain a cohesive liquid column. Equation 2.25 is the mathematical condition for shear breakup to occur,

$$\rho_g|\vec{U}_g - \vec{U}_l|\kappa > C_\sigma \frac{\sigma}{d_p}, \tag{2.25}$$

where: $\vec{U}_g$ and $\vec{U}_l$ are the average vector velocity over cells neighboring the injection point, respectively for the gas phase and liquid phase; κ is the interface curvature; C_σ is a constant accounting the deficiency of the proposed model, set to 2.0; σ is the surface tension coefficient; and d_p is the diameter drop, Eq. 2.10. Besides column breakup and surface breakup, the authors modeled the film formation at the wall, film breakup and secondary breakup of the LJIC. The results agreed well with experimental velocity profiles, film thickness and SMD distribution.

Considering the potential of the Hybrid approach with high dependence on the transition models of obtaining realistic and fast numerical results in practical problems, in this dissertation a numerical modeling was developed in an unstructured grid code, following the methodology from Arienti et al. (2011) as base. Different schemes/models were implemented from the original methodology developed by Arienti et al. (2011), such as: secondary breakup models; density interpolation schemes; and advection schemes for VOF method for unstructured grid. All these differences along with the evaluation of the interactions between droplets-airflow (two-way) and droplets-droplets (four-way) were the main advance made in this work on the LJIC research using Hybrid approach. To the best of the knowledge of this author there is no published work that analyzed LJIC with this methodology, which is presented in the following.

CHAPTER III

MODELING AND METHODOLOGY

The general physical, mathematical and numerical modelings used in this work are described in this chapter.

3.1 Physical modeling

The adopted physical modeling follows the laws of classical mechanics. Therefore, the mass is conserved and the second law of Newton is used to represent momentum in the flows. The continuum mechanics concept was adopted, which means the thermodynamic properties are used to represent the physics in the microscopic level as mean properties in the macroscopic level, such as, density, viscosity, velocity, and pressure.

In the present work, liquid jet in crossflow (LJIC), whose schematic representation is shown in Fig. 2.1, is the principal configuration of two-phase flow studied (in verification and validation other two-phase flows were studied). These two-phase flows were evaluated considering immiscible fluids, i.e., the fluids do not form a mixture, but they can interpenetrate each other. Furthermore, mass transfer from one phase to the other phase was not accounted, i.e., evaporation are not considered. The interaction between the phases occurs in the interface, that is infinitesimally thin concerning the continuum mechanics. The surface tension coefficient is a relevant physical property to represent the interactions in the interface, modeling the surface tension force related to the discontinuous change in the physical properties at the interface.

About the adopted behavior for the fluids, three hypothesis were made: the fluid flows were considered incompressible, since density was not variable with the temperature and pressure changes in the studied ranges; Newtonian behavior was assumed to the fluids, considering the shear stress was proportional to the strain rate; and the flows were studied at the same temperature, isothermal flows. These three hypothesis impose the fluids physical properties are constants in each problem analyzed.

The smallest droplets were modeled as discrete spherical particles in Lagrangian referential. The physical modeling of the droplets motion follows Newton's second law. Thus, the droplets are transported by the fluid flow and may interact with the fluid flow and other droplets, when applicable.

The interaction between droplets may be important in the dense spray region (high concentration of droplets), whereas in the dilute spray region (low concentration of droplets), the droplet interaction is irrelevant. The interaction of the droplets between themselves can be of two kinds, considering binary collision: grazing collision and coalescence. In the grazing collision the droplets sizes are kept, but the subsequent velocities change. In the coalescence interaction, the two droplets become a bigger single droplet, and its velocity is also changed. In the Fig. 3.1 a schematic representation of these two interactions is shown. The condition for the droplet collision results in coalescence is the surface tension force dominate over the liquid inertia forces (REITZ, 2006). The ratio of these two forces is represented by the Weber number, thus it is expected high Weber numbers generate grazing collision instead of coalescence.

Finally, four boundary conditions were applied in the physical modeling of the studied problems:

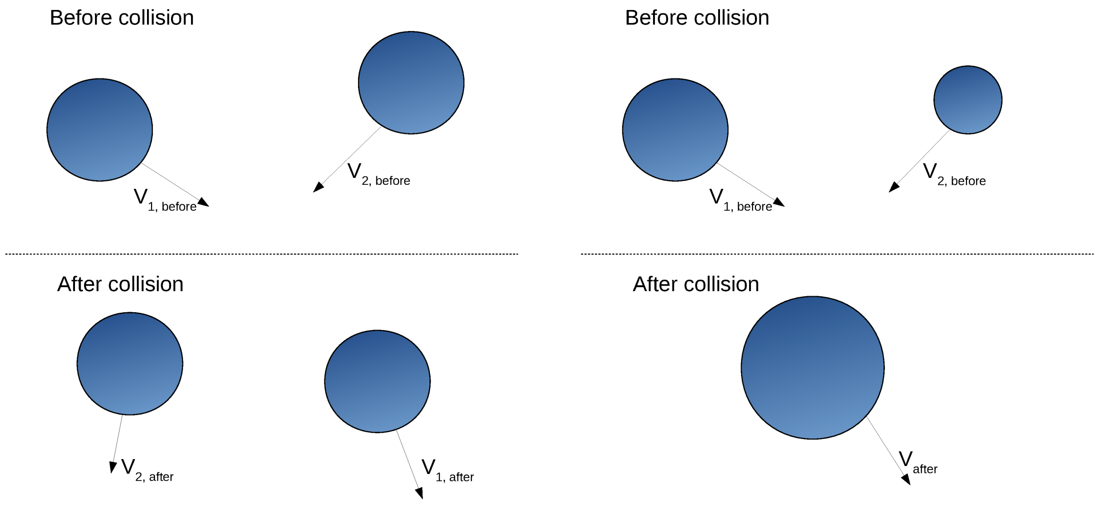

(a) Grazing collision. (b) Coalescence.

Figura 3.1 – Representation of the two assumed droplet interaction.

- walls, no-slip velocity, no mass flux for fluid and null derivative for pressure and volume fraction;
- symmetry, reflection of the values of all properties (velocity, pressure, volume fraction);
- inlet, normal velocity, null pressure derivative, and imposed value for volume fraction;
- and outlet, the pressure value is known, the velocity field is calculated, and the other properties are transported according to the flow velocity.

In the Lagrangian approach, escape boundary condition was applied to the particles in the outflow surface, while in the other boundaries, the reflect boundary condition was used, since in the experiments, evaluated wall film does not occur.

3.2 Mathematical modeling

The mathematical modeling used in this work, following the physical modeling previously presented, is composed of three parts, referring to Eulerian referential (fluids), Lagrangian referential (droplets), and empirical models (hybrid approach).

3.2.1 Eulerian referential

All transport equations for an Eulerian referential are presented using the integral form and the index notation. The discretization of the transport equations in the integral form using the finite volume method (FVM) (FERZIGER; PERIĆ, 2002) is more easily applicable. It is worth remembering that in the index notation, the index are 1, 2 and 3, indicating, respectively, the x, y and z axes and the variables in their respective axis. The terms with repeated index indicate a summation.

Since in this dissertation the LJIC were at turbulent regime and filtered equations were considered to model turbulent flows, the filtering of the momentum and mass balance equations were used to represent the physical modeling. The procedure to obtain the filtered equations under the taken hypothesis (incompressible, iso-thermal and Newtonian) is found in Ferziger and Perić (2002). Thus, Eq. 3.1 and Eq.3.2 are the mass and momentum equations respectively, recognizing that the variables are the filtered variables, even without the usual bar over the variable, in order to facilitate the notation. This set of equations are known as unsteady Reynolds averaged Navier-Stokes (URANS), because Reynolds (1895) was the first who derived the basis of the average mass and momentum balance equations for turbulent flows.

$$\int\limits_{sc} u_i n_i \cdot ds = 0, \tag{3.1}$$

$$\begin{aligned} &\frac{\partial}{\partial t}\int\limits_{cv} \rho u_i dv + \int\limits_{cs} \rho u_i u_j \cdot n_j ds = -\int\limits_{cs} p\delta_{ij} \cdot n_j ds + \int\limits_{cv} \rho g_i dv \\ &+\int\limits_{cs} \left[\mu\left(\frac{\partial u_i}{\partial x_j} + \frac{\partial u_j}{\partial x_i}\right) - \rho u_i' u_j'\right] \cdot n_j ds + \int\limits_{cv} \rho f_\alpha dv + \int\limits_{cv} \rho s_{u_i} dv + f_{st}, \end{aligned} \tag{3.2}$$

where: cs and cv stand for the control surface and control volume; δ_{ij} is the Kronecker delta; u_i are the velocity vector components; g_i are the gravity vector components; μ is the fluid dynamic viscosity; ρ is the fluid density; $u_i' u_j'$ is the filtered tensor of the fluctuating velocities, which is modeled in this work with the two-layer $k-\epsilon$ turbulence closure model (LAUNDER; SPALDING, 1974); f_{st} is the surface tension source term; $s_{u_i} = -\dfrac{n_d}{m_p}(F_{d_i})$ is the source term that represents the exchange of momentum, related to the drag force (described bellow), F_{d_i}, on droplets and the number density of a drop parcel, n_d; and f_α is the source term related to the change in the momentum when an Eulerian liquid portion is converted to a Lagrangian particle.

3.2.1.1 Turbulence closure model

The fluctuating velocities tensor is known as the Reynolds stress tensor, $\overline{\tau_{ij}} = -\rho u_i' u_j'$. The Reynolds stress tensor must be modeled, since the fluctuating velocities are unknowns. The Boussinesq (1877) hypothesis, that relates the Reynolds stress tensor with the mean velocity gradients, according Eq. 3.3, was used to model the Reynolds stress tensor,

$$\overline{\tau_{ij}} = \mu_t \left(\frac{\partial u_i}{\partial x_j} + \frac{\partial u_j}{\partial x_i} - \frac{2}{3}\rho \delta_{ij} k \right), \tag{3.3}$$

where: μ_t is the eddy-viscosity and k is the turbulent kinetic energy, defined as, Eq. 3.4,

$$k = \frac{1}{2} u_i' u_i', \tag{3.4}$$

which is the half of the summation of the main diagonal of the Reynolds stress tensor.

The eddy-viscosity, μ_t, and the turbulent kinetic energy, k, are unknown. Therefore, a turbulence closure model is required to solve URANS equations. The semi-empirical two-layer $k - \epsilon$ turbulence closure model (LAUNDER; SPALDING, 1974) was used in this work, since it provides robustness, economy and reasonable accuracy for both the core flow and the flow near the walls. This model consists on a combination of the two transport equations model and the one transport equation model, that are used to represent the turbulent flow region and the flow region affected by the viscous effects, respectively. Eddy viscosity that appears in the momentum equation, Eq. 3.2, is obtained through the solution of the transport equations and other empirical equations, presented bellow. The transport equations of the turbulent kinetic energy, k, and the dissipation rate of the turbulent kinetic energy, ϵ, are expressed, respectively by the Eq. 3.5 and Eq. 3.6,

$$\begin{aligned}&\frac{\partial}{\partial t}\int_{vc}\rho k dv+\int_{sc}\rho k u_j\cdot n_j ds=\int_{sc}\left[\left(\mu+\frac{\mu_t}{\sigma_k}\right)\frac{\partial k}{\partial x_j}\right]\cdot n_j ds+\\&+\int_{vc}\mu_t\left(\frac{\partial u_i}{\partial x_j}+\frac{\partial u_j}{\partial x_i}\right)\frac{\partial u_i}{\partial x_j}dv-\int_{vc}\rho\epsilon dv,\end{aligned}\tag{3.5}$$

$$\begin{aligned}&\frac{\partial}{\partial t}\int_{vc}\rho\epsilon dv+\int_{sc}\rho\epsilon u_j\cdot n_j ds=\int_{vc}C_{\epsilon 1}\frac{\epsilon}{k}\mu_t\left(\frac{\partial u_i}{\partial x_j}+\frac{\partial u_j}{\partial x_i}\right)\frac{\partial u_i}{\partial x_j}dv+\\&-\int_{vc}\rho C_{\epsilon 2}\frac{\epsilon^2}{k}dv+\int_{sc}\left(\frac{\mu_t}{\sigma_\epsilon}\frac{\partial k}{\partial x_j}\right)\cdot n_j ds,\end{aligned}\tag{3.6}$$

for the two equations model. For the one equation model, the k equation is remained while the ϵ variable is obtained through an algebraic equation, Eq.3.7,

$$\epsilon=\frac{k^{3/2}}{l_\epsilon}.\tag{3.7}$$

The length scale in Eq. 3.7 is computed through Eq. 3.8 (CHEN; PATEL, 1988),

$$l_\epsilon=yC_l\left(1-e^{-Re_y/A_\epsilon}\right).\tag{3.8}$$

The turbulent Reynolds number, Re_y, is defined as, Eq. 3.9,

$$Re_y=\frac{\rho y\sqrt{k}}{\mu},\tag{3.9}$$

where y is the distance from the wall to the center of a finite volume. In the region strongly affected by the viscous effects, $Re_y < Re_y*$ and in the fully turbulent region, $Re_y > Re_y*$, where $Re_y* = 200$.

The eddy-viscosity is calculated using different equations depending on the region of the flow, viscous affected or fully turbulent. For the region strongly affected by the viscous effects and the fully turbulent region, the eddy-viscosity is calculated using, respectively the Eq. 3.10 and Eq. 3.11,

$$\mu_{t,1eq}=\rho C_\mu l_\mu\sqrt{k},\tag{3.10}$$

$$\mu_{t,2eq} = \rho C_\mu \frac{k^2}{\epsilon}. \tag{3.11}$$

In Eq. 3.10, the length scale l_μ is calculated from Eq. 3.12 (CHEN; PATEL, 1988),

$$l_\mu = y C_l \left(1 - e^{-Re_y/A_\mu}\right). \tag{3.12}$$

All the constants presented in the equations above (Eq. 3.5 to Eq. 3.12) were taken from Ferziger and Perić (2002) and Chen and Patel (1988), and their values are as follows:

- $C_{\epsilon 1} = 1.44$;
- $C_{\epsilon 2} = 1.92$;
- $\sigma_\epsilon = 1.3$;
- $\sigma_k = 1.0$;
- $C_\mu = 0.09$;
- $C_l = 0.4187 C_\mu^{-3/4}$;
- $A_\epsilon = 2C_l$;
- $A_\mu = 70$.

The models transition imposes a smooth way to switch between the two equations for the eddy viscosity. Therefore, Eq. 3.13 is used to prevent solution divergence when the solution of the two models do not match. Thus,

$$\mu_t = \lambda_\epsilon \mu_{t,2eq} + (1 - \lambda_\epsilon)\, \mu_{t,1eq}, \tag{3.13}$$

where, the blending function λ_ϵ is calculated through the Eq. 3.14,

$$\lambda_\epsilon = \frac{1}{2}\left[1 + tanh\left(\frac{Re_y - Re_y*}{A}\right)\right]. \tag{3.14}$$

The constant $A = \dfrac{0.20Re_y*}{tanh^{-1}(0.98)}$ establishes the width of the blending function.

Since no wall functions are used, a refined grid resolution is required close to the walls, with $y^+ \approx 1$. The proper solution of the boundary layer is fundamental because the height of the liquid column jet is strongly influenced by the velocity profile.

3.2.1.2 Two-phase model

The two phase-flow is solved as one fluid with different physical properties, following the concept of the VOF method (UBBINK, 1997). A volume fraction variable is defined as the ratio of the liquid volume and the total volume in a finite volume, $\left(\alpha = \dfrac{V_l}{V_l + V_g}\right)$. This scalar variable is bounded with $0 \leq \alpha \leq 1$ and indicates which phase is present in a specific point of the domain. In this work, the liquid phase is represented by $\alpha = 1$, whereas the gas phase by $\alpha = 0$. Density and viscosity in mass and momentum equations are weighted according to the volume fraction in the specific finite volume, respectively Eq. 3.15 and Eq. 3.16,

$$\rho = (1-\alpha)\rho_g + \alpha\rho_l, \tag{3.15}$$

$$\mu = (1-\alpha)\mu_g + \alpha\mu_l, \tag{3.16}$$

where the subscripts g and l indicate gas and liquid phases, respectively. Remembering in this work both phases are assumed incompressible, thus ρ_l and ρ_g are constant. The transport equation for the volume fraction (Eq. 3.17) is obtained from the continuity equation for individual phases, using density relation with the volume fraction, Eq. 3.15,

$$\frac{\partial}{\partial t}\int_{cv} \alpha dv + \int_{sc} \alpha u_j \cdot n_j ds = s_\alpha, \tag{3.17}$$

where s_α is the source term related to the conversion of Eulerian droplets to Lagrangian droplets, being calculated as the ratio of the liquid volume, V_l, and the volume of the analyzed finite volume, V, per time step (ARIENTI et al., 2011), Eq.3.18,

$$s_\alpha = -\frac{V_l}{V\Delta t} = -\frac{\alpha}{\Delta t}. \tag{3.18}$$

Since the phases are considered incompressible, volume is conserved in the calculations, while mass is not conserved.

The source term assume positive signal whether a Lagrangian droplet must be converted to the Eulerian approach. The source term related to the changes in the momentum is defined according, Eq. 3.19,

$$f_\alpha = -\frac{V_l\vec{v}_d}{V\Delta t} = -\frac{\alpha\vec{v}_d}{\Delta t}, \tag{3.19}$$

considering an amount of momentum is lost in the conversion; the $\vec{v}_d$ is the velocity vector in the cell in which the conversion happened.

Temporal changes in the phases location are evaluated through Eq. 3.17, so that the interface is placed in cells wherein $0 < \alpha < 1$. The higher the number of cells in the interface vicinity, the better the interface is described, despite the different interpolation methods (which are described bellow) for the advection term in the scalar VOF equation.

The interactions at the interface are modeled through the surface tension force, which is physically discontinuous and defined only at the liquid-gas interface. However, from a numerical point of view, this effect must be mathematically modeled as continuous. The Continuum Surface Force model (BRACKBILL; KOTHE; ZEMACH, 1992) is used to describe the source term due to the surface tension force as a continuous force in the momentum equation, Eq. 3.2. Thus, in the VOF method, this source term is related to the volume fraction gradient represented in the integral form, the interface curvature and the surface tension coefficient of the phases pair, Eq. 3.20,

$$f_{st} = \sigma\kappa \int\limits_{sc} \alpha n_j ds. \tag{3.20}$$

The interface curvature can be obtained from the divergence of the unit vector to the interface (UBBINK, 1997), which is calculated as the unit vector of the gradient of the volume fraction (α), according to Eq. 3.21,

$$\kappa = -\nabla \cdot \left(\frac{\nabla \alpha}{|\nabla \alpha|} \right). \tag{3.21}$$

The description of the mathematical modeling for Lagrangian referential required to the hybrid approach applied to the LJIC problems is presented bellow.

3.2.2 Lagrangian referential

Following the adopted physical modeling, when the VOF method is not suitable to guarantee global features of the gas-liquid interface in the grid size (usually lower than 3 million of elements), droplets are used to represent the liquid phase as discrete entities. Therefore, Lagrangian calculations are involved in the simulations to represent properly the discrete droplets.

The current velocity and position of the droplets are calculated using the ordinary differential equations of the motion, respectively Eq. 3.22 and Eq. 3.23,

$$m_p \frac{du_{p_i}}{dt} = F_d + F_{w,b}, \tag{3.22}$$

$$\frac{dx_{p_i}}{dt} = u_{p_i}, \tag{3.23}$$

In these equations, the subscript i indicates the three components of the velocity vector; the subscript p indicates that the variable is related to the discrete particle; u and x are the velocity and position variables; m represents mass. Only the drag force, F_d, and the combined buoyancy-weight force, $F_{w,b}$, were considered in this work, being represented by the Eq. 3.24 and Eq. 3.25, respectively,

$$F_d = m_p \frac{3\rho C_D}{4\rho_p d_p} \left(u_{i,t} - u_{p_i} \right), \tag{3.24}$$

$$F_{w,b} = \left(1 - \frac{\rho}{\rho_p}\right) m_p g_i. \tag{3.25}$$

In Eq. 3.24 the $u_{i,t}$ is the instantaneous fluid velocity, calculated as filtered velocity plus a fluctuating component, $u_{i,t} = u_i + u_i'$. This fluctuating component of the velocity is obtained from the Langevin dispersion model proposed by Sommerfeld (2001) and the filtered fluid velocity must be interpolated to the particle position. The drag coefficient, C_D, is calculated using two correlations: correlation of Schiller and Naumann (1935) and correlation of Feng and Michaelides (2001). The empirical correlation of Schiller and Naumann (1935), Eq. 3.26, was used for rigid spherical droplets,

$$\begin{aligned} &Re_p < 1000 \rightarrow C_D = \frac{24}{Re_p}\left(1 + 0.15 Re_p^{0.687}\right) \\ &Re_p > 1000 \rightarrow C_D = 0.424. \end{aligned} \tag{3.26}$$

The Reynolds number of the discrete particle is calculated according Eq. 3.27,

$$Re_p = \frac{\rho |u_i - u_{p_i}| d_p}{\mu}. \tag{3.27}$$

The correlation of Feng and Michaelides (2001) combined with the correlation of Dahms and Oefelein (2016), Eq. 3.28,

$$\begin{aligned} &for\, 1000 \geq Re_p > 5 \\ &C_D = 17.0 Re_p^{-2/3}\left(\frac{4}{\lambda + 2}\right) + \frac{24}{Re_p}\left(1 + 0.15 Re_p^{0.687}\right)\left(\frac{\lambda - 2}{\lambda + 2}\right), \\ &for\, 0 \leq Re_p \leq 5 \\ &C_D = \frac{8.0}{Re_p}\left(\frac{3\lambda + 2}{\lambda + 1}\right)\left(1 + 0.05\left(\frac{3\lambda + 2}{\lambda + 1}\right) Re_p\right) - 0.01\left(\frac{3\lambda + 2}{\lambda + 1}\right) Re_p ln(Re_p), \end{aligned} \tag{3.28}$$

which considers the viscous flow inside the liquid droplets and droplet distortion, was also used with the purpose of verifying the influence of a drag coefficient's correlation that takes account the viscous flow inside a liquid droplet and droplet distortion on the spray formation in the LJIC.

In this work, interactions between droplets were evaluated. The possible types of interaction between droplets, as assumed in the physical modeling, are grazing collision and coalescence. The collision occurrence and the result of the collision is modeled by the stochastic method of Reitz (1987). The method considers collision can occur only with a pair of parcels (one parcel represents many real droplets with the same volume and velocity) at the same numeric finite volume. When collision is identified, the collision type is determined comparing the collision impact parameter b, Eq. 3.29, with the critical collision impact parameter, b_{crit}, Eq. 3.30.

$$b = (r_1 + r_2)\sqrt{Y}, \tag{3.29}$$

$$b_{crit} = (r_1 + r_2)\sqrt{min\left(1.0, \frac{2.4\left(r_r^3 - 2.4r_r^2 + 2.7r_r\right)}{We_c}\right)}. \tag{3.30}$$

In Eq. 3.29 and Eq. 3.30, Y is a random number between 0 and 1; r_1 and r_2 are respectively the radius of the bigger parcel and of the smaller parcel involved in the collision; and We_c is the collisional Weber number, calculated from the Eq. 3.31,

$$We_c = \frac{\rho U_{rel}^2 \bar{D}}{\sigma}, \tag{3.31}$$

where: U_{rel} is the relative velocity between the two parcels, and $\bar{D}$ is the mean diameter of the two parcels.

3.2.3 Primary breakup and secondary breakup models

The liquid portion conversion from an Eulerian referential to a Lagrangian referential was accomplished considering two forms of primary breakup in LJIC: column breakup and shear breakup. The description of these two kinds of primary breakup were previously presented in the section 2.2.

The column breakup model establishes a height of the liquid column where the entire liquid column is disrupted, forming droplets. According to Wu, Kirkendall and Fuller (1997) and Sallam, Aalburg and Faeth (2003), the height breakup can be estimated through Eq.

2.2 and Eq. 2.9. This two column breakup correlations are evaluated in the present work, verifying the most appropriate column breakup correlation. The diameter of the created droplet are expressed by Eq. 2.24.

The shear breakup empirical model can be relevant for Weber number higher than 12. In this condition droplets are stripped off from the liquid column surface. The condition used in this work for the droplets detachment considers a balance of the aerodynamic forces, improving the droplet detachment probability, and the surface tension forces reducing the droplet detachment probability (ARIENTI et al., 2011), Eq. 2.25. The diameters of the droplets produced by the shear breakup was calculated through Eq. 2.10 and Eq. 2.10 (SALLAM; AALBURG; FAETH, 2003).

The secondary breakup was modeled using the original Taylor analogy breakup (TAB) model (O'ROURKE; AMSDEN, 1987) and the accurate balance equation Taylor analogy breakup model from Dahms and Oefelein (2016), which accounts properly the distortion of the droplets. The accurate balance TAB model is referenced in this work as AB-TAB model.

In the original TAB model (O'ROURKE; AMSDEN, 1987), the secondary breakup of an oscillating and distorting droplet is associated with a mass-spring-damper system, represented through the Fig. 3.2 and the Eq. 3.32,

$$\frac{d^2x}{dt^2} + \frac{c}{m}\frac{dx}{dt} + \frac{k}{m}x = \frac{F}{m}, \tag{3.32}$$

where: m is the mass of the system; x is the displacement of the pole for the distorted droplet from the pole for the undistorted droplet; k is the spring stiffness; c is the damping coefficient; and F is the external force applied to the mass. Table 3.1 showed the association of the terms of the mass-spring-damper mass system equation with the oscillating and distorting droplet. In Tab. 3.1, r_p is the droplet radius; u is the relative velocity between the droplet and the surrounding gas; C_F, C_k and C_d are dimensionless constantes, whose empirical values are, respectively, $1/3$, 8 and 5. These constants matches experimental value of the critical Weber number for Newtonian liquids with low viscosity and the known oscillation dynamics of

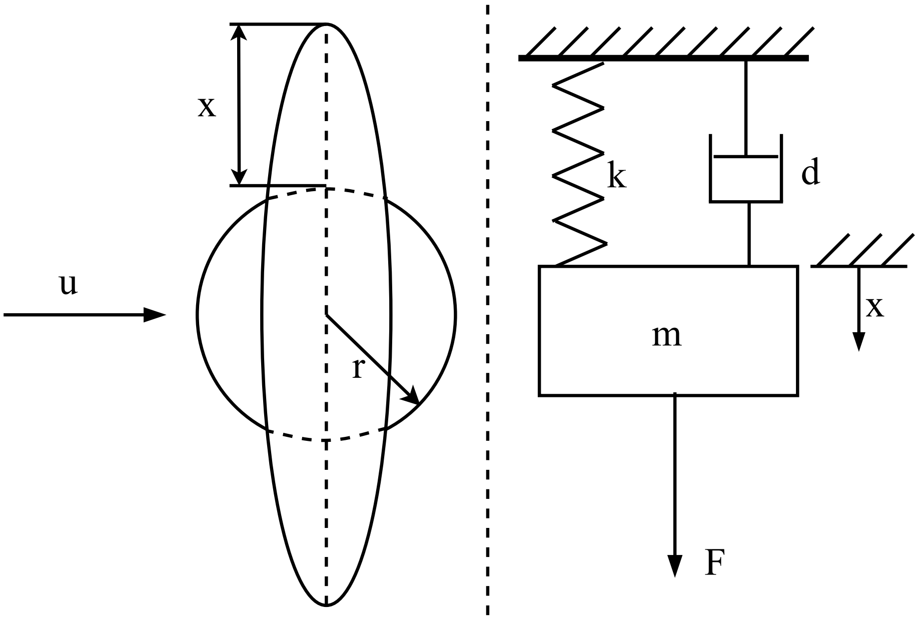

Figura 3.2 – Schematic representation of the Taylor Analogy Breakup.

Tabela 3.1 – The analogy between the mass-spring-damper system and a oscillating and distorting droplet.

mass-spring-damper system	oscillating and distorting droplet	mathematical equivalence
spring force	surface tension force	$\frac{k}{m} = C_k \frac{\sigma}{\rho_l r_p^3}$
damping force	viscous force	$\frac{c}{m} = C_d \frac{\mu_l}{\rho_l r_p^2}$
external force	drag force	$\frac{F}{m} = C_F \frac{\rho_g u^2}{\rho_l r_p}$

inviscid and damped viscous drops (DAHMS; OEFELEIN, 2016). A non-dimensional distortion equation can be obtained, Eq. 3.33,

$$\begin{aligned} y(t) = & We_{crit} + \\ & exp\left(-\frac{\Delta t}{t_D}\right)\left[(y_0 - We_{crit})\, cos(\omega \Delta t) + \frac{1}{\omega}\left(\frac{dy_0}{dt} + \frac{y_0 - We_{crit}}{t_D}\right) sin(\omega \Delta t)\right], \end{aligned} \tag{3.33}$$

using $y = \frac{x}{C_b r_p}$ as dimensionless distortion. The C_b constant is set 0.5. In Eq. 3.33, y_0 and $\frac{dy_0}{dt}$ are respectively the initial values of the drop distortion and of the distortion velocity. The critical Weber number, We_{crit}, is proportional to the effective Weber number of the droplet,

We^*, which is calculated as function of the Weber number, We, and the Ohnesorge number, Oh, of the droplet. The critical Weber number, the effective Weber number, the droplet Weber number and the Ohnesorge number are expressed by Eq. 3.34, Eq. 3.35, Eq. 3.36 and Eq. 3.37, respectively:

$$We_{crit} = \frac{C_F}{C_k C_b} We, \tag{3.34}$$

$$We^* = \frac{We}{1 + 1.077 Oh^{1.6}}, \tag{3.35}$$

$$We = \frac{\rho_g u^2 r_p}{\sigma}, \tag{3.36}$$

$$Oh = \frac{\mu_l}{\sqrt{\rho_l d_p \sigma}}. \tag{3.37}$$

The oscillating damping time, t_D, and the drop oscillating frequency, ω, are calculated by Eq. 3.38 and Eq. 3.39,

$$t_D = \frac{2\rho_l r_d^2}{C_d \mu_l}, \tag{3.38}$$

$$\omega = \sqrt{C_k \frac{\sigma}{\rho_l r_p^3} - \frac{1}{t_D^2}}. \tag{3.39}$$

The distortion velocity was given by O'Rourke and Amsden (1987), according Eq. 3.40,

$$\begin{aligned} \frac{dy}{dt} &= \frac{We_{crit} - y}{t_D} + \\ &exp\left(-\frac{\Delta t}{t_D}\right)\left[\frac{1}{\omega}\left(\frac{dy_0}{dt} + \frac{y_0 - We_{crit}}{t_D}\right) cos(\omega \Delta t) - (y_0 - We_{crit})\, sin(\omega \Delta t)\right], \end{aligned} \tag{3.40}$$

The breakup condition is established when the dimensionless drop distortion, y, exceed the unity. However, a breakup time is more convenient to verify the occasional moment of the droplet breakup than the dimensionless drop distortion. Thus, an expression for the breakup time, t_B, can be obtained considering the drop distortion is equal the unity, $y = 1$, according the Eq. 3.41,

$$t_B = \frac{1}{\omega}\left[cos\left(\frac{1 - We_{crit}}{A}\right) - \phi\right], \tag{3.41}$$

where, the parameters A and ϕ are calculated, respectively, by the Eq. 3.42 and Eq. 3.43:

$$A = \sqrt{(y - We_{crit})^2 + \left(\frac{1}{\omega}\frac{dy}{dt}\right)^2}, \tag{3.42}$$

$$\phi = arctg\left(\frac{1}{\omega(y - We_{crit})}\frac{dy}{dt}\right). \tag{3.43}$$

The diameters and the velocities of the droplets created in the secondary breakup are calculated considering the energy conservation before and after the breakup, as presented in the work of O'Rourke and Amsden (1987). However, some empirical constants were assumed to calculate the diameters and velocities of the droplets created in the secondary breakup.

The AB-TAB model, developed by Dahms and Oefelein (2016), follows the main concepts of the original TAB model. However, a refined balance of the mass, momentum, energy and surface energy equations were assured in the calculation of the diameters and velocities of the droplets generated from the secondary breakup, not only the energy equation as made by O'Rourke and Amsden (1987). The time breakup is realistically estimated, since the oscillation energy of droplets is accounted properly, not considering the empirical value of the critical Weber number (DAHMS; OEFELEIN, 2016). Other secondary breakup models, for example ETAB (TANNER, 1997), had been already developed aiming to solve some under predictions of the diameters of the generated droplets and some inconsistencies on the spray angle prediction, of the original TAB model. Nevertheless, empirical constants was also considered. Therefore, the AB-TAB model is physically more consistent to describe the secondary breakup than the original TAB model and similar models that make use of empirical constants.

3.3 Numerical modeling

The numerical modeling consists on the description of all methods used to discretize and solve equations in the Eulerian referential (including the VOF method) and Lagrangian referential, that when properly combined constitute the numerical modeling of the hybrid approach.

3.3.1 Eulerian referential

The numerical modeling used in this work is based on the finite volume method (FVM), developed by Patankar (1980), to discretize the transport equations presented in section 3.2. Two fundamental premises of the FVM are important to recall (FERZIGER; PERIĆ, 2002): the variable values in the finite volume are constants, assuming them as medium values; and the variable values at the finite volume faces are considered as medium values located at the face centroid.

A collocated unstructured grid was used as basis for the discretization. Thus, Fig. 3.3 represents two unstructured finite volumes in two dimensions. This figure was used as reference for all discretizations. Since the normal face between two finite volumes is not necessarily aligned to the vectors $\vec{dr}_L$ and $\vec{dr}_R$, in some terms of the transport equations geometric calculus must be applied in the discretization. The discretization of three recurring terms present in all transport equations are described: temporal, advective and diffusion terms. The discretization of these terms were exemplified using particular terms of the equations for better understanding of the discretization process.

3.3.1.1 Temporal term

Considering the left finite volume element, Fig. 3.3, temporal term can be discretized using a second-order three level method (FERZIGER; PERIĆ, 2002). Taking as example the

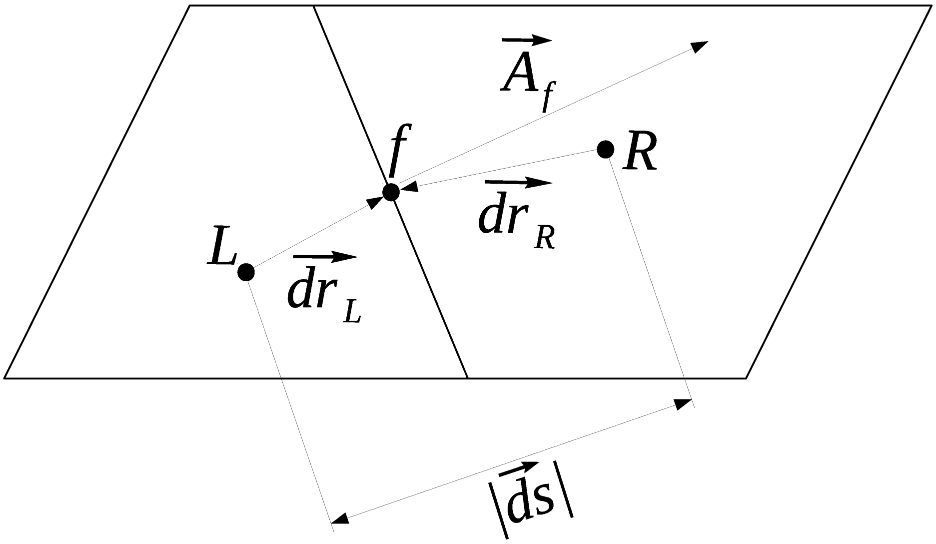

Figura 3.3 – Schematic diagram of two finite volumes of an unstructured grid.

first term of the Eq. 3.2, temporal discretization is given by the Eq. 3.44,

$$\left(\frac{\partial}{\partial t}\int_{vc}\rho u_i dv\right)_L = \frac{3\left(\rho_L u_{iL}\right)^{n+1} - 4\left(\rho_L u_{iL}\right)^{n} + \left(\rho_L u_{iL}\right)^{n-1}}{2\Delta t}, \tag{3.44}$$

where: n indicates the current time (t); $n+1$ indicates values at the future time $(t+\Delta t)$; and $n-1$ indicates the values at the previous time $(t-\Delta t)$.

Hereafter, in the next discretizations, the values at $n+1$ $(t+\Delta t)$ are presented without the superscript $n+1$ for simplicity. Beside this, in the discretizations of the terms presented bellow, the variables are evaluated at the future time, unless it is mentioned. In other words, the variables were calculated implicitly.

3.3.1.2 Advection term

The second term of the Eq. 3.2 was used to exemplify the advective term discretization, Eq. 3.45,

$$\left(\int_{sc}\rho u_i u_j \cdot n_j ds\right)_L = \sum_{m=1}^{nf}\rho_f^n u_i|_f u_j{}^n|_f \cdot A_{f_j}, \tag{3.45}$$

where, nf is the number of faces of the finite volume considered. The face value of the variable calculated, in this case $u_i|_f$, can be calculated using first order upwind, second order upwind or central differences schemes, whose calculations are found in Ferziger and Perić (2002), Fluent (2013). The mass flux, $\rho_f^n {u_j}^n|_f \cdot A_{f_j}$, used in this discretization is from the current temporal calculation (variables known).

3.3.1.3 Diffusion term

The diffusion term can be calculated through Eq. 3.46, using the first term of the right side of the Eq. 3.5 as example,

$$\left(\int\limits_{sc} \left[\left(\mu + \frac{\mu_t}{\sigma_k}\right)\frac{\partial k}{\partial x_j}\right] \cdot n_j ds\right)_L = \sum_{m=1}^{nf} \left(\mu + \frac{\mu_t}{\sigma_k}\right)\left.\frac{\partial k}{\partial x_j}\right|_f \cdot A_{f_j}. \tag{3.46}$$

Primary diffusion and secondary diffusion must be considered (MATHUR; MURTHY, 1997) in the gradient that appears in a diffusion term of the transport equations. Thus, using the diffusion term of the turbulent kinetic energy equation, the gradient in it, $D_f = \left.\frac{\partial k}{\partial x_j}\right|_f \cdot A_{f_j}$, is calculated as, Eq. 3.47,

$$D_f = \frac{(k_R - k_L)}{|\vec{ds}|}\frac{\vec{A_f} \cdot \vec{A_f}}{\vec{A_f} \cdot \vec{e_s}} + \left(\overline{\nabla k} \cdot \vec{A_f} - \overline{\nabla k} \cdot \vec{e_s}\frac{\vec{A_f} \cdot \vec{A_f}}{\vec{A_f} \cdot \vec{e_s}}\right). \tag{3.47}$$

In Eq. 3.47, the first term on the right side is the primary diffusion and the second term is the secondary diffusion. All the variables comes from Fig. 3.3, where: $\vec{e_s} = \frac{\vec{ds}}{|\vec{ds}|}$ is the unit vector from centroid of L finite volume to the centroid of the R finite volume; and $\overline{\nabla k}$ is the average gradients calculated from the adjacent finite volumes.

3.3.1.4 Advection scheme for VOF method

The transport equation for the VOF method can be solved implicitly or explicitly. In case of explicit solution, first order scheme integration was used. Despite the simplicity of the VOF transport equation, the abrupt change in the fluid properties, whose ratio is of $\mathcal{O}(1000)$, arises some difficulties related to the advection term.

The advection term of the VOF transport equation is not so simple to discretize, in such a way that usual interpolation schemes, such as central differences scheme and upwind schemes, lead to an oscillating or very diffusive interface. Therefore, specific discretization schemes are needed to solve the advection term of the VOF transport equation. Two kinds of discretization schemes for the advection term can be found in the literature: geometric discretization schemes, such as PLIC, based on the work of Youngs (1982); and algebraic discretization, such as CICSAM (UBBINK; ISSA, 1999) and HRIC (MUZAFERIJA et al., 1998).

The geometric schemes usually present better interface description at a higher computational cost when compared to the algebraic discretization schemes. Prioritizing lower computational cost with relative good interface representation, three algebraic discretization schemes were implemented: compressive interface capturing scheme for arbitrary meshes (CICSAM), high resolution interface capturing (HRIC) and modified HRIC (FLUENT, 2013). All these schemes are based on blending upwind and downwind schemes through some criteria. In this dissertation only CICSAM scheme is described, since there are few changes in the original implementation (UBBINK; ISSA, 1999), while the implementation of the HRIC scheme and the modified HRIC schemes followed strictly the algorithm presented in the original works (MUZAFERIJA et al., 1998; FLUENT, 2013).

CICSAM scheme, as well as HRIC and modified HRIC schemes, are used to determine the face values of the volume fraction variable, α_f. Normalized Variable Diagram of Leonard (1991) is the base to obtain the face values. Donor, acceptor cells and upwind point are used to obtain the face value of the volume fraction which are used in the advective term discretization. All these variables are obtained following the pseudo-code of the CICSAM scheme, presented in the Algorithm 1. In this pseudo-algorithm, the $\sim$ represents normalized variables and ϵ is a tiny number, in the order of zero machine, to avoid divisions by zero. Subscripts A and D represent the Acceptor and Donor cells, respectively, which can be found based on the sign of

Algorithm 1 CICSAM scheme on arbitrary meshes

```
$\alpha_U \leftarrow \alpha_D + \nabla\alpha_D \cdot (\vec{x}_A - \vec{x}_D)$
$\alpha_U \leftarrow \max(\alpha_U, 0)$
$\alpha_U \leftarrow \min(\alpha_U, 1)$
$\tilde{\alpha}_D \leftarrow \dfrac{\alpha_D - \alpha_U}{\alpha_A - \alpha_U + \epsilon}$
$\theta \leftarrow \arccos\left(\dfrac{\nabla\alpha_D \cdot (\vec{x}_A - \vec{x}_D)}{|\nabla\alpha_D + \epsilon| \cdot |\vec{x}_A - \vec{x}_D|}\right)$
$\gamma_f \leftarrow \min\left(\dfrac{1+\cos 2\theta}{2}, 1\right)$
if $\tilde{\alpha}_D < 0$ or $\tilde{\alpha}_D > 1$ then
    $\alpha_{CBC} \leftarrow \tilde{\alpha}_D$
    $\alpha_{UQ} \leftarrow \tilde{\alpha}_D$
else
    $\alpha_{CBC} \leftarrow \min\left(1, \dfrac{\tilde{\alpha}_D}{\mathsf{Co}}\right)$
    $\alpha_{UQ} \leftarrow \min\left(\alpha_{CBC}, 8\,\mathsf{Co}\,\tilde{\alpha}_D + (1-\mathsf{Co})\dfrac{6\tilde{\alpha}_D + 3}{8}\right)$
end if
$\tilde{\alpha}_f \leftarrow \gamma_f \alpha_{CBC} + (1-\gamma_f)\alpha_{UQ}$
$\alpha_f \leftarrow \alpha_U + (\alpha_A - \alpha_U)\tilde{\alpha}_f$
```

mass flow rate through the face between both cells. Co represents the cell Courant number:

$$Co = \sum_{f=1}^{N} \max\left(\vec{u}_f \cdot \vec{n} A_f \tfrac{\Delta t}{V_{cv}}, 0\right), \tag{3.48}$$

For the evaluation of the gradients in the equations above, the Node-Averaged-Gauss (NAG) scheme was used, as proposed by Maric, Marschall and Bothe (2013).

3.3.1.5 Pressure-velocity coupling

In incompressible flows there is no thermodynamic equation for pressure. The three components of momentum equation Eq. 3.2 are used to solve the three components of the fluid velocity, while the continuity equation, Eq. 3.1, works as a kinematic restriction that can be related to the pressure gradient. Thus, a pressure equation is generated through the continuity equation so that the mass balance is satisfied. This procedure is related to the pressure-velocity coupling.

The Semi-Implicit Method for Pressure Linked Equations, SIMPLE was used to ensure pressure-velocity coupling. This method was designed for segregated solution, that is pressure is solved separately from the velocity variables. The full description of this method can be found in Ferziger and Perić (2002) and therefore is omitted here. However, a flow chart, representing SIMPLE, is presented in Fig. 3.4, which gives a general idea of SIMPLE. In this flow chart the process is described as follows:

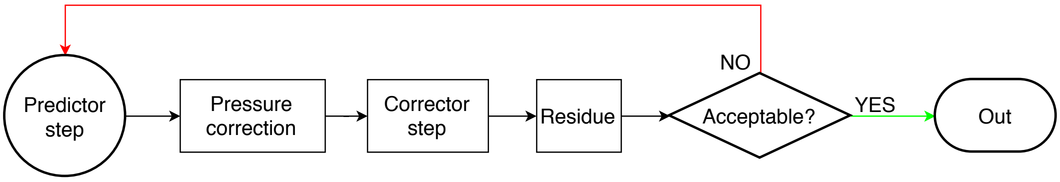

Figura 3.4 – Flow chart of the SIMPLE method.

- PREDICTOR STEP: this is the first process in the SIMPLE method, in which the momentum equation are solved using the values available (mass balance is not necessarily satisfied);
- PRESSURE CORRECTION: the linear system for the pressure correction is solved using the the values obtained from the predictor step;
- CORRECTOR STEP: the known pressure correction is used to correct the mass flow, the velocity components, and the pressure;
- RESIDUE: the residue is estimated using the corrected variables;
- ACCEPTABLE: a comparison of the calculated residue and a tolerance is made to decide if the numerical results are acceptable;
- OUT: if the results were acceptable the SIMPLE procedure is finished.

3.3.1.6 Momentum interpolation method

The code used in this work is based on collocated grid, that is all variables are evaluated in the volume centroid. Thus, a specific interpolation method must be used to obtain the velocities on the volume faces. For incompressible and one-phase flow, the momentum interpolation method developed by Rhie and Chow (1983) can ensure pressure-velocity coupling, preventing the appearance of the checkerboard pressure field. However, the VOF method implies surface tension force between phases and usually the time step is reduced when compared to that of the one-phase flow. Therefore, modification of the original momentum interpolation method was made, following the work of Denner (2013).

The velocity at the cell faces, u_{i_f}, is calculated according Eq. 3.49,

$$\begin{aligned}
&u_{i_f} = u^*_{i_f} \cdot n_{j_f} + CAP\left(p_R - p_L - \nabla p_f \cdot \vec{ds}\right) - \\
&\frac{2CAP\sigma}{\rho_g + \rho_l}\left(\rho^*_f \kappa^*_f \left(\alpha_R - \alpha_L\right) - \frac{2\left(\kappa_R \nabla \alpha_R + \kappa_L \nabla \alpha_L\right)}{\rho^*_f} \cdot \vec{ds}\right) + \qquad (3.49)\\
&\frac{V_L \rho_L^{n-1} + V_R \rho_R^{n-1}}{\Delta t\left(ap_L + ap_R\right)}\left(u_{i_f}^{n-1} - u_{i_f}^{*^{n-1}} \cdot n_{j_f}\right),
\end{aligned}$$

where: $u^*_{i_f}$ is a first approximation of the velocity on face, weighted by the coefficients ap_R and ap_L from the discretization; n_{j_f} is the unit vector normal to face analyzed; $CAP = -\left(\frac{1}{\vec{ds} \cdot n_{j_f}}\right)\left(\frac{V_L + V_R}{ap_L + ap_R}\right)$ is the contribution of the cell volumes over their coefficients ap_R and ap_L; ∇p_f is the gradient evaluated at the face between the two cells, weighted by the coefficients ap_R and ap_L; ρ^*_f and κ^*_f are the first approximations of, respectively, the density and the curvature at the face between the two cells; the subscripts R and L indicates the variables at, respectively, right cell and left cell, according Fig. 3.3; and $n-1$ indicates the variables are from the previous time step.

Concisely, the momentum interpolation method used in this work accounts for transient and surface tension force effects besides the common effects usually accounted in the original work of Rhie and Chow (1983).

3.3.2 Lagrangian referential

Numerical modeling for the discrete phase gathers the schemes used to integrate the differential equations for the particle motion, the interpolation of Eulerian variables at the particle position and the particle tracking method.

3.3.2.1 Integration scheme

In the present work, the ordinary differential equations for the particle motion were integrated using the analytical scheme (SALVO, 2013), so that the velocity and position of the discrete particle can be estimated according the Eq. 3.50 and Eq. 3.51, respectively,

$$u_{p_i}^{n+1} = u_i^n + e^{-\Delta t/\tau_p}\left(u_{p_i}^n - u_i^n\right) - a\tau_p\left(e^{-\Delta t/\tau_p} - 1\right), \tag{3.50}$$

$$x_{p_i}^{n+1} = x_{p_i}^n + u_i^n\Delta t + a\tau_p\Delta t + \left(u_{p_i}^n - u_i^n - a\tau_p\right)\tau_p\left(1 - e^{-\Delta t/\tau_p}\right), \tag{3.51}$$

where, the superscript n indicates the current time step; u_i is the fluid velocity at the particle position; $\tau_p = 1/F_d$ is the relaxation time; and $a = F_{w,b}/m_p$ is the weight-buoyancy force combination divided by the particle mass.

3.3.2.2 Interpolation at the particle position

Since the fluid velocity at the particle position is required in the calculation of the particles motion, the Shepard interpolation scheme is used (SALVO, 2013) to obtain the fluid velocity in the particle position, which is usually different of the position of the cell centroid. In this scheme, the velocity of the fluid at the particle position is interpolated considering the fluid velocity of the cell, where the particle is contained, and the other neighboring cells. The velocity at the particle position is calculated through a weighted average of the inverse of the distances between the centroid of each cell and the particle position. Figure 3.5 shows the distances between the particle position and the geometric center of each cell. The Eq. 3.52,

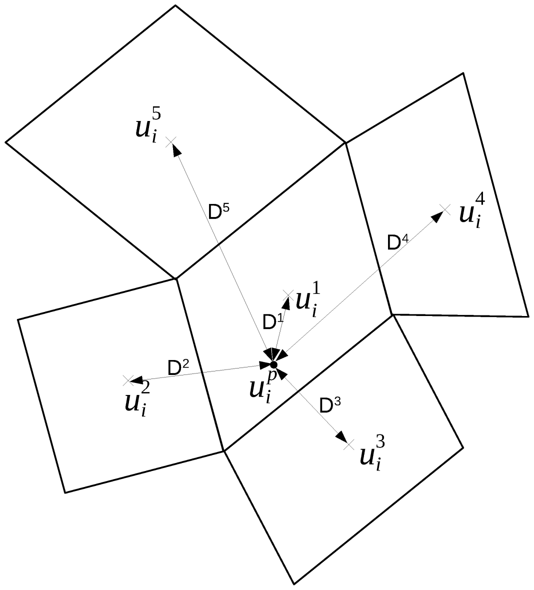

Figura 3.5 – Diagram of particle position and centroid of cells.

$$u_i^p = \frac{\sum\limits_{j=1}^{N} \left(u_i^j / D^j\right)}{\sum\limits_{j=1}^{N} \left(1/D^j\right)}, \tag{3.52}$$

expresses the Shepard interpolation scheme, where all variables is related to the Fig. 3.5 and N is the number of neighboring cells plus one (the cell in which the particle is contained).

3.3.2.3 Algorithm of particle tracking

The algorithm proposed by Haselbacher, Najjar and Ferry (2007) was used to track the particles position. The algorithm has proved to be efficient and robust for unstructured grid, since the algorithm is based on tracking a particle along its trajectory by computing the intersections of the trajectory and the cell faces. Initially, the position and velocity of the particles are known; the fluid flow is solved numerically and the new position and velocity of the particles are calculated using interpolations at the previous position. The new calculated position of the particle is compared to the face center of the finite volume, according Eq. 3.53,

$$(\overrightarrow{r_{f_c}} - \overrightarrow{r_p}) \cdot \vec{n} \geq 0, \tag{3.53}$$

where, $\overrightarrow{r_p}$ is the new position of the particle; $\overrightarrow{r_{f_c}}$ is the center of the finite volume faces and $\vec{n}$ is the unit normal face vector pointed out.

The details of the particle tracking developed by Haselbacher, Najjar and Ferry (2007) are not described here, however some features of this algorithm deserve to be highlighted:

- this algorithm is robust enough to allow a particle to crosses more than one computational cell in a single step and time, in other words, the algorithm enables the particle to go through long distances, which is a limiting factor for a number of algorithms;
- the algorithm is based on distances intersection rather than time intersection, which is much more natural, once the particle tracking problem should be primarily a spatial problem, not temporal;
- and the algorithm can be applied to Eulerian meshes consisting of polyhedral elements.

3.3.3 Numerical overview

In this subsection, an overview of the numerical modeling is presented to give a better understanding of the steps followed to solve LJIC using hybrid approach. Figure 3.6 presents the complete flow chart for the numerical modeling applied in the numerical simulation procedure. Initial and boundary conditions are established prior, and temporal advance is made by solving fluid flow. Primary breakup criterion is evaluated following to Lagrangian solution, in which secondary breakup is performed. Simulation is finished as soon as the residues and final time are reached.

3.3.4 Methodology

The methodology used in this work consists of the problems used for verification of VOF method implementation, the use of software for mesh generation, numerical simulation and post processing.

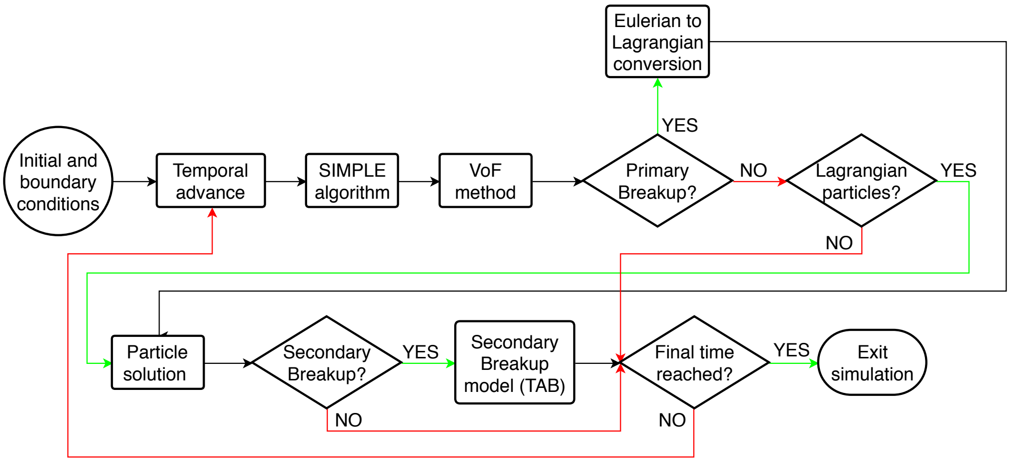

Figura 3.6 – Flow chart of the general overview of the numerical modeling applied in the numerical simulation procedure.

Two cases were chosen for verification of VOF method implementation: sphere deformation and stationary droplet. Both cases a common numerical tests used to verify two-phase methods. These verification tests following the work of Francois et al. (2006), Hernández et al. (2008), Maric, Marschall and Bothe (2013).

Mesh generation were made through ICEM-ANSYS. All finite volumes are of hexahedral elements. In all cases, the quality of the generated mesh was higher than 0.5. After mesh is generated a data conversion is made, so that geometric data from mesh can be read by UNSCYFL3D code.

Numerical simulations are performed in UNSCYFL3D code, where the numerical setup is defined previously. After simulation is finished, the results can be visualized in VisIT or ParaView software. Both software were used to analyze simulations.

In the following chapter numerical results for the LJIC is presented preceded by numerical verifications for the VOF method implementations in the unstructured grid code.

CHAPTER IV

RESULTS AND DISCUSSIONS

Part of the content of this chapter has been published in: Fontes, Duarte and de Souza (2018) and Fontes and de Souza (2017)

First, in this chapter the verification and validation processes of VOF method, implemented in an unstructured grid code, named UNSCYFL3D (developed at the Fluid Mechanics Laboratory from the Federal University of Uberlândia), version 2.4, is presented. In the following, the cases and numerical settings analyzed for the simulations of LJIC are described. Discussions of the numerical results using different methods are made properly, comparing these results with the experimental measurements of two LJIC cases.

4.1 Verification and validation of VOF method

During this dissertation the VOF method was implemented in the UNSCYFL3D code, which was already extensively validated for Lagrangian approach simulations (De Souza; De Vasconcelos Salvo; De Moro Martins, 2012; De Souza; SILVA; UTZIG, 2014; DUARTE; SOUZA; SANTOS, 2015; DUARTE et al., 2017). Thus, some verification and validation simulations related to the VOF method are presented, ensuring the implementation and robustness of the VOF method implemented in the unstructured grid code UNSCYFL3D. The verification test consists of evaluating whether the implementation is correct, comparing numerical solution to the exact solution of a manufactured problem. Validation process consists of simulating a physical problem and comparing the results to an analytical or experimental solution.

Three problems are presented for verification and validation of the VOF method: sphere deformation, which is a verification test; stationary drop with surface tension force and water droplet splash, both validation tests.

4.1.1 Sphere deformation

In the sphere deformation verification test, a water sphere with a radius of $0.15\ m$ is surrounded by air, confined in a cubic cavity with side length of $1.0\ m$. The center of the water sphere is located at the position $\vec{x}_c = (0.35, 0.35, 0.35)$, as depicted in Fig. 4.1. Water sphere is deformed through an imposed velocity field, dependent on position and time, Eq.

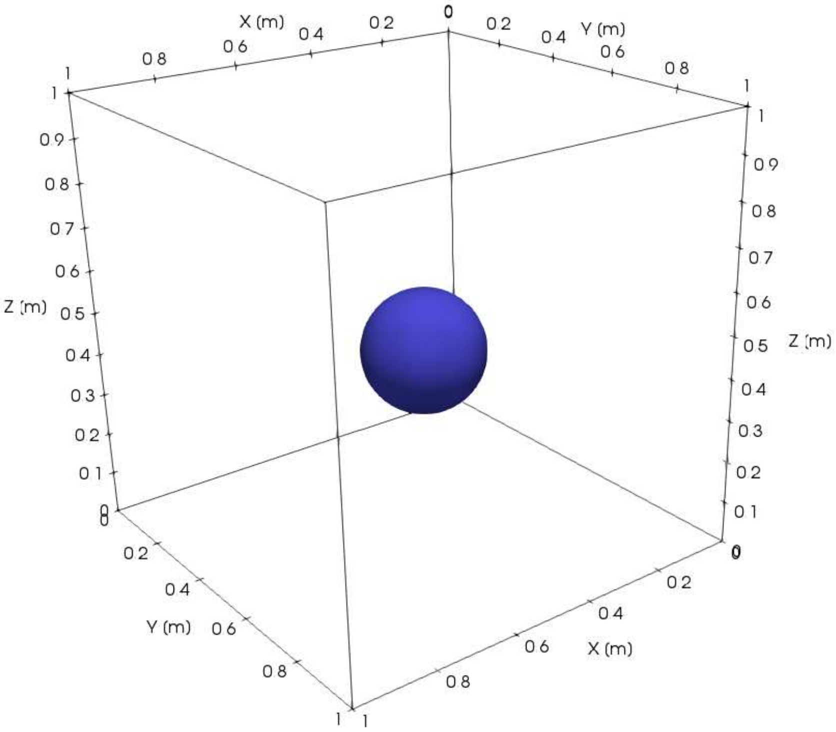

Figura 4.1 – Diagram of the initial position of the sphere submitted to deformation.

4.1,

$$
\begin{aligned}
u(x,y,z,t) &= 2sin^2(\pi x)sin(2\pi y)sin(2\pi z)cos\left(\frac{\pi}{3}t\right),\\
v(x,y,z,t) &= -sin(2\pi x)sin^2(\pi y)sin(2\pi z)cos\left(\frac{\pi}{3}t\right),\\
w(x,y,z,t) &= -sin(2\pi x)sin(2\pi y)sin^2(\pi z)cos\left(\frac{\pi}{3}t\right).
\end{aligned}
\tag{4.1}
$$

The imposed velocity field deforms the water drop until a maximum deformation and returns the water drop to its initial form and position. However, due to the limitations of the VOF method using algebraic schemes (CICSAM) for the advection term, the interface is expect to be not perfectly represented.

In this numerical verification, a grid mesh of 64^3 uniform and hexahedral finite volumes were used. Three time steps were evaluated: $\Delta t = 0.005\,s$, $\Delta t = 0.0025\,s$ and $\Delta t = 0.00125\,s$. Beside this, three algebraic schemes for the advection term of the VOF method were evaluated: CICSAM, HRIC and the modified HRIC.

Courant number is an important dimensionless number relating time step, grid size and velocity, defined as Eq. 4.2 for three dimensions,

$$
Co = \Delta t \sum_{i=1}^{3} \frac{u_{x_i}}{\Delta x_i}. \tag{4.2}
$$

The Courant number is a good parameter to guarantee numerical convergence, mainly in explicit solution. For VOF simulations, low Courant numbers are associated to a better interface representation, whereas high Courant number are associated to an worse interface representation. The Courant numbers, corresponding to $\Delta t = 0.005\,s$, $\Delta t = 0.0025\,s$ and $\Delta t = 0.00125\,s$ are, respectively: $Co = 0.64$, $Co = 0.32$ and $Co = 0.16$.

The droplet interface, represented by an iso-surface of $\alpha = 0.5$, at the position in the maximum droplet deformation (half temporal cycle) and at the position after one temporal cycle are shown in Fig. 4.2, for algebraic schemes implemented and $Co = 0.16$. The droplet interface was not perfectly represented, since part of the interface vanished/deformed in both stages presented in Fig. 4.2. HRIC and modified HRIC schemes present little differences on

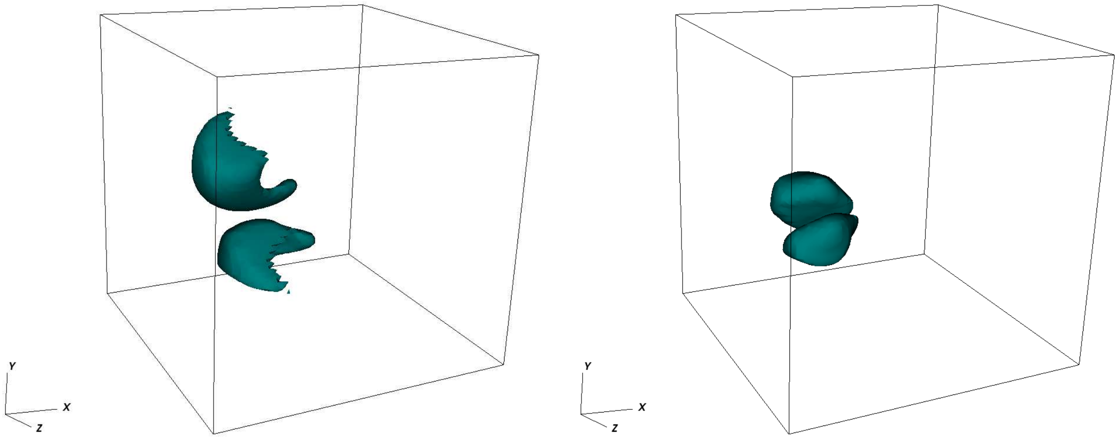

(a) Position in the maximum droplet deformation, using HRIC.

(b) Position after one temporal cycle, using HRIC.

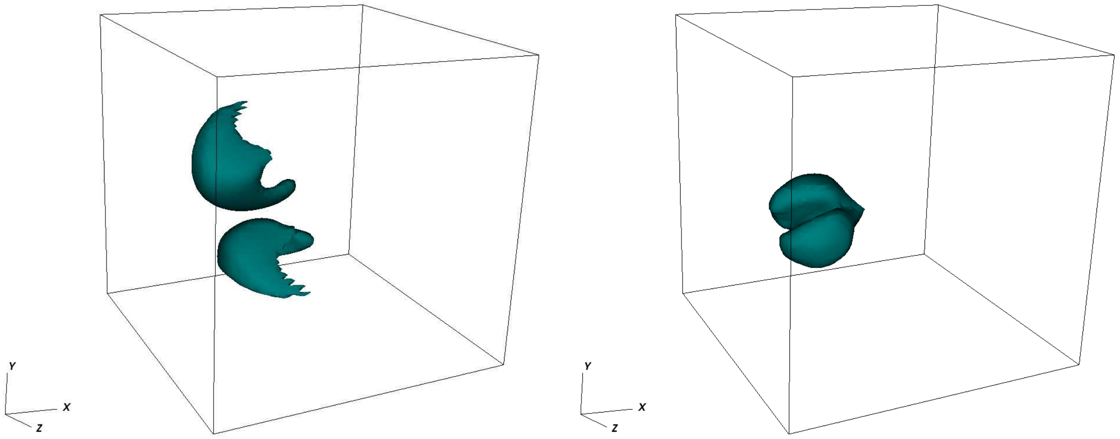

(c) Position in the maximum droplet deformation, using modified HRIC.

(d) Position after one temporal cycle, using modified HRIC.

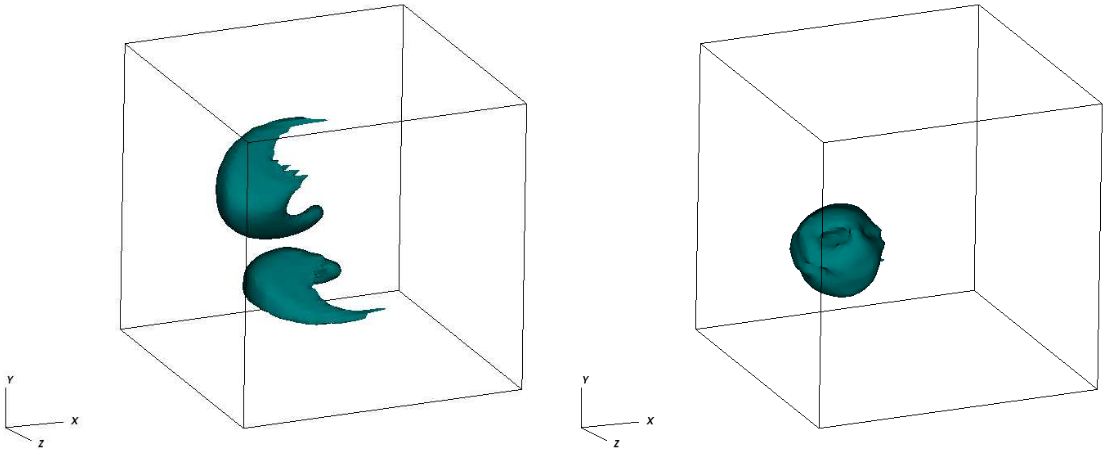

(e) Position in the maximum droplet deformation, using CICSAM.

(f) Position after one temporal cycle, using CICSAM.

Figura 4.2 – Temporal stages of the droplet deformation.

the droplet interface representation. However, CICSAM schemes shows a better representation of the droplet interface, keeping droplet form closer to spherical form for one temporal cycle than that of HRIC and modified HRIC schemes. Aiming to obtain quantitative comparisons between algebraic schemes and the Courant numbers, the deviations of the description of the droplet interface after one temporal cycle were calculated. Error calculus is made through the L_1-error norm as made by Hernández et al. (2008). The estimated errors were also compared to those obtained for other authors that used algebraic and geometric schemes for similar grid size, presented in Tab. 4.1.

Tabela 4.1 – Error of numerical simulation compared to the analytical solution for different algebraic schemes and Courant numbers.

Author	Co	Error
Present work, HRIC	0.16	1.009e-2
	0.32	1.029e-2
	0.64	1.499e-2
Present work, modified HRIC	0.16	7.014e-3
	0.32	8.288e-3
	0.64	3.502e-2
Present work, CICSAM	0.16	5.157e-3
	0.32	8.177e-3
	0.64	2.948e-2
Hernández et al. (2008), RK-3D	1.0	2.32e-3
	0.5	2.75e-3
Hernández et al. (2008), FMFPA-3D	1.0	2.62e-3
	0.5	2.79e-3
Xiao et al. (2015), UMTHINC/QHQ, algebraic scheme	0.25	2.76e-3
Maric, Marschall and Bothe (2013), geometric scheme	0.1	1.534e-3
	0.5	2.350e-3
	0.75	3.172e-3

The calculated errors for this verification test were very close to that obtained by other authors, ensuring the accuracy of the implemented VOF method. Other manufactured problems were evaluated, such as advection of a disk and advection of a square. However, due to the fact these problems are more straightforward than the sphere droplet deformation problem, they were omitted. Therefore, considering the verification of the sphere droplet deformation problem, the implementation of the VOF method is considered verified.

4.1.2 Surface tension in a stationary droplet

This verification problem consists of a sphere of one phase immersed in other phase. The surrounding phase is contained in a cubic domain of side $l = 8\,m$ and the radius of the sphere is $r_{sphere} = 2\,m$, as depicted in Fig. 4.3. The density ratios between phases is 10, where the sphere density is $\rho_{sphere} = 1\,kg/m^3$ and the density of the surrounding phase is $\rho_{surrounding} = 0.1\,kg/m^3$. No gravitational forces, neither viscous effects were considered in this problem, since the goal is to evaluate the pressure difference between the pressure inside the sphere and the pressure outside the sphere.

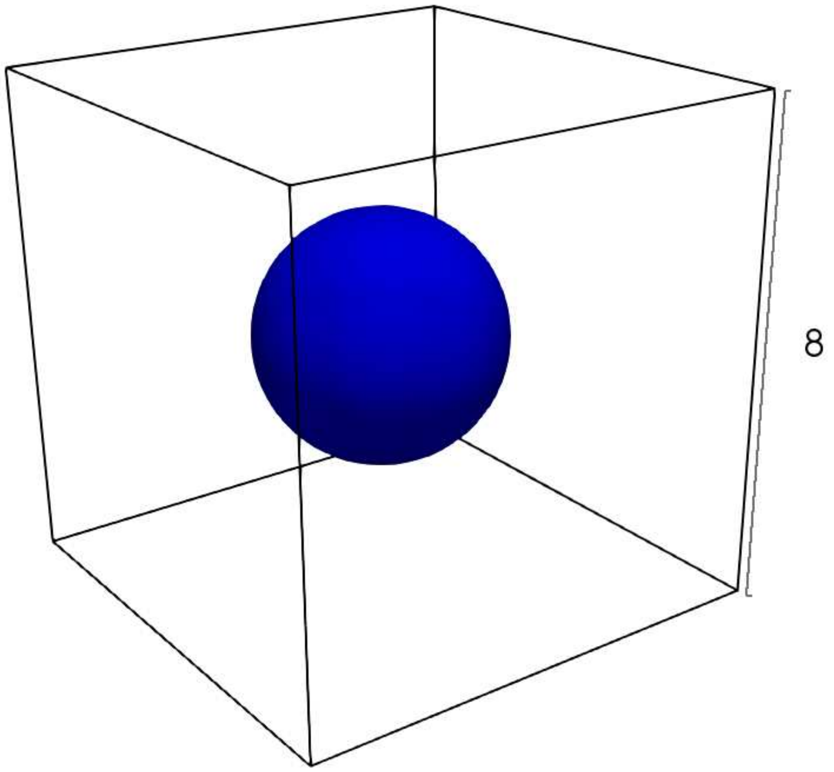

Figura 4.3 – Diagram of the denser sphere surrounded by less dense phase in a cubic domain.

An analytical solution of the pressure difference in this problem is obtained through the Young-Laplace equation (WHITE, 2003), Eq. 4.3,

$$\Delta p_{exact} = \sigma\kappa, \tag{4.3}$$

where $\sigma = 73\,Pa \cdot s$ is the surface tension coefficient of this problem; and $\kappa = 1\,m^{-1}$ is the curvature of the sphere of radius $r_{sphere} = 2\,m$. The surface tension force is net force keeping spherical form despite the pressure inside the sphere and the pressure outside are different.

The comparison of the numerical solution and analytical solution of this problem is shown in Tab. 4.2. The pressure difference calculated, Δp, was obtained considering the average pressure in two regions: first region consists on $r \leq r_{sphere}/2 = 1$; second region consists on $r \geq 3r_{sphere}/2 = 3$. This two regions were established to avoid the transition region, similarly as considered by Francois et al. (2006).

Tabela 4.2 – Comparison of the numerical solution and analytical solution for the problem of surface tension in a stationary inviscid droplet.

number of time step	$\Delta p_{numerical}$	$\Delta p_{analytical}$	$error = \dfrac{\Delta p_{numerical} - \Delta p_{analytical}}{\Delta p_{analytical}}$
1	71.70	73.0	1.78×10^{-2}
10	74.00	73.0	1.37×10^{-2}
50	78.29	73.0	7.25×10^{-2}

The error between numerical solution and analytical solution increases with time, due to the spurious velocities that arise in VOF stationary problems (FRANCOIS et al., 2006; DESHPANDE; ANUMOLU; TRUJILLO, 2012). Figure 4.4 shows the magnitude of spurious velocities for one time step and ten time steps. Clearly, the magnitude of spurious velocities increases quickly on time. High accuracy methods have showed reduced spurious velocity, near to zero. However, these spurious velocities are only relevant in stationary problems, such as

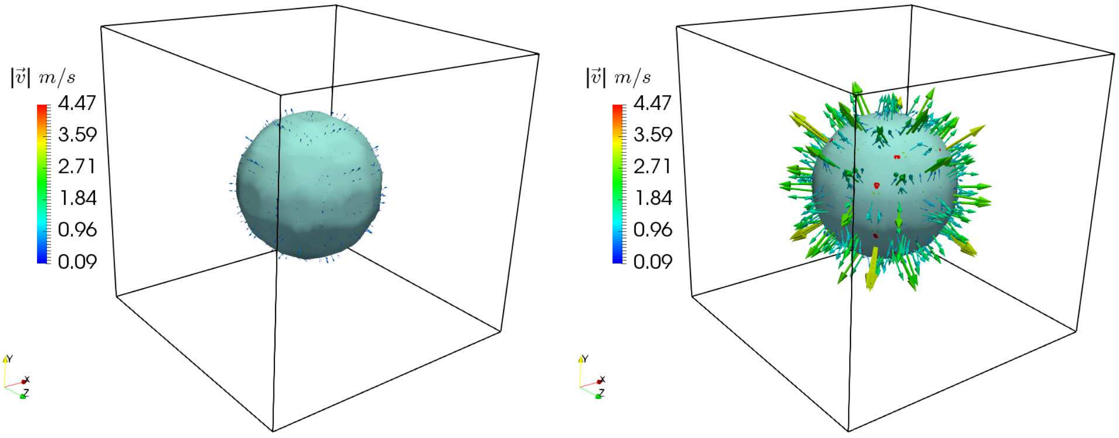

(a) $1\,\Delta t$.

(b) $10\,\Delta t$.

Figura 4.4 – Magnitude of spurious velocities.

the stationary inviscid droplet. In dynamic problems, spurious velocities are also reduced to zero. Therefore, the implemented VOF method and respective schemes are able to solve LJIC problems.

4.1.3 Water droplet splash

Water droplet splash consists of temporal evolution of a water droplet impacting on water pool. This impact creates a crater that reaches a maximum depth. The combination of surface tension and gravitational effects leads the gas-liquid interface to an hydrostatic condition. From crater formation to hydrostatic condition, the impact of the water drop on the pool can generate bubble entrainment, ascending liquid jet and other coherent structures. Consequently, temporal evolution of this problem is highly dependent on the surface tension, inertial effects and gravitational field. In dimensional analysis terms, these phenomena can be represented by two important dimensionless parameters, the Weber and Froude numbers. The former expresses the ratio between the inertial forces and the surface tension forces, while the latter is the ratio of the inertial forces on a element of fluid to the weight of the fluid element. Weber, We, and Froude, Fr, numbers are given by the following equations, Eq. 4.4 and Eq. 4.5,

$$We = \frac{\rho_l U_I^2 d_d}{\sigma}, \tag{4.4}$$

$$Fr = \frac{U_I^2}{g d_d}, \tag{4.5}$$

where: ρ_l is liquid density; σ is the interfacial tension between liquid and gas phases; U_I is the impact drop velocity; and d_d is drop diameter. Oguz and Prosperetti (1990) mapped the bubble entrainment zone using experimental data from Pumphrey and Crum (1988). These authors identified bubble entrainment for some physical conditions of the drop impact and related them to the Weber and Froude numbers. As a result, they concluded that the bubble entrainment is contained by two curves, as shown in Fig. 4.5, where lines are the least-square fit of the experimental data of Pumphrey and Crum (1988) with the form of $We = AFr^B$.

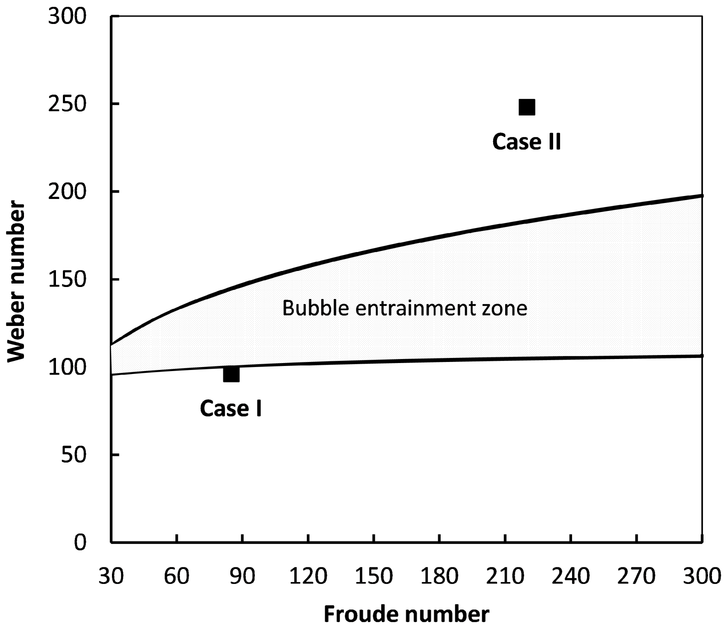

Figura 4.5 – Map showing the bubble entrainment zone for different conditions based on the Weber and Froude numbers, adapted from (OGUZ; PROSPERETTI, 1990).

The upper line gives $A = 48.3$ and $B = 0.247$, while the lower line $A = 41.3$ and $B = 0.179$.

The two cases indicated in the Fig. 4.5 were numerically studied and compared with the experimental work of Morton, Rudman and Liow (2000) for the same Froude and Weber numbers. The complete geometry for the two cases consists of a cubic domain containing water and air in a quiescent condition. This condition is disturbed by the impact of a water drop onto the water pool. In Fig 4.6 initial condition for the splash cases is presented. Because of the symmetry of the problem, only a quarter of the domain was considered to reduce the computational cost. Furthermore, the water drop was released at the imminence to impact the water pool. The impact velocity was set to reproduce the one measured experimentally, and to consequently match the experimental Froude and Weber numbers. No-slip conditions were prescribed at the walls. All the dimensions of the Fig. 4.6 are scaled using the water drop diameter ($d_d = 2.9\,mm$). In Fig. 4.6, h_c is the height of the cavity, h_w is the height of the water pool, w_c is the width of the cavity (remembering that w_c is the half of the width of the complete domain) and r_d is the water drop radius. In Tab. 4.3 the dimensions for the two cases studied in this work are shown.

The results shown here were obtained using the CICSAM scheme with explicit solution of

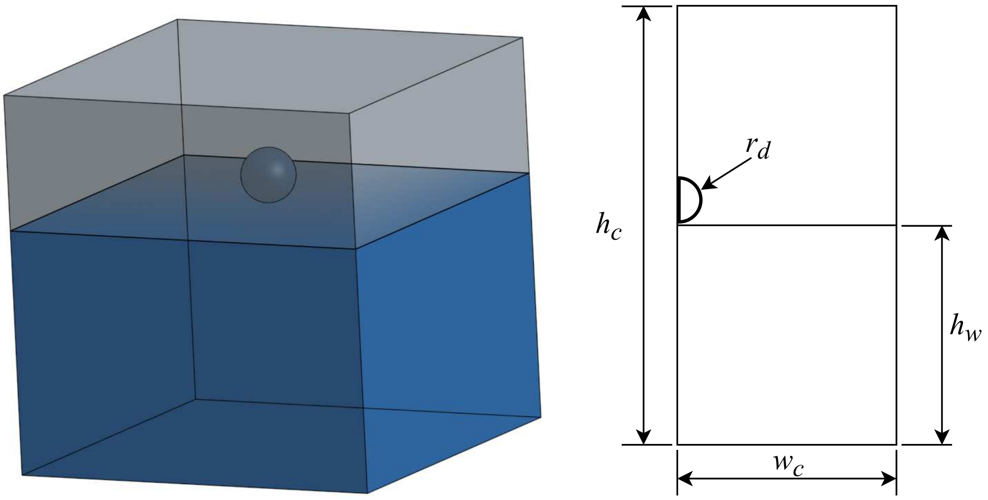

(a) Complete model. (b) A quarter of the domain.

Figura 4.6 – Schematic of the droplet in the imminence of impacting the water pool.

Tabela 4.3 – Scaled dimensions of the splash cases.

$dimensions$	$dimensions/d_d$	
	$case\,I$	$case\,II$
h_c	7	9
h_w	4.5	4.5
w_c	3.5	3.5

the VOF equations. The computational mesh was uniform, using nearly two million hexahedral elements. The time step was $\Delta t = 10^{-5}\,s$ ($Co \approx 0.2$). The CPU time taken to solve the cases with this setup was approximately five days to reach about $0.03\,s$ in physical time, using a serial simulation with an intel® i7-4790k processor with 8GB of RAM memory.

The numerical results of the temporal development of the water droplet splash were analyzed and compared with the experimental results (MORTON; RUDMAN; LIOW, 2000), for case I and case II (Tab. 4.3).

In the real case, when the water drop is at the imminence to impact the water pool, it is expected that the downstream air pushes the free water surface. Sprittles (2017), using kinetic theory in the gas film via Boltzmann equation, showed the gas only influences the liquid phase through the pressure term in the normal direction of the interface, since usually $\mu_g/\mu_l << 1$, the tangential interaction is negligible.

In the numerical strategy, the water drop was released slightly above the water free surface, with a little gap ($\approx 0.2\,mm$) . However, this gap was found to be enough to capture the effect of the air pushing the free surface of the water pool, as shown in Fig. 4.7. In this figure an iso-volume of $\alpha = 0.5$ was used for the case I.

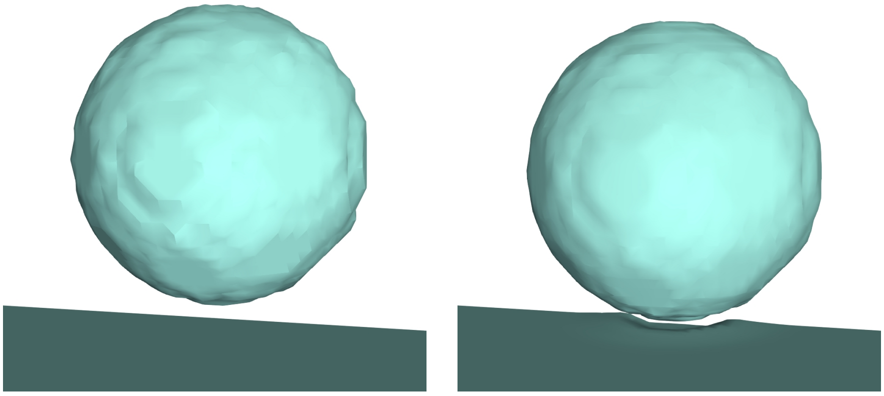

(a) First time step.

(b) Second time step.

Figura 4.7 – The effect of the air pushing the free surface of the water pool.

Temporal development of the water drop splash is an important qualitative result. The temporal evolution of the iso-volume of $\alpha = 0.5$, which was used to represent the interface, was compared to the experimental images of the temporal evolution of the water drop splash from Morton, Rudman and Liow (2000), Fig. 4.8 and Fig. 4.9. The comparison of the temporal evolution was made considering the same dimensionless time, represented by the t and τ variables, respectively for the experimental and numerical data. The dimensionless time of each case was obtained multiplying the time by the ratio of the corresponding drop impact velocity and the drop diameter (U_I/d_d).

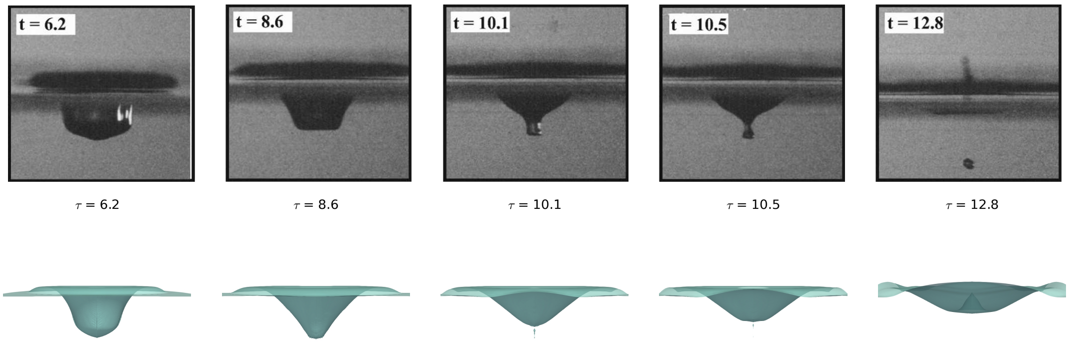

Figura 4.8 – Qualitative comparisons of the numerical splash topologies with images from Morton, Rudman and Liow (2000) for the case I.

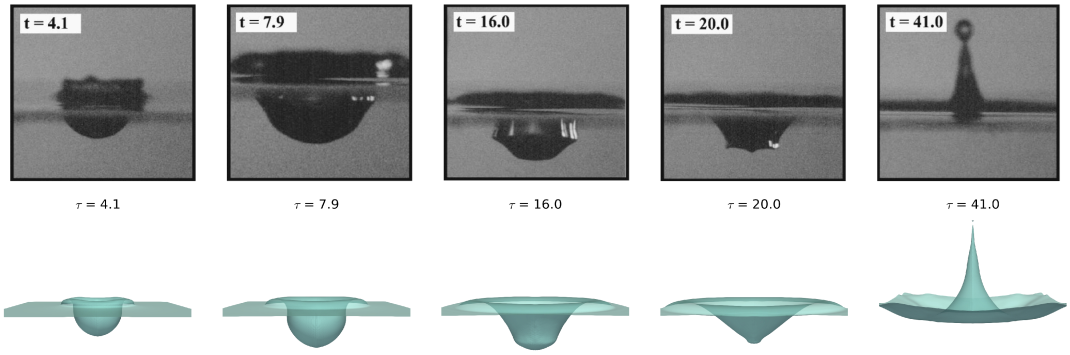

Figura 4.9 – Qualitative comparisons of the numerical splash topologies with images from Morton, Rudman and Liow (2000) for the case II.

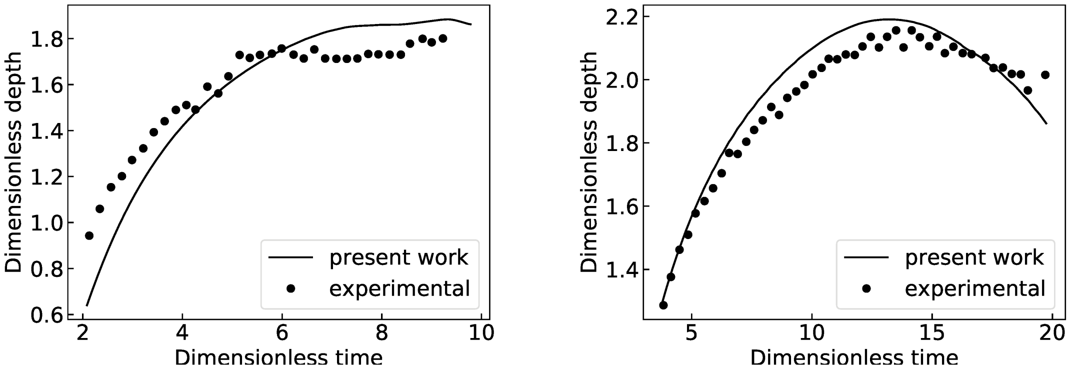

(a) case I.

(b) case II.

Figura 4.10 – Quantitative comparison of the numerical results for the depth crater with the experimental data of Morton, Rudman and Liow (2000).

The quantitative comparison between numerical results and the experimental data are depicted in Fig. 4.10. In this figure, one can see the dimensionless crater depth was solved suitably relating the experimental data work (MORTON; RUDMAN; LIOW, 2000) for different Froude and Weber numbers. More details about the water droplet splash and other analysis are found in Fontes, Duarte and de Souza (2018).

The verification and validation of the performed tests show that the VOF method implementation is suitable to solve liquid jet in crossflow (LJIC) problems.

4.2 Numerical results for LJIC

In this section the numerical results, using hybrid approach, of the two cases of LJIC are discussed. The physical features and the computational settings for the cases are described in details bellow.

4.2.1 LJIC cases and numerical settings

The two LJIC cases studied in this work are the same two cases numerically studied by Arienti and Soteriou (2007), which used hybrid approach to solve the spray formation on liquid jet in air crossflow. These two cases were evaluated experimentally by Deepe (2006). In addition to the hybrid approach strategy, further analyzes, not performed together in the literature yet, were considered in this present work:

- column breakup model;
- modified TAB model, accounting viscous flow inside the liquid droplet and droplet distortion;
- coalescence and grazing collision;
- and two-way interaction;

The computational domain is similar to the experimental test section of Deepe (2006). Figures 4.11 and 4.12 depict, respectively, the experimental test section (DEEPE, 2006) and the computational domain used in this work, where the dimensions of the domain are also shown.

In the two cases, the liquid phase is water, and the gas phase is air, whose physical properties considered are shown in Tab. 4.4. The flow conditions for the two cases, termed as $C1$ and $C2$, such as inlet velocity and dimensionless numbers are shown in Tab. 4.5. Due to the characteristics of the liquid jet entrance, such as short tube length and a tapered

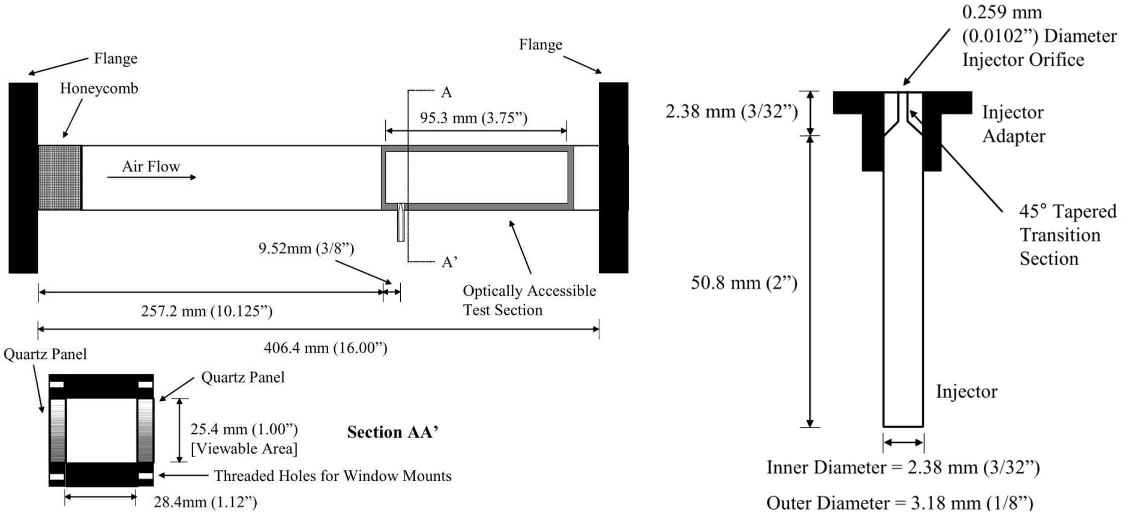

(a) experimental test section (DEEPE, 2006). (b) details of the injection of liquid (DEEPE, 2006).

Figura 4.11 – Dimensions of the experimental domain for the two cases of LJIC.

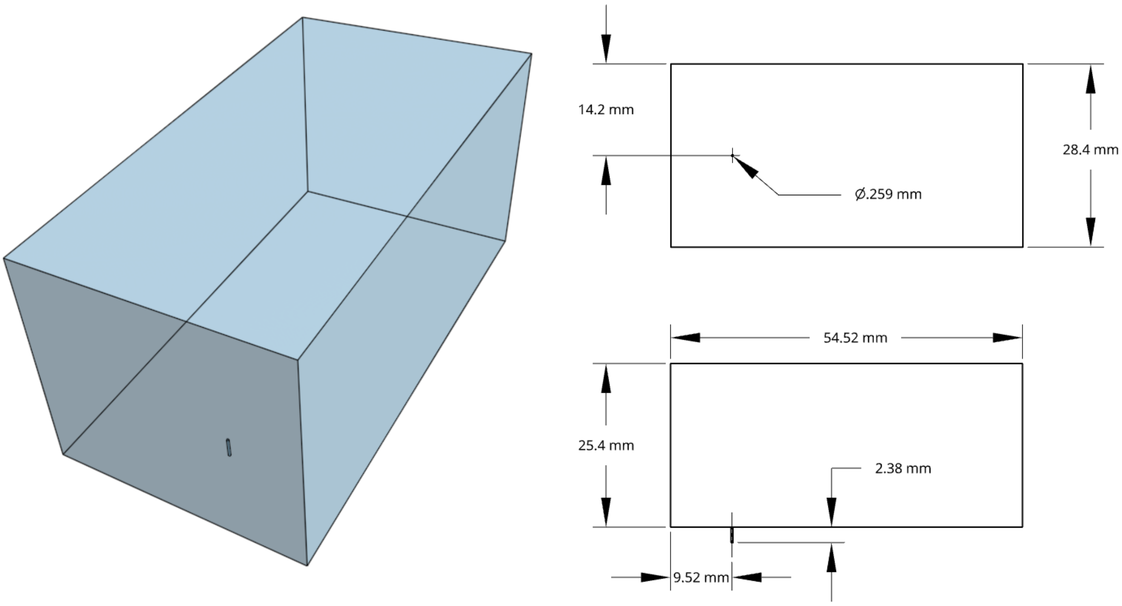

(a) isometric view of the physical domain. (b) dimensions of the physical domain.

Figura 4.12 – Physical domain for the two cases of LJIC.

Tabela 4.4 – Physical properties of the fluids studied.

Property	Air	Water
ρ $[kg/m^3]$	1.207	998.2
μ $[Pa \cdot s]$	1.7894×10^{-5}	1.003×10^{-3}
σ $[N/m]$	0.0713	

Tabela 4.5 – Flow conditions for the two studied cases.

Cases	$v_j[m/s]$	$v_g[m/s]$	$We_l[-]$	$We_g[-]$	$Re_l[-]$	$Re_g[-]$	$J[-]$
$C1$	4.26	50	15	11	1098	85665	6
$C2$	13.3	110	48	53	3428	188463	12

transition section, the liquid jet flows in both cases are considered laminar, even for $C2$, whose $Re > 2300$. Thus, two height column breakup are evaluated considering laminar flow for the liquid jet. Height column breakup is obtained through the column breakup coefficients, previously presented in section 2.2, from Wu, Kirkendall and Fuller (1997) and Sallam, Aalburg and Faeth (2003), respectively $C_b = 3.44$ and $C_b = 2.6$.

The different Weber numbers from the two cases indicate surface breakup regime is more likely to occur in $C2$ than in $C1$, since the ratio of the aerodynamic forces and the surface tension forces is higher in $C2$ than in $C1$. According to the physical conditions depicted in Tab. 4.5 and Fig. 4.13 (WU; KIRKENDALL; FULLER, 1997), $C1$ corresponds to column breakup regime, with primary breakup on bag breakup mode, whereas $C2$ is a multi-mode primary breakup, close to the surface breakup regime.

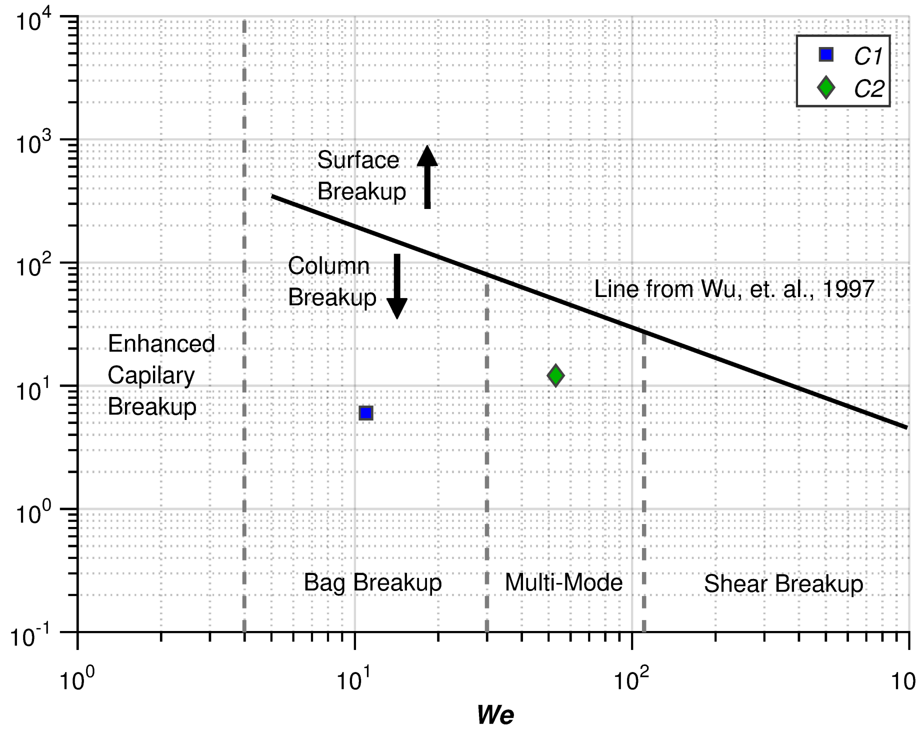

Figura 4.13 – Map of momentum flux ratio versus Weber number for the primary breakup of the LJIC.

Briefly, the numerical settings for the simulations of the studied cases are shown in Tab. 4.6, where one can see that eight simulations for each case are expected.

Tabela 4.6 – Numerical settings for the two studied cases.

Analyze	$C1$	$C2$
C_b	2.6	3.44
	3.44	2.6
Secondary Breakup	TAB	AB-TAB
	AB-TAB	TAB
Coupling	one-way	two-way
	two-way	one-way

In the following sections the results of LJIC simulations using the hybrid approach are discussed in details, addressing the following issues: adopted strategy for domain reduction; general LJIC flow characteristics; influences of different primary breakup coefficients and secondary breakup model over the velocity and mass occurrence of droplets; and two-way coupling and droplet collision effects. In previous sections the following modelings were described properly: two coefficients for the column breakup height from Wu, Kirkendall and Fuller (1997) and Sallam, Aalburg and Faeth (2003), respectively $C_b = 3.44$ and $C_b = 2.6$; the original TAB (O'ROURKE; AMSDEN, 1987); and AB-TAB (DAHMS; OEFELEIN, 2016) models and two-way coupling with droplet collisions.

4.2.2 Strategy for domain reduction

LJIC simulations usually require mesh resolutions of millions of elements to properly represent the liquid jet interface, so a strategy to relax such requirement is always useful. In this work, a symmetry assumption along the longitudinal tunnel plane, $x{-}plane$, was evaluated based on $C1$, Tab. 4.5. Figure 4.14 shows the general view and the mesh refinement on the $x - plane$ for two analyzed domains: half domain and full domain. In mesh creation, a box region including liquid column jet were refined aiming to capture properly liquid-gas interface and primary breakup. This box region is about $(2 \times 13 \times 13)d_j$, respectively for x, y and z axes. This region covers the range of column breakup height for both cases using the two analyzed column breakup height coefficients.

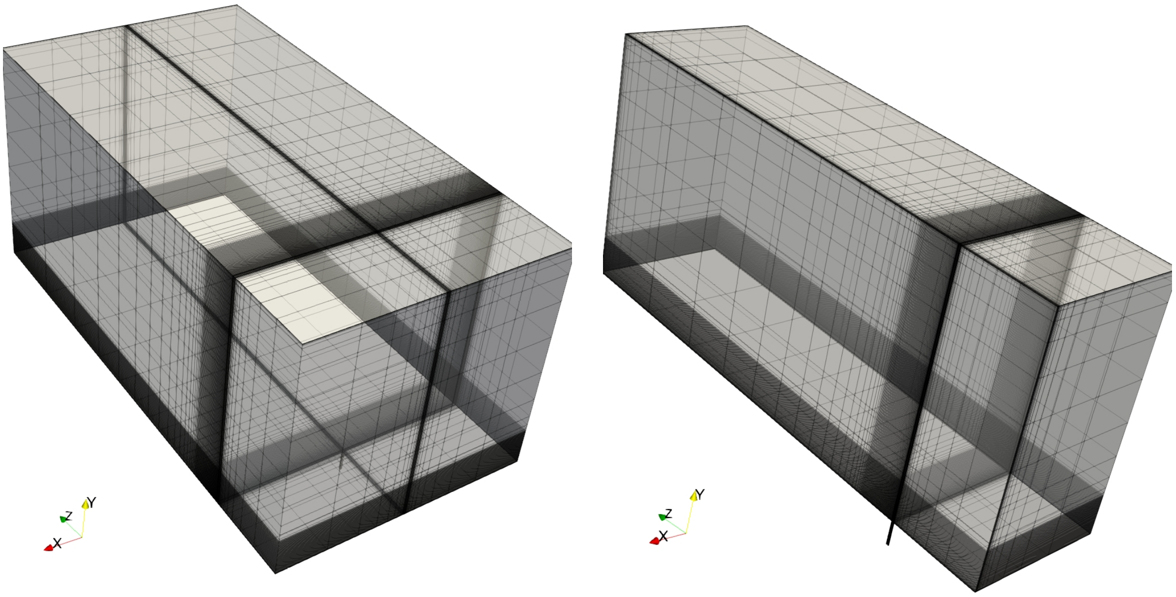

(a) full domain. (b) half domain.

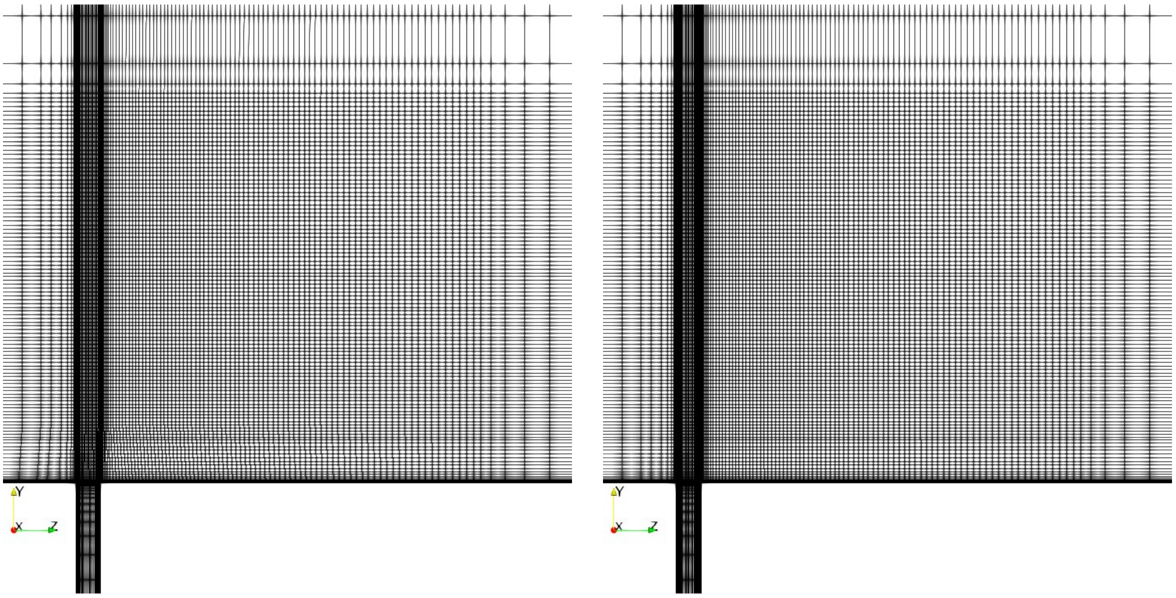

(c) full domain. (d) half domain.

Figura 4.14 – Grid and refinement zone near jet.

The use of a symmetric plane reduces the number of elements approximately by half. Meshes resolution of ≈ 640000 elements for a full domain and of ≈ 311000 elements for a half domain were enough to describe $C1$ adequately, based on the numerical representation of liquid jet topology and mass fraction distribution results. In both domains, the smallest elements have characteristic length of about $0.03\,mm$.

Figure 4.15 shows the similarity between the numerical results of full and half domains for the volume fraction in the symmetric plane $x-plane$. The volume fraction, α, is insensitive to the domain reduction, mainly because this is a RANS simulation. However, if LES simulations was used instead of RANS simulations, the liquid column of the jet would be time oscillating and the symmetry strategy would be inappropriate. The normalized mass fraction and the droplet velocity were obtained at $z-plane$ located at $3.81\,cm$ from the liquid jet exit for

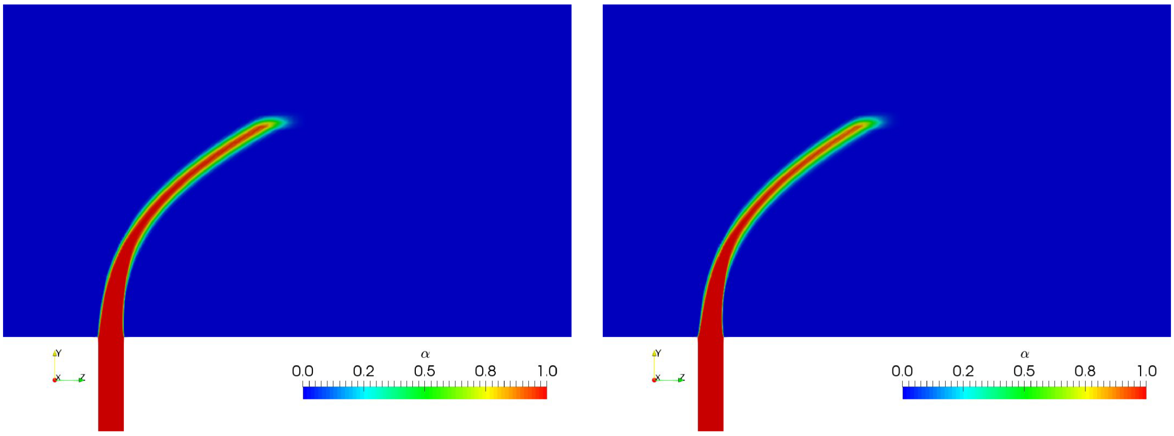

(a) full domain.

(b) half domain.

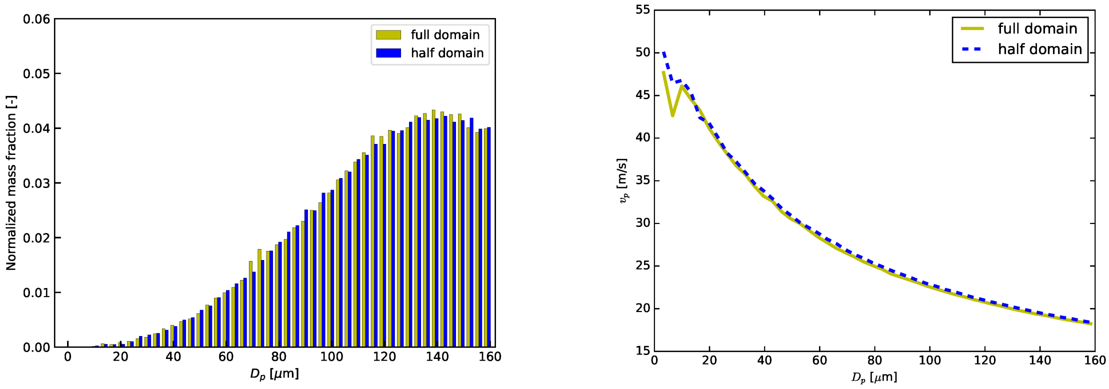

(c) mass fraction distribution.

(d) droplet velocity.

Figura 4.15 – Comparison of volume fraction field at $x-plane$ and mass fraction distribution and velocity at $z-plane$ for both analyzed domains.

both domains. Clearly, normalized mass fraction and velocity are rather insensitive to the assumption of symmetric flow, as expected for RANS simulations. Therefore, the strategy for domain reduction considering symmetric flow is reasonable and will be used throughout this work.

Following the assessed strategy for domain reduction, a mesh with about 2 million elements was made based on the half domain. This resolution produced grid-converged solutions for $C2$, which has higher Weber and momentum ratio numbers, considering liquid jet topology and mass fraction distribution. All numerical results for the two cases were obtained using this mesh.

4.2.3 LJIC characteristics using hybrid approach

In the hybrid approach, the interaction between air crossflow and liquid jet is solved through the VOF method, while droplets transport in airflow is solved as discrete particles.

Since the general features of the two-phase flow using hybrid approach are quite similar for different methods evaluated in this work, the flow characteristics for $C1$ and $C2$, Tab. 4.5, are shown for primary breakup coefficient $C_b = 3.44$, the original TAB method for secondary breakup and one-way coupling, unless otherwise stated.

Figure 4.16 shows a front view of the spray formation for $C1$ and $C2$ with $C_b = 2.6$, emphasizing the pressure augmentation on the liquid column jet. Biggest drops are created at the top of the liquid column jet being broken into smaller droplets along the air crossflow. The spray is laterally wider for $C1$ than for $C2$ because air velocity is higher in this case, which leads to higher secondary breakup frequency. Liquid column jet is curved into the air crossflow direction due to the increase of pressure on the front surface of liquid column jet. This increase of pressure on liquid column jet causes a flattening of the liquid column, so that circumferential profile of the liquid column jet is changed along the jet height.

In Fig. 4.17, the profiles of liquid column jet changes as its height increases. The shape of the profiles are dependent on the Weber number, which in this work varies with the air

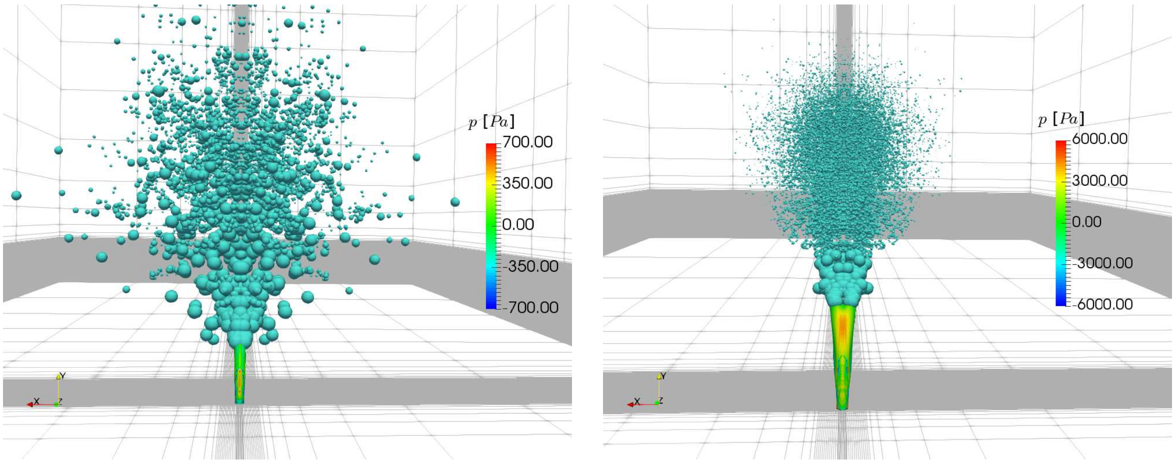

(a) $C1$ (b) $C2$

Figura 4.16 – Pressure on liquid column jet and spray formation.

velocity. Profiles more deformed are obtained in $C2$, since Weber number is higher in this case. The concavity formed at downstream side of the liquid column jet was obtained by Behzad, Ashgriz and Karney (2016), which studied numerically surface breakup on liquid jet in crossflow through high fidelity simulation. Experimentally the concave shape at downstream side of the liquid column jet was visualized and described by Oda et al. (1994). In both works in the upstream side of the liquid column jet, convex form is preserved. However, for $C2$ the Weber and momentum ratio are higher so that a kind of bifurcation may occur, which produces a concave shape of the interface profiles for higher dimensionless heights ($y/d_j = 8$).

Liquid jet in air crossflow changes significantly the gas velocity field, Fig. 4.18, creating a downstream recirculation, while the liquid jet is curved by the flow towards its main direction, as previously mentioned. Due to the liquid column barrier, the maximum air velocity in longitudinal direction is increased to maintain mass conservation.

Figure 4.19 shows the streamlines of air interacting with liquid jet. They are colored by the perpendicular component, y, of gas vorticity and the liquid jet column is represented by the isocontour $\alpha = 0.5$. Recirculating structures presented in $C2$ are more complex than those in $C1$ because the air velocity and liquid column height are higher in $C2$ than those in $C1$. In both cases these structure affect the droplet secondary breakup, since the drops released from the top of jet column may be carried to this recirculation region, changing drop Weber

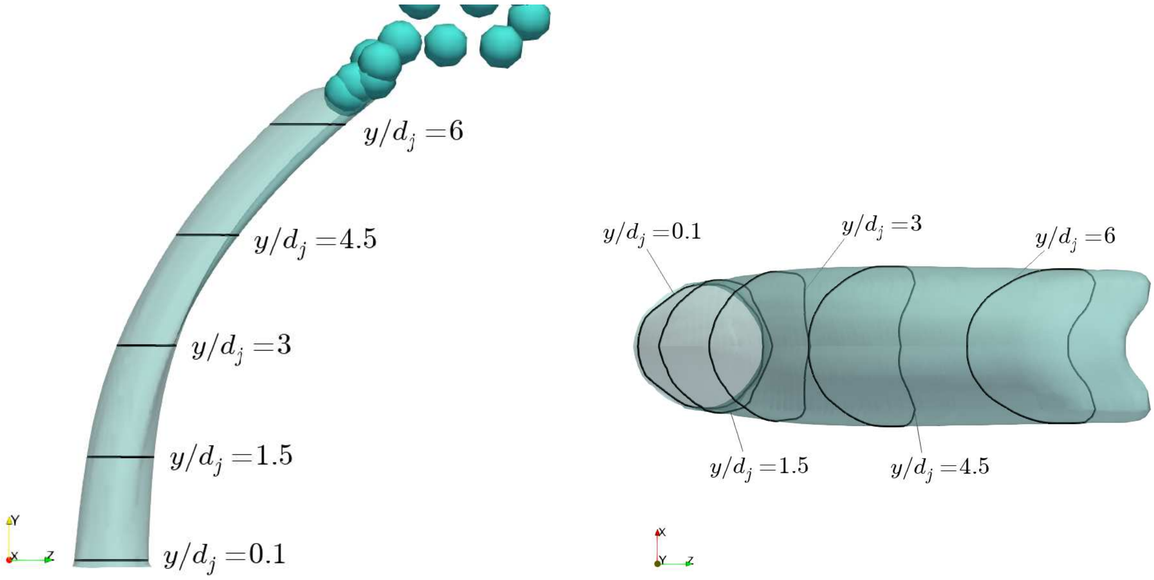

(a) Dimensionless height - $C1$ (b) Profiles - $C1$

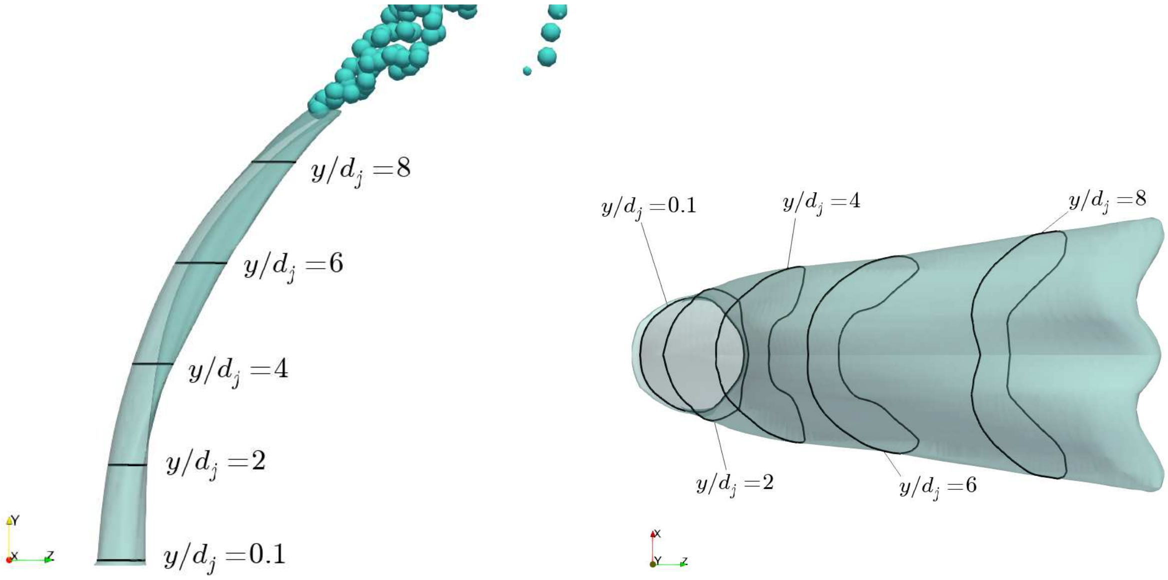

(c) Dimensionless height - $C2$ (d) Profiles - $C2$

Figura 4.17 – Profiles of liquid column jet.

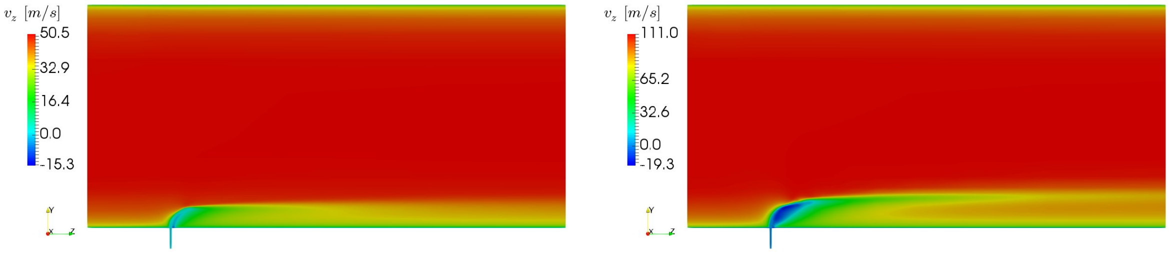

(a) $C1$ (b) $C2$

Figura 4.18 – Streamwise velocity component.

number that is used to calculate the criterion for secondary breakup. It is worth mentioning

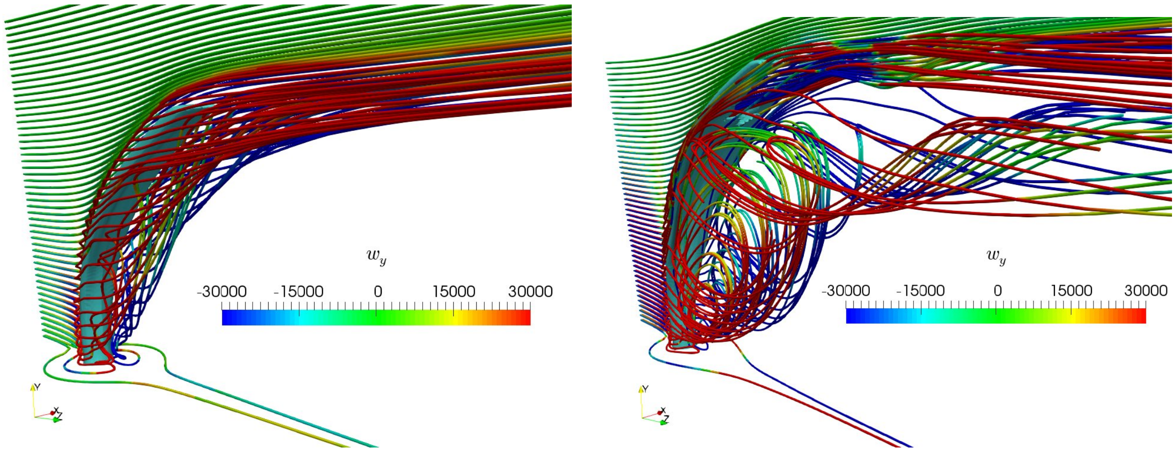

(a) $C1$ (b) $C2$

Figura 4.19 – Streamlines of air flow around the liquid jet.

that counter-rotating vortex, clearly identified in both cases, cannot be represented numerically by Euler-Lagrange approach, since liquid column jet is usually represented by blobs.

Primary breakup represents the conversion from Eulerian approach (VOF method) to Lagrangian approach (particle tracking). Figure 4.20 shows the general view of the primary and secondary breakups. The drops created at the top of the liquid jet have large diameter and low velocity; these drops are broken into other droplets due to the prevalence of aerodynamics forces over surface tension forces on their surfaces; the smallest droplets, in turn, are accelerated by the air flow, reaching equilibrium with the air velocity faster than the largest drops. In both cases the occurrence of droplets near walls is very low, so that the absent of liquid film on wall can be inferred. Regarding the differences between the two cases, in $C1$ droplets are more scattered in the domain than those in $C2$. This fact is related to the difference between the air velocity in both cases. As expected, in the case with higher air velocity ($C2$) the droplets directions align faster than in the case with lower air velocity ($C1$). Also, due to the air velocity differences in the cases, aerodynamic forces are higher in $C2$ than in $C1$ causing smaller droplet diameters in $C2$ than in $C1$.

More droplets are generated by secondary breakup in $C2$ than in $C1$. Due to the fact of the air velocity in $C2$ is higher than in $C1$, the shear stress on droplets surfaces is likewise higher, surpassing the surface tension forces more times than in $C1$. From a numerical point

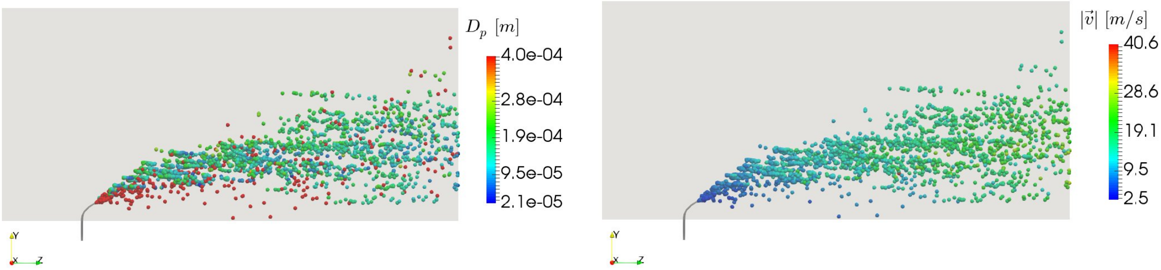

(a) $C1$: droplets colored by diameter.

(b) $C1$: droplets colored by velocity.

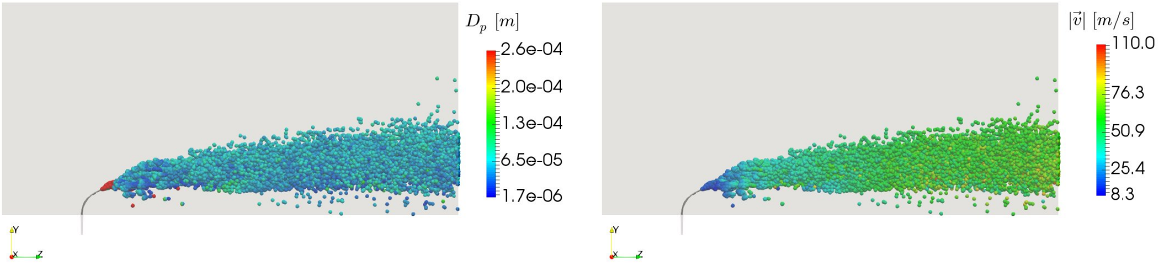

(c) $C2$: droplets colored by diameter.

(d) $C2$: droplets colored by velocity.

Figura 4.20 – General view of the first and secondary breakups.

of view, the critical Weber number is achieved more frequently in $C2$ than in $C1$, enhancing the secondary breakup.

In both cases, the droplet velocity increases as the droplets move away from the liquid jet nozzle. Thus, the fastest droplets are located close to the tunnel outlet. The small droplets quickly achieve equilibrium with the air velocity. This can be verified at the end of tunnel in $C1$, by comparing the droplet velocity and the respective diameter in Fig. 4.20(a) and Fig. 4.20(b).

According to the operating conditions depicted in Table 4.5 and Figure 4.13, $C1$ and $C2$ are classified as column breakup regime. Therefore, in both cases primary breakup can be modeled considering only column breakup, without breakup along the lateral surface of the jet column, known as surface/shear breakup. Therefore, there is no droplet creation on the column surface of the liquid jet.

The main advantage of the hybrid approach over the conventional Euler-Lagrange approach is highlighted by properly solving the interactions of the air flow and the liquid jet: the continuous flow field is accurately solved, which is crucial for mass fraction distribution and droplet velocity prediction. Although the Euler-Euler approach is capable of predicting the two-phase interactions accurately, extremely high CPU times are necessary, even using adaptive mesh refinement, to solve liquid-gas flows (SHINJO; UMEMURA, 2011; CHEN et al., 2013; BRAVO et al., 2015; LI; SOTERIOU, 2016). The hybrid approach poses as an excellent option to solve spray formation in LJIC with low CPU time. In this work, the most LJIC simulations took about ten days using a serial Intel® i7-4790k processor with $8\,GB$ of RAM.

4.2.4 Evaluation of primary breakup coefficients and secondary breakup models

In this section, the effects of different coefficients for the column primary breakup model and different secondary breakup models are compared numerically. Mass fraction distribution and droplet velocity at a specific measurement plane are a crucial to compare differences between methods and empirical coefficients. Also, these measurements are good criteria to determine the best numerical methodology to solve spray formation in LJIC. The following combinations are tested for both $C1$ and $C2$: two column breakup coefficients for primary breakup, $C_b = 2.6$ (SALLAM; AALBURG; FAETH, 2003) and $C_b = 3.44$ (WU; KIRKENDALL; FULLER, 1997); and two secondary breakup models, TAB (O'ROURKE; AMSDEN, 1987) and AB-TAB (DAHMS; OEFELEIN, 2016).

According to the experiment carried out by Deepe (2006), a transverse sampling plane, located at $3.81\,cm$ downstream the liquid jet nozzle, is defined to obtain mass fraction distribution and droplet velocity, as depicted in Fig. 4.21.

Normalized mass fraction distribution on the sampling plane was obtained by the following procedure: droplets diameters were divided into bins of range $3\,\mu m$; the mass of droplet whose diameter matched a specific bin was accumulated; and the final result was normalized by the total mass. The droplet velocity was temporally averaged for each droplet diameter, and achieved a statistically steady state.

Differences on experimental and numerical mass fraction results were evaluated using

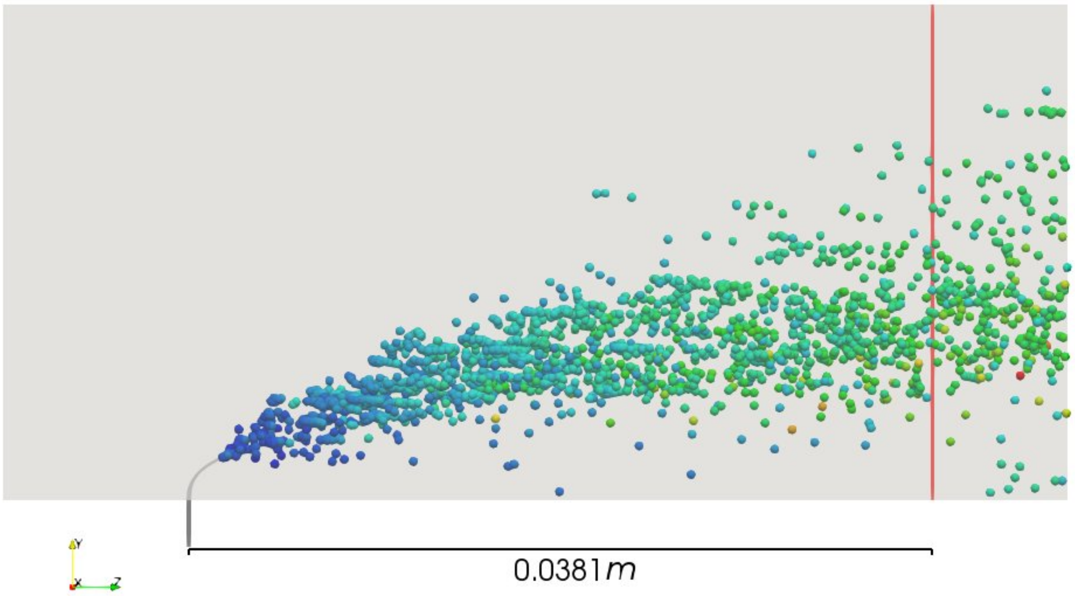

Figura 4.21 – Sampling plane at $3.81\ cm$, red line.

$l2-norm$, Eq. 4.6,

$$l2=\sqrt{\sum\left(m_{num}^{*}-m_{\exp}^{*}\right)^{2}}, \tag{4.6}$$

where m^* is the normalized mass fraction.

In the following sections are presented the results of the numerical simulations for each case, evidencing the best primary and secondary breakup modeling for LJIC through analyses of mass fraction distribution, droplet velocity and other numerical results. Mass fraction distribution and droplet velocity are the most challenging outcomes to obtain by numerical simulations. Therefore, these analyses were chosen as the main criteria to identify the most suitable numerical methodology to solve spray formation in LJIC, considering low computational costs.

4.2.4.1 General results for mean diameter distribution

General views of SMD (Sauter Mean Diameter), which is equal to the mean droplet diameter since droplets are spherical, are shown in Fig. 4.22 for $C1$ with different primary breakup coefficients and secondary breakup models. Three planes, located at $z/d_j \approx 174$,

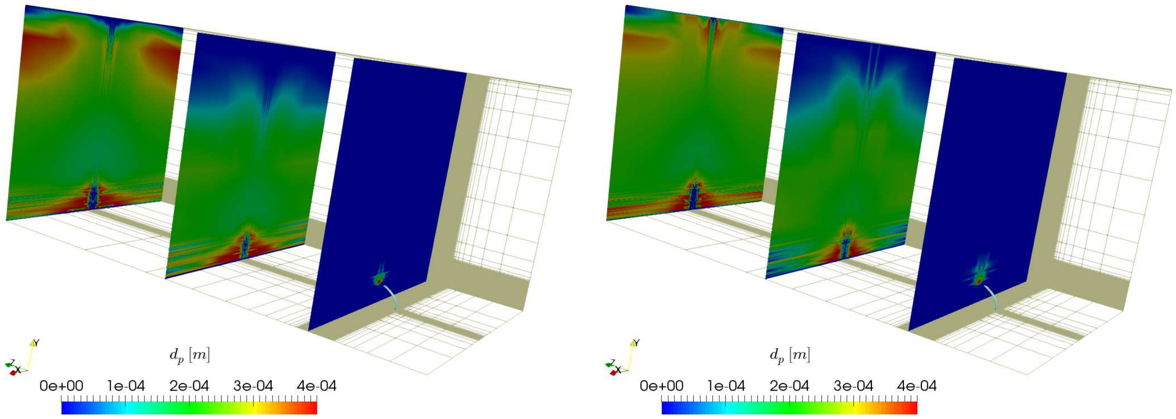

(a) $C_b = 3.44$ and TAB method.

(b) $C_b = 3.44$ and AB-TAB method.

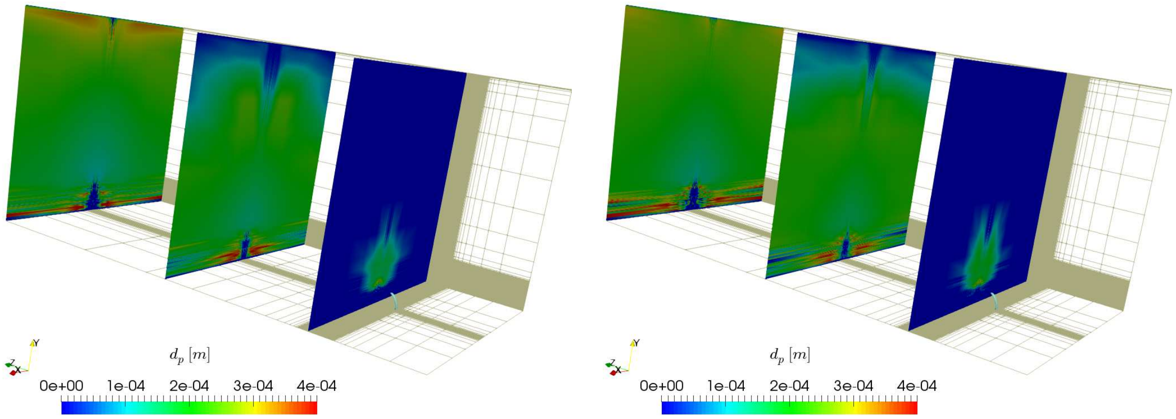

(c) $C_b = 2.6$ and TAB method.

(d) $C_b = 2.6$ and AB-TAB method.

Figura 4.22 – Average of droplet diameter in three planes for $C1$.

$z/d_j \approx 77$ and $z/d_j \approx 10$ from jet exit, are highlighted evidencing mean droplet diameter changes along air flow direction. Droplets spreads along the longitudinal axis (z) from the plane closer to the liquid column jet to the last plane, located at the air tunnel exit. This spreading enhances mean diameter distribution area on cross-sectional area of the air duct. For all simulations, droplets with the largest mean diameters ($\approx 400\,\mu m$) are located at whether top or bottom regions in the last plane ($z/d_j \approx 174$). The biggest drops are more inertial so that air flow takes more time (more space) to align these drops with its flow direction. By the other hand, droplets with the smallest mean diameters are located at middle region in all planes, since these droplets, less inertial, quickly align with the air crossflow direction.

Drops created from the column breakup are broken into smaller drops in a short distance from the jet exit. This fact can be verified by the comparisons of mean diameter distribution in the first plane, closer to the jet exit, for simulations using $C_b = 3.44$ and $C_b = 2.6$. For

$C_b = 3.44$ the jet top is very close to the first plane so that the most prominent droplets crossed this plane. However, for $C_b = 2.6$ the maximum value of mean diameter distribution is lower than that for $C_b = 3.44$, since the top jet for $C_b = 2.6$ is further from the first plane.

In terms of the secondary breakup models, the main qualitative difference between the two models is that the AB-TAB model shows a reduction on larger mean diameter on the top region of the planes compared to the results obtained by TAB model. In other words, droplets crossing the air streamlines are broken into smaller droplets more frequently when AB-TAB model was used. In fact, in AB-TAB model energy balance criterion for breakup is more accurately performed. Figure 4.23 shows a schematic diagram of a drop with oblique velocity in the air flow. Based on mean diameter distribution on specific planes the probability of a drop crossing the air streamline to be broken using AB-TAB model is higher than that using TAB model.

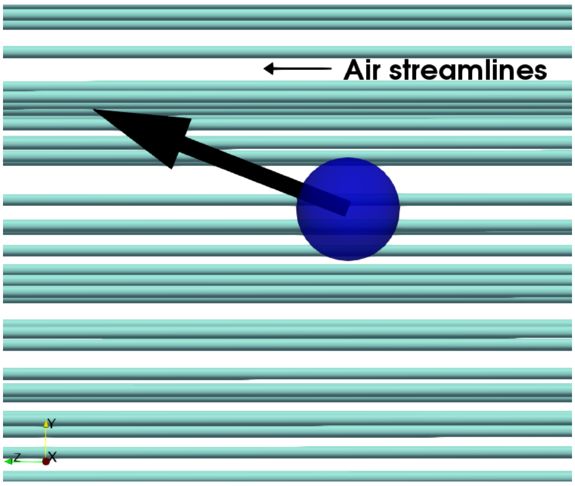

Figura 4.23 – Schematic diagram of a drop with oblique velocity compared to the air streamline.

For better understanding of the influences of primary breakup coefficients and secondary breakup models, numerical average values of the mean diameter and experimental mean diameter (DEEPE, 2006) on last plane for $C1$ are shown in Tab. 4.7 as well as relative deviation of numerical results related to the experimental results. This average value is taken for $y < 1.52\,cm$, following the experimental procedure of Deepe (2006) for the PDPA (Phase Doppler Particle Analysis).

Tabela 4.7 – Mean diameter of droplet in the last plane (air tunnel exit) for $C1$.

setup	$\bar{d}_p\,[\mu m]$	relative deviation [%]
$C_b = 3.44$ TAB model	183.4	72
$C_b = 3.44$ AB-TAB model	193.0	81
$C_b = 2.6$ TAB model	155.0	45
$C_b = 2.6$ AB-TAB model	172.0	61
experimental (DEEPE, 2006)	106.6	−−

In general, the experimental mean diameter is a tough parameter to predict. However, all simulations were able to estimate the order of magnitude of the mean diameter, regardless of the adopted primary breakup coefficients or secondary breakup models. Nevertheless, these deviations is not critical considering the complexity found in LJIC. The mean diameter of droplets on the air duct exit is quantitative parameter that depends on several factors, such as: primary breakup, secondary breakup, flow instabilities related to eddies structures, physical properties uncertainties, etc.

Considering only the primary breakup coefficient, the mean diameter is reduced when $C_b = 2.6$ is used instead of $C_b = 3.44$. In fact when $C_b = 2.6$ is used instead of $C_b = 3.44$, the liquid column jet is more perpendicular to the air flow, so that higher relative velocity is found between drop released from the jet top and air flow. Thus, critical Weber number is reached more quickly for $C_b = 2.6$ than for $C_b = 3.44$.

Regarding secondary breakup models, mean diameter is increased when AB-TAB model is used instead of standard TAB model. Despite differences found, mean diameter comparison is not enough to state which primary breakup coefficient and secondary breakup coefficient are more appropriate to solve spray formation in LJIC. However, mean diameter is very helpful to understand some tendencies in the choice of each primary breakup coefficient and secondary breakup model.

Figure 4.24 shows the general views of SMD for $C2$, using longitudinal planes located at the same positions those of $C1$, except the first plane that is located at $z/d_j \approx 11$. In the simulations, droplets rarely reaches top and bottom regions, except for the simulation using $C_b = 3.44$ and TAB model. In carrying out a visual analysis of the mean diameter distribution

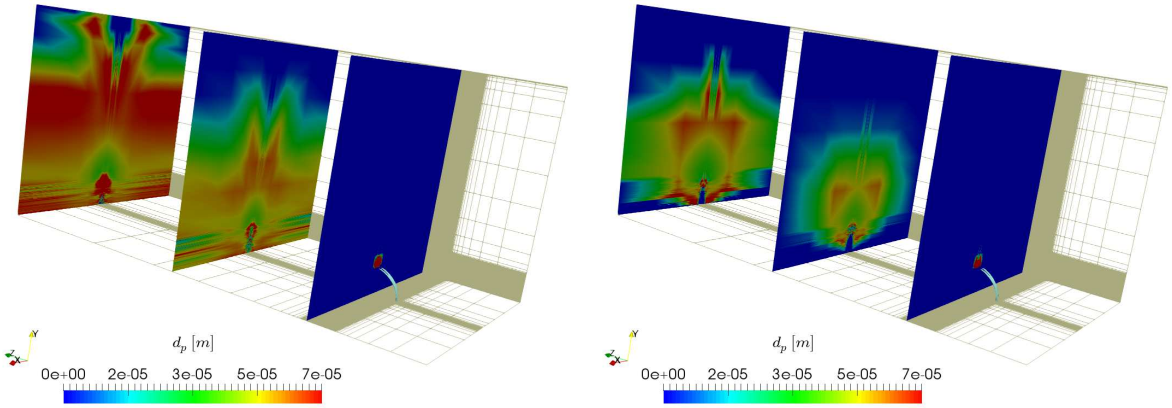

(a) $C_b = 3.44$ and TAB method. (b) $C_b = 3.44$ and AB-TAB method.

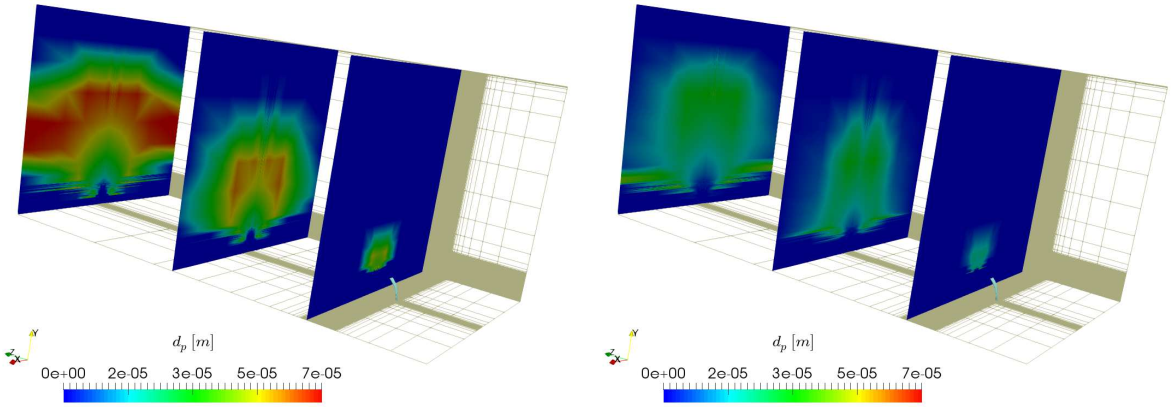

(c) $C_b = 2.6$ and TAB method. (d) $C_b = 2.6$ and AB-TAB method.

Figura 4.24 – Average of droplet diameter in three planes for $C2$.

on the last plane, a reduction of the maximum value of diameter when AB-TAB model is used instead TAB model can be observed. Also, droplet distribution in the domain is changed when different secondary breakup model is applied. The maximum value of diameter is also reduced when the primary breakup coefficient is decreased (from $C_b = 3.44$ to $C_b = 2.6$). As discussed above for $C1$, a smaller liquid column jet releases drops more perpendicularly to the air flow, so that the relative velocity is higher, enhancing the probability of secondary breakup.

Table 4.8 shows the mean diameter of droplet on the last plane for $C2$, similarly as made in $C1$. In $C2$, numerical results of mean diameter presents better agreement than that in $C1$. Since Weber number is higher in $C2$, the range of droplet diameter is lower than that in $C1$, so that a better prediction of the mean diameter becomes easier.

Considering the primary breakup coefficients, mean diameter is reduced significantly when $C_b = 2.6$ is used instead of $C_b = 3.44$, 22% of reduction for TAB model and

Tabela 4.8 – Mean diameter of droplet in the last plane (air tunnel exit) for $C2$.

setup	$\bar{d}_p\,[\mu m]$	relative deviation [%]
$C_b = 3.44$ TAB model	52.7	16
$C_b = 3.44$ AB-TAB model	39.6	37
$C_b = 2.6$ TAB model	41.0	34
$C_b = 2.6$ AB-TAB model	18.1	71
experimental (DEEPE, 2006)	62.5	$--$

54% of reduction for AB-TAB model. These reductions are related to the angle of the drop release at the top of the liquid column jet, as explained above in $C1$ case. The initial condition for the primary breakup is crucial to solve suitably spray formation in LJIC, which reinforces the importance of hybrid approach regarding pure Euler-Lagrange approach. Therefore, experimental comparisons are made in the following to establish which primary breakup coefficient is more appropriate to solve LJIC.

Unlike $C1$, in $C2$ mean diameter presents reduction when AB-TAB model is used instead of TAB model. Secondary breakup is not modeled linear, thus linear similar trends must not be expected for different two-phase flow conditions (for example different Weber numbers).

Different secondary breakup models result in remarkable changes on mass fraction distribution for $C2$, similarly in $C1$. These comparisons are made in next section.

4.2.4.2 Mass fraction distribution

Figure 4.25 shows the normalized mass fraction distribution for $C1$ using combinations of the two column breakup coefficients and the two secondary breakup models. The frequency of droplets crossing the sampling plane (Fig. 4.21) is predominantly influenced by the secondary breakup model, with little influence of the column height (C_b). However, it is worth remembering that for $C1$ primary breakup coefficient plays a significant role on mean diameter estimate with differences on mean diameter about of 10%. The AB-TAB model presents an overall good prediction of the droplet diameters, whereas the peak of the mass fraction distribution is shifted to the left when the original TAB model is used. Despite the AB-TAB appears to better predict the peak diameter in terms of mass distribution, the prediction

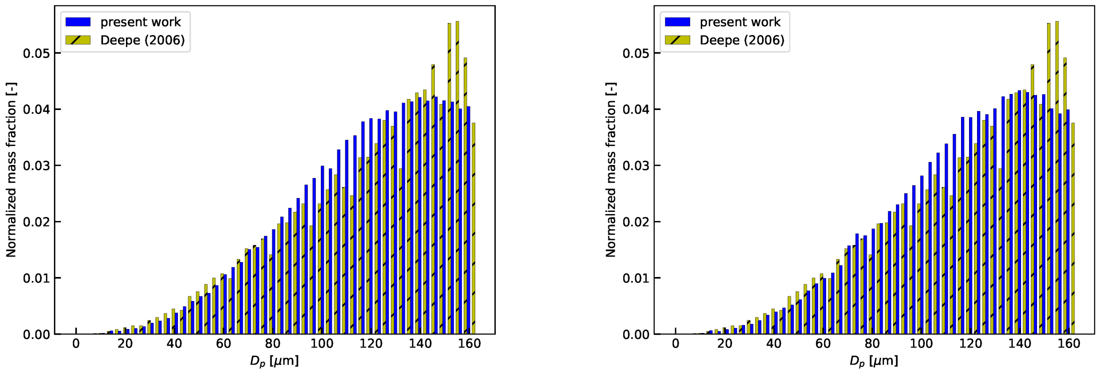

(a) $C_b = 2.6$ and TAB model.

(b) $C_b = 3.44$ and TAB model.

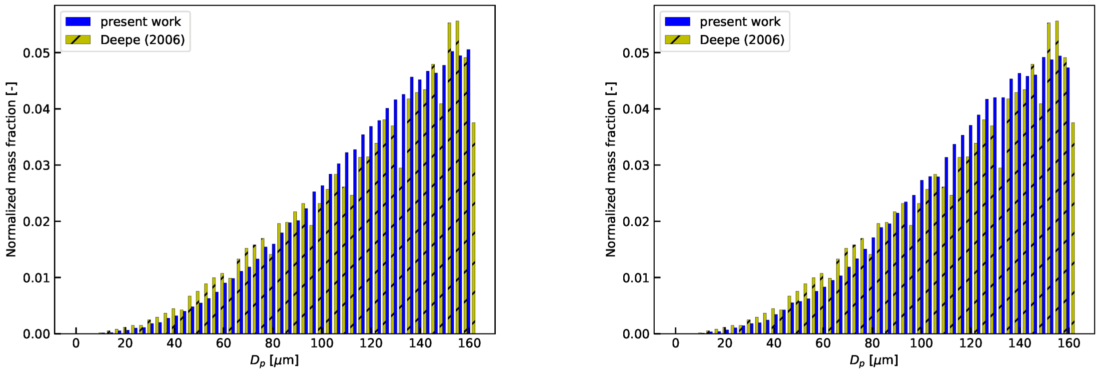

(c) $C_b = 2.6$ and AB-TAB model

(d) $C_b = 3.44$ and AB-TAB model.

Figura 4.25 – Mass fraction distribution for $C1$ using different primary and secondary breakup models.

for intermediate diameters ($40\,\mu m < D_p < 90\,\mu m$) is slightly better when the original TAB model is used.

The $l2 - norm$, represented by Equation 4.6, is a way to quantitatively assess the differences on mass fraction distribution for the different column breakup coefficients and secondary breakup models. The $l2 - norm$ expresses a cumulative difference between the numerical results and the experimental data for mass fraction distribution. Table 4.9 presents the deviations for simulations compared to the experimental data. Minor differences on $l2 - norm$ are seen for different primary and secondary breakup models. Therefore for low Weber numbers, such as in ($C1$), considering mass distribution and mean diameter in the air duct exit, mass fraction distribution is suitably predicted by either column breakup coefficient or secondary breakup model analyzed in this study. However, in terms of the peak of the the mass

Tabela 4.9 – $l2 - norm$ of the mass fraction distribution for $C1$.

Secondary breakup	C_b	$l2$
TAB model	2.6	3.78×10^{-2}
AB-TAB model	2.6	3.01×10^{-2}
TAB model	3.44	3.84×10^{-2}
AB-TAB model	3.44	3.57×10^{-2}

fraction distribution, the AB-TAB model was better to model secondary breakup on LJIC. This better prediction of the mass fraction distribution is related to the accurate conservation of linear momentum, angular momentum and kinetic energy during the breakup, provided by the AB-TAB model.

Figure 4.26 shows the numerical results for the normalized mass fraction distribution for $C2$. The distributions for all simulations are shifted to the left relative to the experiments. This may be due to the fact of the primary breakup coefficient for this condition should be higher than that correlated in the experiments. Because in the experiments different values of primary breakup coefficients were found, but a mean value was correlated for all experimented cases. For this reason, the simulation using the column breakup coefficient $C_b = 3.44$ and the AB-TAB model shows the best agreement among all simulations for $C2$. In fact, the simulations using $C_b = 3.44$ improve the prediction of the mass fraction distribution despite the secondary breakup model chosen, while the simulations using AB-TAB model presented a little improvement on the prediction of the peak of the mass fraction distribution, despite the primary breakup coefficient.

In Tab. 4.10 $l2-norm$ for $C2$ is shown, expressing the quantitative differences between the primary breakup coefficients and secondary breakup models in the prediction of the mass fraction distribution. Unlike $C1$, the choice of secondary breakup model and primary breakup coefficient affects mass fraction distribution more significantly. In the case with higher Weber

Tabela 4.10 – $l2 - norm$ of mass fraction distribution for $C2$.

Secondary breakup	C_b	$l2$
TAB model	2.6	13.97×10^{-2}
AB-TAB model	2.6	10.21×10^{-2}
TAB model	3.44	9.80×10^{-2}
AB-TAB model	3.44	6.56×10^{-2}

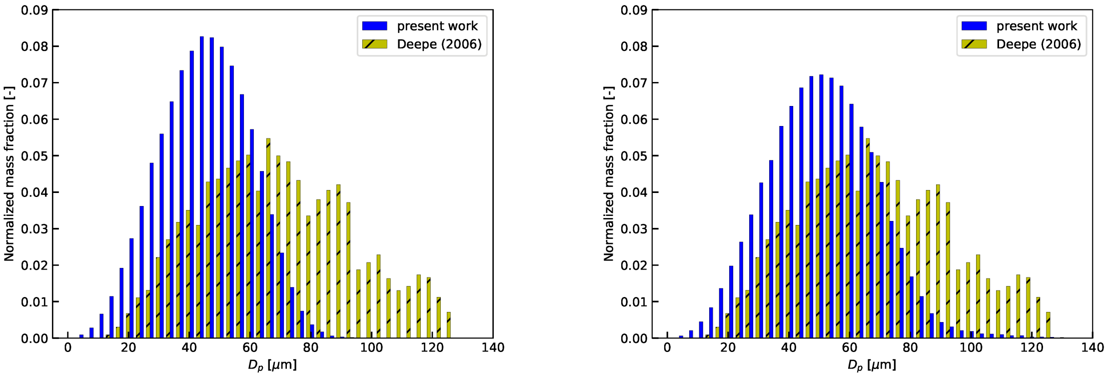

(a) $C_b = 2.6$ and TAB model.

(b) $C_b = 3.44$ and TAB model.

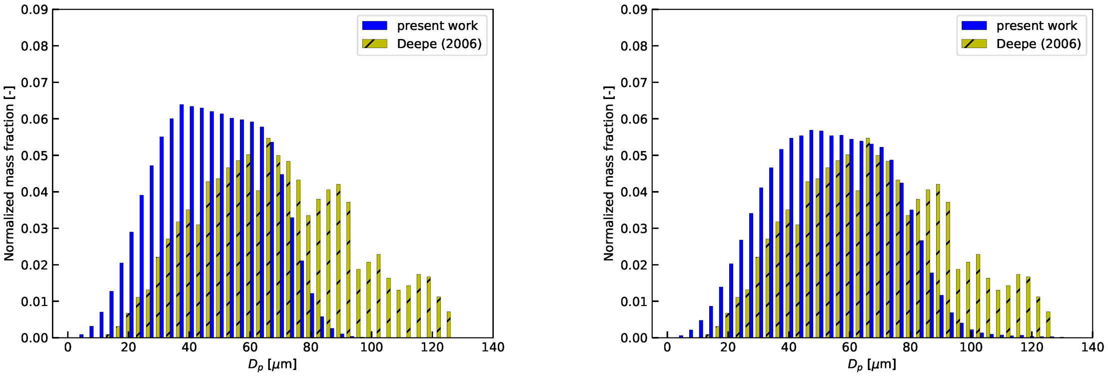

(c) $C_b = 2.6$ and AB-TAB model

(d) $C_b = 3.44$ and AB-TAB model.

Figura 4.26 – Mass fraction distribution for case $C2$ using different primary and secondary breakup models.

number ($C2$), the instabilities that promote secondary breakup of the droplets are more susceptible to appear, since the air velocity is higher and consequently the relative velocity that a droplet experiences is also higher. Therefore, extreme cases of spray formation in LJIC must account accurately the secondary breakup, as is made by the AB-TAB model. For a better prediction of spray features in LJIC Large Eddy Simulation (LES) strategy should be considered, in which the column jet position and aerodynamic instabilities on droplets can be solved with high accuracy, which would improve, respectively, the initial condition of the drop released at the jet top and the criterion for secondary breakup. Also, a primary breakup coefficient adjustment is an interesting way to obtain a better prediction of mass fraction distributions.

Column primary breakup coefficients for column breakup height of LJIC was obtained

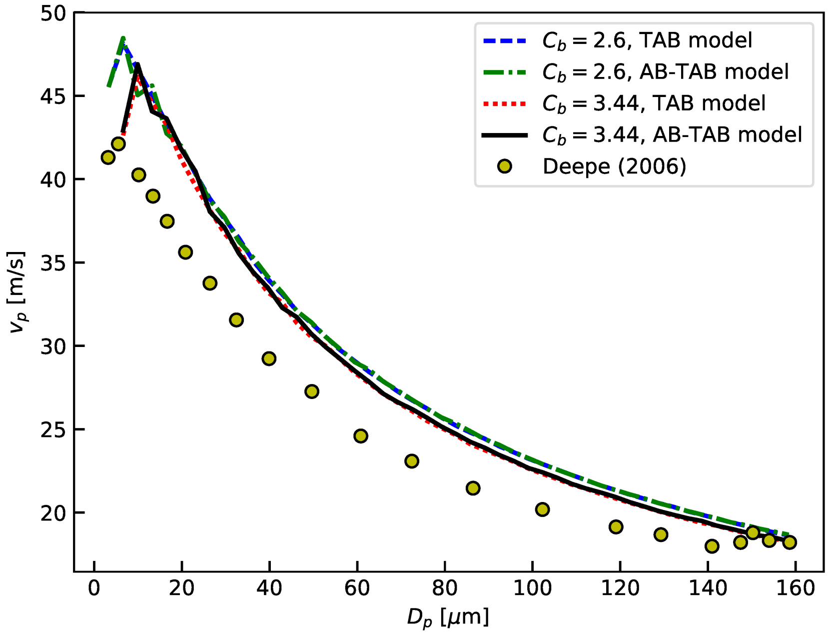

Figura 4.27 – Droplet velocity for $C1$ at the sampling plane $3.81\,cm$ downstream of the liquid jet nozzle.

through experimental images (WU; KIRKENDALL; FULLER, 1997; SALLAM; AALBURG; FAETH, 2003). Different liquids and conditions may present some differences on primary breakup coefficient value do exist. However, in the LJIC cases simulated in this work, the column breakup coefficient of Wu, Kirkendall and Fuller (1997), $C_b = 3.44$, presents better experimental agreement on mass fraction distribution.

4.2.4.3 *Droplet velocity*

Figure 4.27 shows droplet velocity for $C1$ using combinations of the two secondary breakup models and the two primary breakup coefficients. In general, the numerical results of droplet velocity overestimate the experimental data. However, the numerical droplet velocity fit well to the experimental data for larger droplets $(150\,\mu m < D_p < 160\,\mu m)$. Furthermore, the experimental trend of droplet velocity is well predicted numerically, with smaller droplets faster than larger droplets. Still considering the general results, due to the rare generation of smallest droplets $(D_p < 20\,\mu m)$ upstream of the sampling plane, the droplet velocity curve in this diameter range is not so smooth, creating some abrupt changes on curves. In fact, in $C1$ the secondary breakup is not so intense, as expected for this regime, $We = 11$, so that smaller droplets does not cross sampling plane so often.

The numerical results for droplet velocity using the different primary and secondary breakup models are quite similar to each other. Simulations using $C_b = 3.44$ showed a slight improvement on the droplet velocity curve, that is closer to the experimental curve than by using $C_b = 2.6$. The simulations using different secondary breakup models show nearly identical results on the droplet velocity curves. The higher influence of the primary breakup coefficient than the secondary breakup on the droplet velocity was expected, since droplet velocity is basically related to the drag force. The release condition of the drop at the top of the liquid jet is strongly dependent on the column breakup height.

All numerical results display a peak of droplet velocity for lower droplet diameters, similarly to the experimental data. However, the peak of the droplet velocity is better predicted when the column breakup coefficient $C_b = 2.6$ is used, regardless the secondary breakup model. Since the liquid column jet height using $C_b = 2.6$ is lower than that using $C_b = 3.44$, a Lagrangian drop released from the jet top using $C_b = 2.6$ experiences a higher shear tension than a Lagrangian drop created from the primary breakup using $C_b = 3.44$, generating lower droplet diameters. Figure 4.28 shows drops creation from jet top (solved through VOF method) for $C_b = 2.6$ and $C_b = 3.44$. In this figure the curvature of the column liquid jet is highlighted along air flow velocity vector. Clearly, the shear stress due to the air flow is more intense for $C_b = 2.6$ in the primary breakup region, since the liquid jet flow penetrates more perpendicularly into the air flow than the liquid jet flow using $C_b = 3.44$, which is more aligned to the airflow. This figure elucidates similar explanations for mean diameter and mass fraction distribution results.

Regarding secondary breakup models, in Fig. 4.27 negligible differences are seen on droplet velocity. In fact, in the vicinity of the measurement plane secondary breakup is extremely rare and droplet velocity is not affected by the kind of breakup that a droplet suffered.

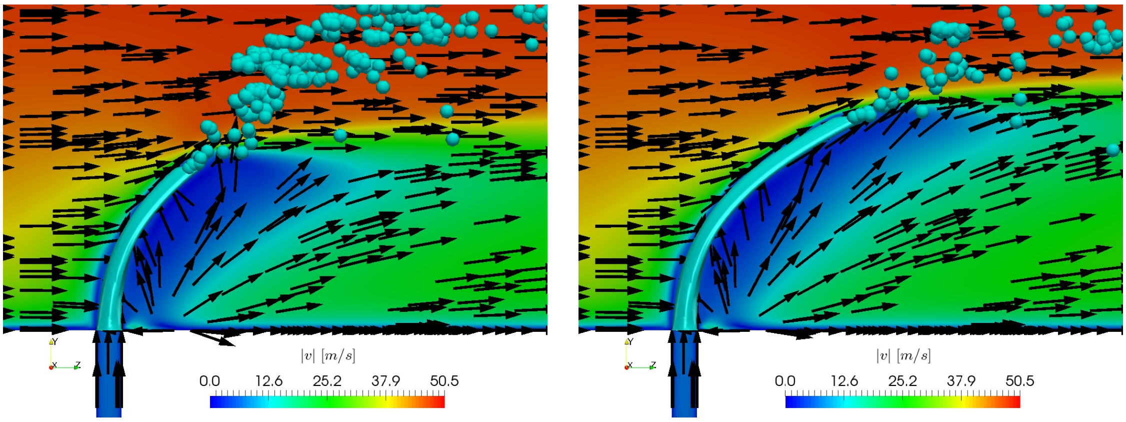

(a) $C_b = 2.6$.

(b) $C_b = 3.44$.

Figura 4.28 – Liquid jet curvature for $C1$.

Figure 4.29 shows the droplet velocity for $C2$ using combinations of the two secondary breakup models and the two primary breakup coefficients. For this higher Weber number case, $C2$, the numerical results of the droplet velocity depart more from the experimental data. The smaller droplets ($Dp \approx 10\,\mu m$) nearly reach the air velocity, while the larger droplets ($D_p > 80\,\mu m$) are having their velocity decreased. This discrepancy between the numerical results and experiments suggest that the interaction of the air flow and the liquid droplets is not being correctly accounted. Considering RANS strategy, it is worth investigating the effects of two-way coupling, which is carried out in the next section. Obviously, $C2$ is more complex than $C1$ and the interactions between air flow and liquid jet may change droplet velocity, consequently droplet breakup, more intensely than in $C1$. Drag correlation considering droplet distortion and unsteady coefficient (SHAO; LUO; FAN, 2017) were implemented and evaluated, but no significant improve was found in droplet velocity prediction.

Considering differences on droplet velocity for different primary and secondary breakup models in $C2$, the two different secondary breakup models present little changes on the numerical results, in the same way as in $C1$. Simulations using $C_b = 3.44$ result in lower droplet velocity than that using $C_b = 2.6$, which is also seen in the results for $C1$. Thus, independently of Weber number, droplet velocity is slightly influenced by column breakup height and is not influenced by the secondary breakup models evaluated.

Droplet velocity curves are not so smooth for large droplets ($D_p > 100\,\mu m$), because

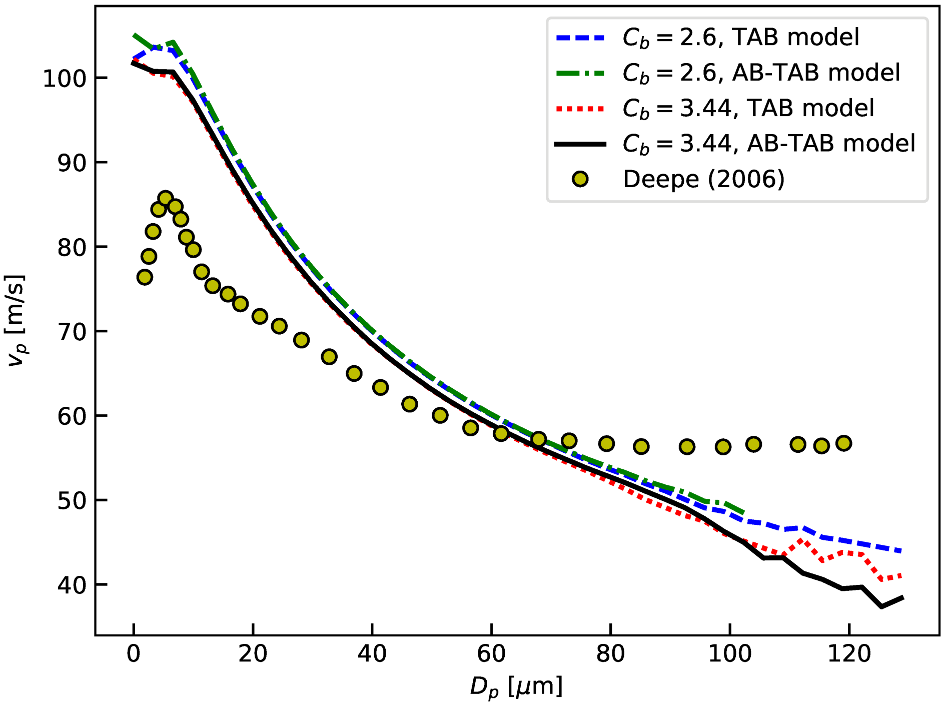

Figura 4.29 – Droplet velocity for $C2$ at the sampling plane $3.81\,cm$ downstream of the liquid jet exit.

the physical condition of $C2$ $(We = 53)$ promotes secondary breakup more frequently, such that the occurrence of larger droplets are rare, which is opposite to the $C1$ situation. For the simulation using $C_b = 2.6$ (lower height of the liquid column) and AB-TAB model, no droplets with $D_p > 102.3\,\mu m$ cross the sampling plane. For other simulations, droplets with $D_p > 100\,\mu m$ cross the sampling plane with low frequency, so that the droplet velocity curves in this diameter range display some spikes.

Therefore, considering the two primary breakup coefficients and two secondary breakup models analyzed, it can be stated that droplet velocity is not significantly influenced by secondary breakup models, whereas primary breakup coefficient has a small effect on the droplet velocity for all diameters.

4.2.5 Two-way coupling and droplet collision effects

In the previous sections, results were obtained disregarding droplet effects on the continuous flow and droplet-to-droplet collisions, i.e. one-way coupling was assumed. In this section, such modeling are accounted in order to assess their effect in the investigated cases. The two cases, $C1$ and $C2$, were solved considering droplet effects on the continuous flow and droplet-to-droplet collisions, using the column breakup coefficient $C_b = 3.44$ and the AB-TAB as secondary breakup model. In general, the column breakup coefficient, $C_b = 3.44$, and the secondary breakup model, AB-TAB, showed the best prediction of the mass fraction distribution and droplet velocity for both LJIC cases compared to the experimental data from Deepe (2006).

Figure 4.30 shows numerical results of mass fraction distribution for the two analyzed cases using two-way coupling and droplet-to-droplet collision, along with the previous results for one-way coupling. Mass fraction distribution considering two-way coupling and droplet collision agrees well with experimental data. However, minor differences can be seen when comparing with one-way coupling simulations.

The differences of numerical results and experimental results for the two cases are presented in Tab. 4.11 through $l2 - norm$ of mass fraction distribution for one-way coupling and two-way coupling with droplet-to-droplet. The differences on $l2 - norm$ considering one-way coupling and two-way coupling with droplet-to-droplet collision are very low. The negligible effect of two-way coupling and droplet-to-droplet collision is related to the low droplet concentration for the LJIC cases $C1$ and $C2$, the global liquid concentration in the domain are respectively 6.2×10^{-6} and 8.8×10^{-6}.

Tabela 4.11 – $l2 - norm$ of the mass fraction distribution for $C2$.

case	coupling	$l2$
$C1$	one-way	3.57×10^{-2}
$C1$	two-way and collision	3.41×10^{-2}
$C2$	one-way	6.56×10^{-2}
$C2$	two-way and collision	7.18×10^{-2}

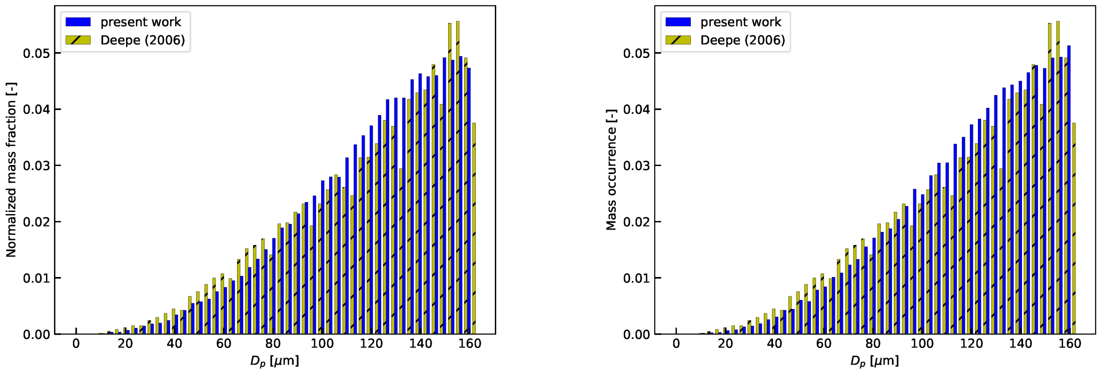

(a) $C1$: one-way coupling.

(b) $C1$: two-way coupling and droplets collision.

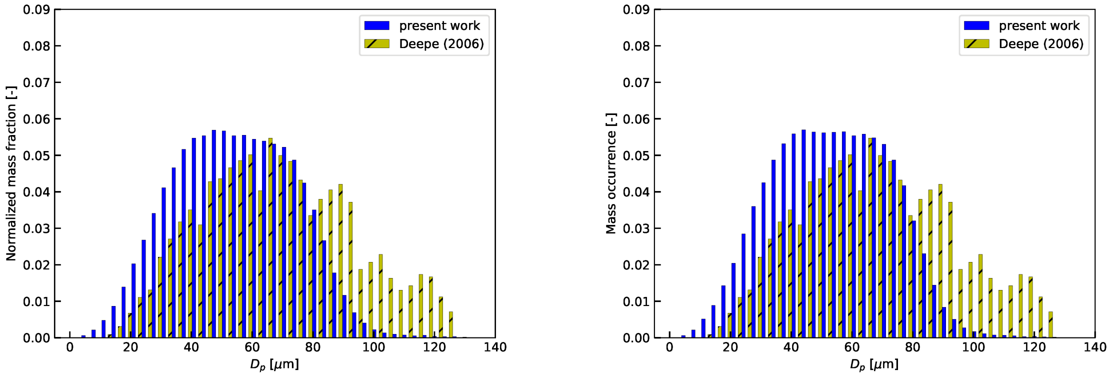

(c) $C2$: one-way coupling.

(d) $C2$: two-way coupling and droplets collision.

Figura 4.30 – Mass fraction distribution using $C_b = 3.44$ and AB-TAB model.

Figure 4.31 shows the results of the droplet velocity for the two cases with one-way coupling and with two-way coupling and droplet-to-droplet collisions, using primary breakup coefficient $C_b = 3.44$ and secondary breakup model AB-TAB. Clearly, one-way coupling and two-way coupling and droplet collision simulations present virtually same droplet velocity curve, except for low diameter in $C1$. However, the occurrence of small droplets in $C1$ is low and this result may be related to the an insufficient number of numerical iterations.

Two-way coupling and droplet collision results reveal minor changes on the droplet velocity. Actually, the droplet concentration in the LJIC domain is considered to be low enough so that the flow is dilute and the droplets in all simulations are small $(D_p < 160\mu m)$. For this reason, droplet collision rarely happens and the small droplets change very little the air flow.

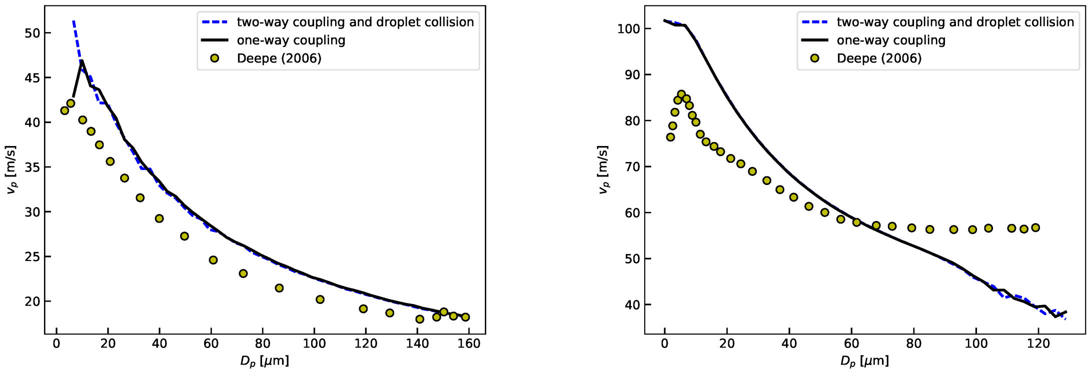

(a) $C1$.

(b) $C2$

Figura 4.31 – Droplet velocity using $C_b = 3.44$ and AB-TAB model.

Considering the results obtained in this work, two-way coupling and droplet collision modeling are unnecessary to solve spray formation in LJIC for low Weber number ($We < 60$). Differences between experimental and numerical results on droplet velocity, may be overcome using Large Eddy Simulations (LES), since LES is able to predict properly instantaneously how droplets interact with the turbulent flow.

Considering all comparisons and analyses carried out in this work, the hybrid model using $C_b = 3.44$ as the primary breakup coefficient and the AB-TAB secondary breakup model for spray formation in LJIC is the most suitable hybrid model for low computational cost and low Weber numbers ($We = 11$ and $We = 53$) regarding the state of art on spray formation in liquid jet in crossflow.

In next section the main conclusions of the work developed in dissertation are summarized as well as proposal future works related to the numerical analysis on spray formation in liquid jet in crossflow.

CHAPTER V

CONCLUSIONS AND FUTURE WORK

In this dissertation, a numerical framework was developed to analyze spray formation in a liquid jet in crossflow. This framework is composed by several methods to solve equations that represent physical features of two-phase flow. The main goal of this framework was to achieve good predictions of spray formation in LJIC using low computational costs preserving physical interaction between liquid column jet and air flow. The numerical strategy chosen to solve numerically spray formation was hybrid approach, which is a mixture of Euler-Euler approach and Euler-Lagrange approach. VOF method was implemented in a unstructured grid code based on finite volume discretization method, UNSCYFL3D, concerning Euler-Euler approach. Euler-Lagrange approach had been already implemented, but several changes were required to establish hybrid approach on UNSCYFL3D code.

VOF method was verified through advection/deforming and stationary tests for three dimensional two-phase flows, presenting errors according to those of the literature for the same advection schemes. Validation of the VOF method was performed for water droplet splash cases. Numerical results showed good agreement with experimental results, qualitatively and quantitatively.

Regarding the spray formation in liquid jet in crossflow, two cases with detailed experimental data were chosen to establish an advanced hybrid approach modeling suitable to solve liquid jet in crossflow at low computational costs. Since interfacial (inherent to two-phase flows) problems requires a high level of refinement and usually high number of elements, a half domain was defined considering symmetry along the air duct. This strategy for domain reduction showed negligible differences in mass fraction distribution and droplet velocity in the measurement plane. This domain reduction strategy was used for all simulations to evaluate two primary breakup coefficients, two secondary breakup models and the importance of two-way coupling with droplet-to-droplet collision.

General features of liquid jet in crossflow for the two cases were analyzed numerically. Spray formation was analyzed relating droplet formation and spreading along the air duct. These results were in accordance with physical and empirical understanding of spray formation in LJIC, such as: curvature of the liquid jet column; droplets breakup dynamic; interaction between airflow and liquid jet column; droplets velocity and size distributions in the numerical domain.

Mean diameter of droplet in the exit of air duct was influenced by primary breakup coefficients and secondary breakup models. For $C1$, simulations performed using AB-TAB secondary breakup model presented higher mean diameter of droplet than that using TAB model, as well as primary coefficient $C_b = 3.44$ presented higher mean diameter of droplet than that using $C_b = 2.6$. For $C2$, the mean diameter predicted by AB-TAB secondary breakup model was smaller than that using TAB model, while primary breakup coefficients presented same trend seen in $C1$: the mean diameter decreased with the reduction of the primary breakup coefficient.

Considering all numerical analysis made in this work for the two cases, the droplet velocity prediction is insensitive to the choice of secondary breakup model and primary breakup coefficient. However, simulations using AB-TAB model and $C_b = 3.44$ presented the best predictions of mass fraction distribution. Therefore, considering that droplet velocity and mass fraction distribution are one of the most difficult results to compare in spray formation in LJIC, AB-TAB model (DAHMS; OEFELEIN, 2016) with primary breakup $C_b = 3.44$ (WU; KIRKENDALL; FULLER, 1997), is a good choice for prediction of spray formation in LJIC for low Weber number at low computational costs.

The results and analyses presented in this work are substantial, since no publications related to hybrid approach evaluating primary breakup coefficients, secondary breakup models and two-way coupling and droplet-to-droplet collisions have been found so far. Therefore, this work is an important contribution on state of art for numerical prediction of sprays in liquid jet in crossflow.

Based on the experience gained in this dissertation, some future work that can contribute to the research development are summarized:

- Hybrid approach with same methodology applied to other physical conditions, for example higher Weber numbers, which would require higher number of elements;
- Evaluate the validity of shear breakup model, already implemented in the UNSCYFL3D code, in shear breakup regime cases;
- Aiming overcome time spent on serial numerical simulation, code parallelization is mandatory;
- Large eddy simulations to understand how droplets velocity and breakup are influenced by the eddy structures, which may be improve significantly droplet velocity prediction;
- Geometric discretization schemes (Piece-wise linear interface construction - PLIC) for the VOF method instead algebraic schemes (HRIC/CICSAM);
- Hybrid approach simulations able to solve numerically primary breakup on liquid column jet without any empirical correlations;
- and numerical simulations of spray formation from liquid film on wall.

REFERENCES

AALBURG, C.; FAETH, G. M.; SALLAM, K. A. Primary Breakup of Round Turbulent Liquid Jets in Uniform Crossflows. *AIAA Journal*, v. 734, n. January, p. 1907–1916, 2005. ISSN 0001-1452.

APTE, S. V.; GOROKHOVSKI, M.; MOIN, P. LES of atomizing spray with stochastic modeling of secondary breakup. *International Journal of Multiphase Flow*, v. 29, n. 9, p. 1503–1522, 2003. ISSN 03019322.

ARIENTI, M. et al. Aerodynamic Blockage Effect on the Spray Characteristics of a Liquid Jet Atomized by Crossflowing Air. *Proceedings of ASME Turbo Expo 2006 Power for Land, Sea and Air*, v. 1, n. May, p. 1–10, 2006.

ARIENTI, M.; SOTERIOU, M. C. Dynamics of Pulsed Jet in Crossflow. p. 1–12, 2007.

ARIENTI, M.; SUSSMAN, M. A High-Fidelity Study of High-Pressure Diesel Injection. 2015.

ARIENTI, M. et al. Modeling Wall Film Formation and Breakup Using an Integrated Interface-Tracking/Discrete-Phase Approach. *Journal of Engineering for Gas Turbines and Power*, v. 133, n. 3, p. 031501, 2011. ISSN 07424795.

BALASUBRAMANYAM, M. S.; CHEN, C. P. Modeling liquid jet breakup in high speed cross-flow with finite-conductivity evaporation. *International Journal of Heat and Mass Transfer*, v. 51, n. 15-16, p. 3896–3905, 2008. ISSN 00179310.

BECKER, J.; HASSA, C. *Breakup and Atomization of a Kerosene Jet in Crossflow at Elevated Pressure*. 2002. 49–68 p.

BEHZAD, M.; ASHGRIZ, N.; KARNEY, B. W. Surface breakup of a non-turbulent liquid jet injected into a high pressure gaseous crossflow. *International Journal of Multiphase Flow*, v. 80, p. 100–117, 2016. ISSN 03019322.

BEHZAD, M.; ASHGRIZ, N.; MASHAYEK, a. Azimuthal shear instability of a liquid jet injected into a gaseous cross-flow. *Journal of Fluid Mechanics*, v. 767, p. 146–172, 2015. ISSN 0022-1120. Disponível em: <http://www.journals.cambridge.org/abstract_S0022112015000361>.

BOUSSINESQ, J. . Essai sur la théorie des eaux courantes. *Mémoires présentés par divers savants à l'Académie des sciences de l'Institut national de France*, p. 744, 1877.

BRACKBILL, J. U.; KOTHE, D. B.; ZEMACH, C. A continuum method for modeling surface tension. *Journal of Computational Physics*, v. 100, n. 2, p. 335–354, 1992. ISSN 10902716.

BRAVO, L. et al. High Resolution Numerical Simulations of Primary Atomization in Diesel Sprays with Single Component Reference Fuels. n. May, p. 1–10, 2015.

BRAVO, L.; KWEON, C.-b. *A Review on Liquid Spray Models for Diesel Engine Computational Analysis*. [S.l.], 2014. Army Research Laboratory.

CHELKO, L. J. Penetration of Liquid Jets into a High-Velocity Air Stream. *Research Memorandum*, 1950.

CHEN, H. C.; PATEL, V. C. Near-wall turbulence models for complex flows including separation. *Computer Methods in Applied Mechanics and Engineering*, v. 26, n. 6, p. 641–648, 1988.

CHEN, X. et al. High-fidelity simulations of impinging jet atomization. *Atomization and Sprays*, v. 23, n. 12, p. 1079–1101, 2013. ISSN 10445110.

DAHMS, R. N.; OEFELEIN, J. C. The significance of drop non-sphericity in sprays. *International Journal of Multiphase Flow*, Elsevier Ltd, v. 86, p. 67–85, 2016. ISSN 03019322. Disponível em: <http://dx.doi.org/10.1016/j.ijmultiphaseflow.2016.07.010>.

De Souza, F. J.; De Vasconcelos Salvo, R.; De Moro Martins, D. A. Large Eddy Simulation of the gas-particle flow in cyclone separators. *Separation and Purification Technology*, v. 94, p. 61–70, 2012. ISSN 13835866.

De Souza, F. J.; SILVA, A. L.; UTZIG, J. Four-way coupled simulations of the gas-particle flow in a diffuser. *Powder Technology*, v. 253, p. 496–508, 2014. ISSN 00325910.

DEEPE, J. M. *Effect of Weber Number on the Fuel Transfer Function for Modulated Liquid Jets*. 2006. 119 p. Disponível em: <http://search.proquest.com/docview/28834514?accountid=2909>.

DENNER, F. Balanced-Force Two-Phase Flow Modelling on Unstructured and Adaptive Meshes. *thesis*, n. November, p. 237, 2013.

DESHPANDE, S. S.; ANUMOLU, L.; TRUJILLO, M. F. Evaluating the performance of the two-phase flow solver interFoam. *Computational Science & Discovery*, v. 5, n. 1, p. 014016, 2012. ISSN 1749-4699. Disponível em: <http://iopscience.iop.org/1749-4699/5/1/014016/article/>.

DUARTE, C. A. R. et al. The role of inter-particle collisions on elbow erosion. *International Journal of Multiphase Flow*, v. 89, p. 1 – 22, 2017. ISSN 0301-9322. Disponível em: <http://www.sciencedirect.com/science/article/pii/S0301932216302543>.

DUARTE, C. A. R.; SOUZA, F. J. de; SANTOS, V. F. dos. Numerical investigation of mass loading effects on elbow erosion. *Powder Technology*, v. 283, p. 593–606, 2015. ISSN 1873328X.

EDWARD, J.; JR, P.; PUCKETT, E. G. Second-order accurate volume-of-fluid algorithms for tracking material interfaces q. v. 199, p. 465–502, 2004.

ENAYATOLLAHI, R.; NATES, R. J.; ANDERSON, T. Characterising the heat and mass transfer coefficients for a crossflow interaction of air and water. *International Journal of Heat and Mass Transfer*, Elsevier Ltd, v. 111, p. 94–104, 2017. ISSN 00179310. Disponível em: <http://dx.doi.org/10.1016/j.ijheatmasstransfer.2017.03.098>.

FENG, Z.-G.; MICHAELIDES, E. E. Drag Coefficients of Viscous Spheres at Intermediate and High Reynolds Numbers. *Journal of Fluids Engineering*, v. 123, n. 4, p. 841, 2001. ISSN 00982202. Disponível em: <http://fluidsengineering.asmedigitalcollection.asme.org/article.aspx?articleid=1484329>.

FERZIGER, J. H.; PERIĆ, M. *Computational Methods for Fluid Dynamics*. Third edition. Germany: Springer Berlin Heidelberg, 2002.

FLUENT, A. Ansys Fluent Theory Guide. *ANSYS Inc., USA*, v. 15317, n. November, p. 724–746, 2013.

FONTES, D. H.; de Souza, F. J. NUMERICAL ANALYSIS OF JET IN CROSSFLOW SPRAY. *24th ABCM International Congress of Mechanical Engineering*, p. 3–8, 2017.

Fontes, D. H.; Duarte, C. A. D.; de Souza, F. J. Numerical simulation of a water droplet splash: effects of density interpolation schemes. *Mechanics Research Communications*, Elsevier Ltd, v. 90, p. 18–25, 2018. ISSN 00936413. Disponível em: <http://linkinghub.elsevier.com/retrieve/pii/S0093641318301368>.

FRANCOIS, M. M. et al. A balanced-force algorithm for continuous and sharp interfacial surface tension models within a volume tracking framework. *Journal of Computational Physics*, v. 213, n. 1, p. 141–173, 2006. ISSN 00219991.

HASELBACHER, a.; NAJJAR, F. M.; FERRY, J. P. An efficient and robust particle-localization algorithm for unstructured grids. *Journal of Computational Physics*, v. 225, n. 2, p. 2198–2213, 2007. ISSN 00219991.

HERNáNDEZ, J. et al. A new volume of fluid method in three dimensions-Part I: Multidimensional advection method with face-matched flux polyhedra. *International Journal for Numerical Methods in Fluids*, v. 58, n. 8, p. 897–921, nov. 2008. ISSN 02712091. Disponível em: <http://doi.wiley.com/10.1002/fld.1776>.

HERRMANN, M. A balanced force refined level set grid method for two-phase flows on unstructured flow solver grids. *Journal of Computational*

Physics, v. 227, n. 4, p. 2674–2706, 2008. ISSN 00219991. Disponível em: <http://www.sciencedirect.com/science/article/pii/S0021999107004998>.

HERRMANN, M. A parallel Eulerian interface tracking/Lagrangian point particle multi-scale coupling procedure. *Journal of Computational Physics*, Elsevier Inc., v. 229, n. 3, p. 745–759, 2010. ISSN 00219991. Disponível em: <http://linkinghub.elsevier.com/retrieve/pii/S0021999109005543>.

HIROYASU, H.; KADOTA, T. Fuel droplet size distribution in diesel combustion chamber. *SAE Paper*, p. 2615–2624, 1974.

HIRT, C.; NICHOLS, B. Volume of fluid (VOF) method for the dynamics of free boundaries. *Journal of Computational Physics*, v. 39, n. 1, p. 201–225, 1981. ISSN 00219991. Disponível em: <http://www.sciencedirect.com/science/article/pii/0021999181901455>.

HOJNACKI, J. T. Ramjet Engine Fuel Injection Studies. *Technical report to Aero Propulsion Lab., AFAPL-TR-72-76,*, v. 1, n. September, p. 754–852, 1972.

JAEGLE, F. et al. *Comparison of Euler-Euler and Euler-Lagrange methods for liquid jet in a cross flow*. 2010. 27 p.

JEMISON, M. et al. A Coupled Level Set-Moment of Fluid Method for Incompressible Two-Phase Flows. p. 454–491, 2013.

LAUNDER, B. E.; SPALDING, D. B. THE NUMERICAL COMPUTATION OF TURBULENT FLOWS. *Computer Methods in Applied Mechanics and Engineering*, v. 3, p. 269–289, 1974.

LEONARD, B. P. The ULTIMATE conservative difference scheme applied to unsteady one-dimensional advection. *Computer Methods in Applied Mechanics and Engineering*, v. 88, p. 17–74, 1991.

LI, P. et al. Numerical simulation of the gas-liquid interaction of a liquid jet in supersonic crossflow. *Acta Astronautica*, Elsevier Ltd, v. 134, n. November 2016, p. 333–344, 2017. ISSN 00945765. Disponível em: <http://dx.doi.org/10.1016/j.actaastro.2016.12.025>.

LI, X.; ARIENTI, M.; SOTERIOU, M. C. Towards an Efficient , High-Fidelity Methodology for Liquid Jet Atomization Computations. *Aiaa*, p. 092407, 2010.

LI, X.; SOTERIOU, M. C. High fidelity simulation and analysis of liquid jet atomization in a gaseous crossflow at intermediate Weber numbers. *Physics of Fluids*, v. 28, n. 8, p. 082101, 2016. ISSN 1070-6631. Disponível em: <http://scitation.aip.org/content/aip/journal/pof2/28/8/10.1063/1.4959290>.

MARIC, T.; MARSCHALL, H.; BOTHE, D. voFoam-A geometrical Volume of Fluid algorithm on arbitrary unstructured meshes with local dynamic adaptive mesh refinement using OpenFOAM. *arXiv preprint arXiv:1305.3417*, p. 1–30, 2013. Disponível em: <http://arxiv.org/abs/1305.3417>.

MATHUR, S. R.; MURTHY, J. Y. A pressure-based method for unstructured meshes. *Numerical Heat Transfer, Part B: Fundamentals: An International Journal of Computation and Methodology*, v. 31, n. 2, p. 195–215, 1997. ISSN 1040-7782. Disponível em: <http://www.tandfonline.com/doi/abs/10.1080/10407782.2014.916109>.

MAZALLON, J. et al. Aerodynamic Primary Breakup At the Surface of Nonturbulent Round Liquid Jets in Crossflow. *AIAA Journal*, p. 15, 1998.

MORTON, D.; RUDMAN, M.; LIOW, J.-L. An investigation of the flow regimes resulting from splashing drops. *Physics of Fluids*, v. 12, n. 4, p. 747, 2000. ISSN 10706631. Disponível em: <http://link.aip.org/link/PHFLE6/v12/i4/p747/s1&Agg=doi>.

MUZAFERIJA, S. et al. A two-fluid Navier-Stokes solver to simulate water entry. *Proceedings of the 22nd symposium on Naval Hydrodynamics*, 22nd Symposium on Naval Hydrodynamics, Washington, D.C., p. 638–651, 1998. Disponível em: <https://www.nap.edu/read/9771/chapter/13>.

NG, C. L.; SANKARAKRISHNAN, R.; SALLAM, K. a. Bag breakup of nonturbulent liquid jets in crossflow. *International Journal of Multiphase Flow*, v. 34, n. 3, p. 241–259, 2008. ISSN 03019322.

ODA, T. et al. Characterization of Liquid Jet Atomization across a High-Speed Airstream. *JSME International Journal Series B*, v. 37, p. 937–944, 1994. ISSN 1340-8054.

OGUZ, H. N.; PROSPERETTI, A. Bubble Entrainment by the Impact of Drops on Liquid Surfaces liquid surfaces. *Journal of Fluid Mechanics*, v. 219, p. 143–179, 1990.

O'ROURKE, P. J.; AMSDEN, A. A. The TAB Method for Numerical Calculation of Spray Droplet Breakup. *International Fules and Lubricants Meeting and Exposition, Toronto, Ontario*, 1987.

PATANKAR, S. *Numerical heat transfer and fluid flow*. 1980. 1–197 p.

POPINET, S. An accurate adaptive solver for surface-tension-driven interfacial flows. *Journal of Computational Physics*, Elsevier Inc., v. 228, n. 16, p. 5838–5866, 2009. ISSN 0021-9991. Disponível em: <http://dx.doi.org/10.1016/j.jcp.2009.04.042>.

PRAKASH, R. S. et al. Breakup of Volatile Liquid Jet in Hot Cross Flow. *Procedia IUTAM*, v. 15, p. 18–25, 2015. ISSN 22109838.

PUMPHREY, H. C.; CRUM, L. A. Acoustic emissions associated with drop impacts. In: _____. *Sea Surface Sound: Natural Mechanisms of Surface Generated Noise in the Ocean*. Dordrecht: Springer Netherlands, 1988. p. 463–483. ISBN 978-94-009-3017-9.

RAGUCCI, R.; BELLOFIORE, A.; CAVALIERE, A. Breakup and breakdown of bent kerosene jets in gas turbine conditions. *Proceedings of the Combustion Institute*, v. 31 II, p. 2231–2238, 2007. ISSN 15407489.

REBELLO, P. *Liquid Jet Injection into a Supersonic Airstream*. [S.l.: s.n.], 1972. 125 p.

REITZ, R. 4. Spray Processes. *Spray Course*, p. 1–44, 2006. Disponível em: <papers2://publication/uuid/BEE087C4-3B90-4D5F-963E-8C28C55B1ECB>.

REITZ, R. D. Modeling Atomization Processes in High-Pressure Vaporizing Sprays. *Atomization and Sprays*, v. 3, p. 309–337, 1987. ISSN 0266-3481.

REYNOLDS, O. On the dynamical theory of incompressible viscous fluids and the determination of the criterion. *Philosophical Transactions of the Royal Society of London A: Mathematical, Physical and Engineering Sciences*, The Royal Society, v. 186, p. 123–164, 1895. ISSN 0264-3820. Disponível em: <http://rsta.royalsocietypublishing.org/content/186/123>.

RHIE, C. M.; CHOW, W. L. Numerical study of the turbulent flow past an airfoil with trailing edge separation. *3rd Joint Thermophysics, Fluids, Plasma and Heat Transfer Conference*, v. 21, n. 11, p. 1525—-1532, 1983. ISSN 0001-1452.

SALLAM, K. A.; AALBURG, C.; FAETH, G. M. BREAKUP OF ROUND NONTURBULENT LIQUID JETS IN GASEOUS CROSSFLOWS. n. January, p. 1–16, 2003.

SALLAM, K. a. et al. Breakup of Turbulent and Non-Turbulent Liquid jets in Gaseous Crossflows. *44th AIAA Aerospace Sciences Meeting and Exhibit; Reno, NV; USA; 9-12 Jan. 2006*, n. January, p. 1–13, 2006.

SALVO, R. V. *Aplicação da metodologia euleriana-lagrangiana à análise do processo de separação em ciclones*. [S.l.: s.n.], 2013. 245 p.

SCHILLER, L.; NAUMANN, A. A drag coefficient correlation. *Zeitschrift des Vereins Deutscher Ingenieure*, v. 77, p. 318–320, 1935.

SHAO, C.; LUO, K.; FAN, J. Detailed numerical simulation of unsteady drag coefficient of deformable droplet. *Chemical Engineering Journal*, v. 308, p. 619–631, 2017. ISSN 13858947.

SHINJO, J.; UMEMURA, A. Detailed simulation of primary atomization mechanisms in Diesel jet sprays (isolated identification of liquid jet tip effects). *Proceedings of the Combustion Institute*, Elsevier Inc., v. 33, n. 2, p. 2089–2097, 2011. ISSN 1540-7489. Disponível em: <http://dx.doi.org/10.1016/j.proci.2010.07.006>.

SINHA, A. et al. Airblast spray in crossflow - structure, trajectory and droplet sizing. *International Journal of Multiphase Flow*, v. 72, p. 97–111, 2015. ISSN 03019322.

SOMMERFELD, M. Validation of a stochastic Lagrangian modelling approach for inter-particle collisions in homogeneous isotropic turbulence. *International Journal of Multiphase Flow*, v. 27, n. 10, p. 1829–1858, 2001.

SPRITTLES, J. E. Kinetic Effects in Dynamic Wetting. *Physical Review Letters*, p. 6, 2017.

TANNER, F. X. Liquid jet atomization and droplet breakup modeling of non-evaporating diesel fuel sprays. In: *SAE Technical Paper*. SAE International, 1997. Disponível em: <https://doi.org/10.4271/970050>.

UBBINK, O. Numerical prediction of two fluid systems with sharp interfaces. *Splash*, n. January 1997, p. 69, 1997. ISSN 00219991. Disponível em: <http://powerlab.fsb.hr/ped/kturbo/OpenFOAM/docs/OnnoUbbinkPhD.pdf>.

UBBINK, O.; ISSA, R. I. A Method for Capturing Sharp Fluid Interfaces on Arbitrary Meshes. *Journal of Computational Physics*, v. 153, p. 26–50, 1999.

WHITE, F. *Fluid Mechanics*. McGraw-Hill, 2003. (McGraw-Hill international editions). ISBN 9780072402179. Disponível em: <https://books.google.com.br/books?id=1DYtptq3OC4C>.

WU, P.-k.; KIRKENDALL, K. A.; FULLER, R. P. Breakup Processes of Liquid Jets in Subsonic Crossflows. *Journal of Propulsion and Power*, v. 13, n. 1, 1997.

XIAO, D. et al. An efficient and accurate algebraic interface capturing method for unstructured grids in 2 and 3 dimensions: The THINC method with quadratic surface representation. *International Journal for Numerical Methods in Fluids*, v. 79, n. 11, p. 580–595, dez. 2015. ISSN 02712091. Disponível em: <http://doi.wiley.com/10.1002/fld.4066>.

YOUNGS, D. L. Time-Dependent Multi-Material Flow with Large Fluid Distortion. *Numerical Methods for Fluid Dynamics*, p. 273–285, 1982.